DIELECTRIC METASURFACES AS PASSIVE RADIATIVE COOLERS, COLORIMETRIC REFRACTIVE INDEX SENSORS, COLOR FILTERS, AND ONE-WAY PERFECT ABSORBER/REFLECTORS WITH TRANSPARENT SIDEBANDS

A THESIS SUBMITTED TO

THE GRADUATE SCHOOL OF ENGINEERING AND SCIENCE

OF BILKENT UNIVERSITY

IN PARTIAL FULFILLMENT OF THE REQUIREMENTS FOR

THE DEGREE OF

MASTER OF SCIENCE

IN

ELECTRICAL AND ELECTRONICS ENGINEERING

By

Deniz Umut YILDIRIM

July 2020

DIELECTRIC METASURFACES AS PASSIVE RADIATIVE COOLERS, COLORIMETRIC REFRACTIVE INDEX SENSORS, COLOR FILTERS, AND ONE-WAY PERFECT ABSORBER/REFLECTORS WITH TRANSPARENT SIDEBANDS

By Deniz Umut YILDIRIM

July 2020

We certify that we have read this thesis and that in our opinion it is fully adequate, in scope and in quality, as a thesis for the degree of Master of Science.

Ekmel Özbay(Advisor)

Vakur Behçet Ertürk

Hamza Kurt

Approved for the Graduate School of Engineering and Science:

Ezhan Karaşan
Director of the Graduate School

ABSTRACT

DIELECTRIC METASURFACES AS PASSIVE RADIATIVE COOLERS, COLORIMETRIC REFRACTIVE INDEX SENSORS, COLOR FILTERS, AND ONE-WAY PERFECT ABSORBER/REFLECTORS WITH TRANSPARENT SIDEBANDS

Deniz Umut YILDIRIM
M.S. in Electrical and Electronics Engineering
Advisor: Ekmel Özbay
July 2020

Metamaterials define the class of synthetic, man-made materials with exotic properties that cannot be observed with natural materials. Their sub-wavelength counterparts are called metasurfaces. In particular, dielectric metasurfaces are extensively studied due to the advantages they offer in comparison to metamaterials, which are mainly their reduced thickness and not suffering from ohmic losses that are present in metals. Here, we design and implement dielectric metasurfaces in four important application areas, namely 1. Passive radiative coolers for spacecraft, 2. Colorimetric refractive index sensors, and 3. Color filters based on monolayer graphene. 4. A metasurface with a resonant one-way absorption/reflection with transmissive sidebands functionality

In the first work, we propose a facile, lithography-free fabrication route, exploiting oblique deposition to design an optical solar reflector, which constitutes the physical interface between the spacecraft and space. Our proposed metasurface is based on disordered and densely packed Indium Tin Oxide (ITO) nanorod forests. The excellent light trapping capability of the nanorod forests, randomness in the geometrical dimensions of these nanorods, combined with the lossy plasmonic nature of ITO in the thermal-infrared range led to strong coupling of thermal-radiation to broad plasmonic resonances, and consequently an experimental emissivity of 0.968, in a very wide range from 2.5 μm to 25 μm. In the solar spectrum, low-loss dielectric characteristic of ITO resulted in an experimental solar absorptivity as small as 0.168. This design with high-throughput, robustness, low-cost and high-performance, therefore, shows great promise not only for space

missions but also for promoting environmentally friendly passive radiative cooling for our planet and thermal imaging in the field of security labeling.

In the second work, we propose a highly-sensitive refractive index sensor, utilizing the excitation of guided-modes of a novel, 2-dimensional periodically modulated dielectric grating-waveguide structure. The optimized nanosensor can numerically excite guided-mode resonances with an ultra-narrow linewidth (full-width at half-maximum) of 0.58 nm. Sensitivity is numerically investigated by considering the deposition of dielectric layers on the structure. For a layer thickness of 30 nm, the maximum sensitivity reached as high as 110 nm/refractive index unit (RIU), resulting in a very high Figure of Merit of 190. The fabricated devices with 30 nm Aluminum Oxide and Zinc Oxide coatings achieved a maximum sensitivity of 235.2 nm/RIU with a linewidth of 19 nm. Colorimetric detection with polarization-insensitivity is confirmed practically by a simple optical microscope. Samples with different coatings have been observed to have clearly distinct colors, while the color of each sample is nearly identical upon azimuthal rotation. Excellent agreement is obtained between the numerical and experimental results regarding the spectral position of the resonances and sensitivity. The proposed device is, therefore, highly promising in efficient, highly-sensitive, almost lossless, and compact molecular diagnostics platform in the fields of biomedicine with personalized, label-free, early point-of-care diagnosis and field analysis, drug detection, and environmental monitoring.

In the third work, we numerically propose a graphene perfect absorber that can be utilized as a color filter, utilizing the excitation of guided-modes of a dielectric slab waveguide by a novel sub-wavelength dielectric grating structure. When the guided-mode resonance is critically coupled to the graphene, we obtain perfect absorption with an ultra-narrow bandwidth (full-width at half-maximum) of 0.8 nm. The proposed design not only preserves the spectral position of the resonance, but also maintains $> 98\%$ absorption at all polarization angles. The spectral position of the resonance can be tuned as much as 400 nm in visible and near-infrared regimes by tailoring geometrical parameters. The proposed device has great potential in efficient, tunable, ultra-sensitive, compact and easy-to-fabricate advanced photodetectors and color selective notch filters.

In the fourth and final work, we numerically propose the one-way perfect absorption of near-infrared (NIR) radiation in a tunable spectral range with high

transmission in the neighboring spectral ranges. This functionality is obtained by using a 2-dimensional, guided-mode resonance based grating-waveguide metasurface that acts as a frequency-selective reflector, a spacer dielectric, and an absorbing oxide layer. Within the bandwidth of the excited guided-mode resonance excited at 1.82μm with a full-width at half-maximum of 19 nm), we confirmed perfect absorption when light is incident from one of the two opposite directions, whereas in the other direction, perfect reflection is observed. The forward-to-backward absorption ratio reached as high as 60, while the thickness of the entire structure is in the order of the operating wavelength. In addition to the spectral tunability of the excited resonances and their bandwidths, our proposed device supports transparency windows with 65% transmission in the adjacent frequency bands. Our 2D grating is also verified to enable near-absolute insensitivity to the polarization state of incident light. Geometrical parameter modification also gives our design great tunability, as we also designed a device with 300 nm absorption/reflection linewidth.

Keywords: metasurface, passive radiative coolers, colorimetric sensors, color filters, asymmetric absorber/reflectors, perfect absorber.

ÖZET

UZAY ARACI PASİF RADİATİF SOĞUTUCU, KOLORİMETRİK KIRICILIK İNDİSİ SENSÖRÜ, RENK FİLTRESİ, VE KOMŞU BANTLARDA GEÇİRGEN TEK TARAFLI MÜKEMMEL SOĞURUCU/YANSITICILAR OLARAK DİELEKTRİK METAYÜZEYLER

Deniz Umut YILDIRIM
Elektrik ve Elektronik Mühendisliği, Yüksek Lisans
Tez Danışmanı: Ekmel Özbay
Temmuz 2020

Metamateryaller, doğal malzemelerle gözlenemeyecek egzotik özellikleri görmemizi sağlayan, insan yapımı, yapay malzemeleri tanımlamaktadır. Metamateryallerin dalga boyundan daha küçük kalınlığa sahip olan karşılıklarına ise metayüzey denmektedir. Özellikle dielektrik metayüzeyler metamateryallere karşı sundukları azaltılmış kalınlıkları ve ohmik kayıplara sahip olmamaları avantajlarından dolayı oldukça yoğun bir şekilde çalışılmaktadır. Burada, dört önemli uygulamaya yönelik metayüzeyler tasarlıyoruz ve uyguluyoruz: 1. Uzay mekikleri için pasif radiatif soğutucular, 2. kolorimetrik kırıcılık indisi sensörleri, ve 3. tek katman grafin tabanlı renk filtreleri. 4. Rezonant tek yönlü soğurma/yansıtma ve geçirgen yanbantlar işlevselliğine sahip bir metayüzey.

Ilk projede, eğik açılı kaplama metodu kullanarak hızlı ve litografi içermeyen bir fabrikasyon rotasını, uzay mekikleri ve etrafı arasındaki fiziksel arayüz olarak kullanılabilecek bir optik solar yansıtıcı üretmek için önerdik. Önerdiğimiz metayüzey düzensiz ve sıkı bir şekilde paketlenmiş İndiyum Kalay Oksit (ITO) nanoçubuk ormanlarını baz almaktadır. Bu nanoçubuk ormanlarının mükemmel ışık hapsetme kapasitesi, geometrik boyutlardaki rastgelelik ve ITO'nun termal-kızılötesi bölgesindeki kayıplı plazmonik optik karakteristiği sayesinde termal-radyasyonun geniş plazmonik rezonanslara bağlanması ve sonuç olarak deneysel olarak, 2.5 μm-25 μm aralığında 0.968 termal yayma elde edilmesi sağlanmıştır. Solar spektrumda ise, ITO'nun düşük kayıplı dieletrik karakteristiği deneysel solar emiciliğin 0.168'e limitlenmesini sağlamıştır. Sonuç olarak, yüksek çıktı, sağlamlık, düşük maliyet ve yüksek performans sunan bu dizaynımız, sadece

uzay görevlerinde değil, aynı zamanda gezegenimiz için çevre dostu pasif radiatif soğutucuların desteklenmesi ve güvenlik etiketlemesi alanında termal görüntüleme uygulaması için de oldukça umut vadedicidir.

Ikinci projemizde, 2 boyutlu, periyodik olarak modüle edilmiş bir dielektrik ızgara-dalga kılavuzu yapısının desteklenen modlarının uyarılması esasına dayanan ve kırıcılık indisine oldukça duyarlı bir sensör öneriyoruz. Optimize edilmiş nanosensörlerin nümerik olarak 0.58 nanometrelik ultra-dar spektral genişliğine sahip (yarı-maksimum noktasındaki tam-genişlik) rezonansları uyarabileceği gösterilmiştir. Hassaslık ise dieletrik katmanların yapı üzerine kaplanması düşünülerek numerik olarak incelenmiştir. Katman kalınlığı 30 nm iken maksimum hassaslık 110 nm/Kırıcılık indisi birimi (RIU)ne kadar çıkmıştır, bu da çok yüksek bir başarım ölçüsü olan 190 değerinin alınmasını sağlamıştır. Fabrike edilen ve üzerlerine Alüminyum Oksit ve Çinko Oksit kaplı örnekler maksimum duyarlılık değeri olarak 235.2 nm/Kırıcılık indisi birimi (RIU)ne ve 19 nm spektral genişliğine kadar erişmiştir. Kolorimetrik tespit etme ve polarizasyona duyarsızlık özellikleri ise basit bir optik mikroskop yardımıyla doğrulanmıştır. Farklı dieletrik katmanlarla kaplanmış örneklerin bariz farklı renklerinin olduğu ve azimutal yönde döndürüldüklerinde renklerinin değişmediği gözlendi. Ayrıca, rezonansların spektral pozistonları ve duyarlılık konusunda deneysel veriler ve nümerik sonuçlar arasında mükemmel bir uyum gözlendi. Sonuç olarak, önerdiğimiz cihaz, biyotıp alanında bakım noktasında kişiselleştirilmiş ve etiketsiz bir şekilde erken tanı koyma, alan analizi ve çevresel monitörleme konuları için verimli, yüksek duyarlılıklı, neredeyse optik kayıpsız ve kompakt bir moleküler tanılama platformu sunmaktadır.

Üçüncü projemizde ise, nümerik sonuçlara dayanarak dielektrik bir levha dalga-kılavuzunun desteklenen modlarının özgün bir dielektrik ızgara yapısı sayesinde uyarılması prensibiyle çalışan ve renk filtresi olarak kullanılabilecek bir grafin mükemmel soğurucu öneriyoruz. Bu desteklenen modların grafine kritik bir şekilde grafin ile bağlandığında, 0.8 nm'lik bir spektral genişliğe (yarım-maksimum noktasındaki tam-genişlik) sahip bir mükemmel soğurma elde ettik. Önerdiğimiz dizayn tüm polarizasyon açılarında hem rezonansın spektral pozisyonunu, hem de %98'in üzerinde soğurma şiddetini korumaktadır. Uyarılan rezonansın spektral pozisyonu geometrik parametrelerin değiştirilmesi sonucu görünür ve yakın-kızılötesi (NIR) bölgelerinde 400 nm'ye kadar ayarlanabilmiştir.

Önerdiğimiz cihaz bu sonuçlar ışığında verimli, ayarlanabilir, ultra-hassas, kompakt, fabrikasyonu kolay, gelişmiş fotodetektörlerin ve ışık seçici bant durdurma filtreleri için büyük potansiyel göstermektedir.

Dördüncü ve son projemizde, nümerik olarak yakın-kızılötesi dalgalarının ayarlanabilir bir spektral aralıkta ve ve komşu bantlarda yüksek geçirgenlik alınarak tek bir yönden mükemmel soğurulmasını öneriyoruz. Bu işlevsel özellik; 2 boyutlu, desteklenen-mod rezonansı tabanlı bir ızgara-dalga kılavuzu yapısı, ara dielektrik katmanı ve soğurucu bir oksit katmanı kullanılarak elde edilmiştir. 1.82μm'da uyarılan ve 19 nm'lik bir spektral genişliğe sahip (yarım-maksimum noktasındaki tam-genişlik) band aralığında, elektromanyetik radyasyon zıt iki yönden birinden cihaza gelince tamamen soğurulduğunu, diğer yönden geldiğinde ise tamamen yansıtıldığını gözlemledik. Ileri yönden-geri yönden soğurulma miktarlarının oranı 60'a kadar çıktı, aynı zamanda cihazın kalınlığı çalışılan dalga boyunun büyüklüğüne yakın tutuldu. Uyarılan rezonansların spektral pozisyonlarının ve genişliklerinin ayarlanabilmesinin yanı sıra, önerdiğimiz cihaz aynı zamanda komşu frekans bantlarında %65 geçirgenliğe sahip, saydam bölgeleri desteklemektedir. Kullandığımız 2 boyutlu ızgara yapısının aynı zamanda gelen ışığın polarizasyon durumuna duyarsız olduğunu doğruladık. Geometrik parametrelerin modifiye edilmesi dizaynımıza büyük bir ayarlanabilirlik kazandırmıştır, bu sayede soğurma/yansıtma bant aralığının 300 nm'ye kadar çıktığı bir dizaynı da gösteriyoruz.

Anahtar sözcükler: metayüzey, pasif radiatif soğutucu, kolorimetrik sensör, ışık filtresi, asimetrik soğurucu/yansıtıcılar, mükemmel soğurucu.

Acknowledgement

First of all, my limitless gratitude goes to my academic advisor Professor Ekmel Ozbay. I found great inspiration in his ways of thinking in general terms, his positive energy with respect to both work and personal relationships, his work ethic, and most importantly believing in my abilities during my most difficult times.

My sincere appreciation goes to Dr. Amir Ghobadi. His genuine interest, willingness for having discussions at any time, and feedback to our projects contributed immensely to my fruitful Master's. I have learned many invaluable things from him regarding scientific research and academia.

I would also like to thank Prof. Vakur Behçet Ertürk and Prof. Hamza Kurt for being in my thesis committee, their open and positive attitudes, and valuable comments to my thesis. I would like to open a parantheses for Prof. Erturk and thank him for his keen interest in answering my questions and his sincere contributions to me as a researcher in the photonics field while I was taking the "Advanced Electromagnetics Theory" course.

I thank all the talented engineers of Bilkent University, NANOTAM/ABMN, and UNAM for their contributions to my projects. Especially, I thank Dr. Bayram Butun, Mr. Okan Atesal, Mr. Ahmet Toprak, Mr. Murat Gokbayrak, and Dr. Deniz Caliskan from NANOTAM/ABMN, MS. Cangul Akturk from UNAM. I would like to thank MS. Nursel Aşıcı and MS. Gamze Seğmenoğlu from NANOTAM/ABMN, and MS. Mürüvet Parlakay and MS. Asli Tosun from the Electrical and Electronics Engineering department who were always very helpful to me, and made my life in Bilkent University easier.

I thank my friends and office mates who made my graduate life fun and friendly for me. Firstly, I would like to thank Mahmut (Bismuth) Can Soydan for being an amazing office-mate and a scientist, as well as being a great friend that would cheer me up during my demanding article writing crams. Volkan Erturk, Veysel

Ercaglar and Oguz Odabasi were also great friends from NANOTAM and I will be missing the times we spent together in both inside and outside the office. Salahuddin Zafar, in spite of our age difference, was also an amazing friend and was beside me during the times I needed, and I will be missing to have late night discussions just outside the office. From NANOTAM, I also appreciate everything from Mr. Tayfur Kaya, Mert Satilmis, Halit Dolas, Zeinab Eftakhari, Mohsin Habib, Dr. Ali Reza Rahimi Rashed. From Bilkent University, I would like to thank Farzan Shabani, Arash Ashrafnejad, Hamed Dehghanpour, Enes Seker, Bilge Yagci, and Pedram due to the fun times we have had. From UNAM, I would like to thank Hamza Humayun and Ulviyya Quliyeva for their friendship.

I am thankful to my former flat-mate Suphi ("Rocky Balboa") Keskin for the great memories we shared while studying, applying for PhD, hanging out, and, overall the chats we had about topics that would broaden to horizons of a typical engineer.

Although it is difficult to put it into words, I owe my greatest gratitude to my family, and especially my mother Pervin and father İzzet, who have been pillars of support and strong motivators in every step of the way. I would also like to thank my cousin Basak for also being a great friend and motivator. I thank my younger brother, Can, who is the greatest brother that anyone can ask for, due to his politeness, kindness and being a cool young person overall. My grandparents and their memories gave me strength in bringing this work to completion.

I would like to thank and acknowledge TUBITAK-BIDEB for financially supporting M.S. studies

When one is a graduate of Middle East Technical University, and attended graduate school in Bilkent University, which are both places of multicultural natures and such collegial support, it is impossible to write a complete acknowledgment in two pages and not leave someone out. To everyone that deserved a mention but failed to find it in the text above, please know that I appreciate and treasure your contributions to this thesis and to my life.

Contents

1 Introduction **1**

1.1 Background 2

1.1.1 Passive Radiative Coolers and Optical Solar Reflectors . . 3

1.1.2 Colorimetric Refractive Index Sensors 5

1.1.3 Color filters based on Graphene Perfect Absorbers 8

1.1.4 Resonant One-way Absorber/Reflectors with Transmissive Sidebands Functionality 10

1.2 Thesis Outline 11

2 Disordered and Densely Packed ITO Nanorods as an Excellent Lithography-Free Optical Solar Reflector Metasurface **13**

2.1 Introduction 13

2.2 Results and Discussion 14

2.2.1 Theoretical and Numerical Design and Optimization of the OSR Metasurface 14

2.3 Experimental Section 29

2.3.1 Fabrication of the metasurface OSR 29

2.3.2 Optical Characterization 30

2.3.3 Numerical Simulations 30

3 Colorimetric and Near-Absolute Polarization Insensitive Refractive-Index Sensing in All-Dielectric Guided-Mode Resonance based Metasurface 32

3.1 Introduction 32

3.2 Results and Discussion 34

3.2.1 Exciting guided-mode resonances of a grating-waveguide structure with polarization-insensitivity 34

3.2.2 Refractive-index sensing with the proposed Device 38

3.2.3 Fabrication and Characterization of the Proposed Guided-mode Resonance based Nanosensor 46

3.3 Methods 49

3.3.1 Fabrication of the Nanosensor Device 49

3.3.2 Optical Characterization 49

3.3.3 Numerical Simulations 50

3.3.4 Theoretical Analysis of excitation of guided-mode resonances in the proposed 2D- grating 51

4 Near-absolute polarization insensitivity in graphene based ultra-narrowband perfect visible light absorber 54

4.1 Introduction 54

4.2 Results and Discussion 55

4.2.1 Exciting guided-mode resonances of a slab-waveguide to improve light-graphene interaction. 55

4.2.2 Technological tolerances, effect of geometrical parameters on GMRs 65

4.2.3 Achieving perfect absorption with ultra-narrow bandwidth 70

5 One-Way and Near-Absolute Polarization Insensitive Perfect Absorption by using an All-Dielectric Metasurface 78

5.1 Introduction 78

5.2 Results and Discussion 79

6 Conclusion 86

A Scientific Contributions 108

A.1 Journal Articles 108

A.2 Refereed Conference Papers 109

List of Figures

2.1 **Schematics of Devices 1 and 2 and the parameter sweeps on the geometrical dimensions of Device 2.** **(a)** Device 1 to achieve broadband absorption in thermal-infrared and broadband reflection in solar spectrum. **(b)** Device 2 to test the effect of geometrical dimensions of a nanodisc on absorption spectrum, thermal emissivity and solar absorptivity. **(c)** Top-view of Device 2, showing the geometrical parameters in detail. Absorption spectrum of Device 2 under varying **(d)**: Nanodisc radius, r, **(f)**: Thickness of nanodiscs, h, **(h)**: thickness of the SiO_2 spacer, t_{SiO_2}. OSR parameters Device 2 when **(e)**: r, **(g)**: h, and **(i)**: t_{SiO_2} are changed. 15

2.2 **Fabrication of the metasurface OSR and the formation of ITO nanoforests.** **(a)**: Placement of samples in the sputtering chamber before coating of ITO, **(b)**: Schematic illustration of line-of-sight coating in a sputtering system and the formation of tilted nanowires. **(c)**: Low and **(d)**: High resolution top-view SEM micrographs of one of the fabricated devices. **(e)**: cross-sectional SEM image a sample metasurface OSR. 19

2.3 **Optical Characterization of the fabricated devices with disordered ITO nanorods, comparisons to numerical simulations of Device 2 and experimental result of a planar design, physical explanations on ϵ_{IR} enhancement in the proposed Device.** **(a)**: Experimental absorption result for Device 1 with h=50 nm and t_{SiO_2}= 2μm compared to the numerical simulations of Device 2 with the same h and t_{SiO_2}, **(b)**: Experimental absorption result for Device 1 with h=30 nm and t_{SiO_2}= 2μm compared to the numerical simulation Device 2 with the same h and t_{SiO_2}. **(c)**: Experimental absorption result for a planar device with h=50 nm and t_{SiO_2}= 2μm compared to numerical simulations for same device, **(d)**: Comparison of the absorption spectra of the planar device and Device 1 with h=50 nm and t_{SiO_2}= 2μm. **(e)**: Contribution of each layer to the absorption in thermal-infrared. **(f)**: Localization and enhancement of electric-field between nanodiscs of P=300 nm, r=142.5 nm. **(g)**: $|E|^2/|E_0|^2$ value recorded at a planar ITO layer. **(h)**: Near-field enhancement, $|E|^2/|E_0|^2$ values as a function of gap size between nanodiscs. In **(f)**, **(g)** and **(h)**, the $|E|^2/|E_0|^2$ values are recorded at 15 μm, and at the midgap position. 21

2.4 **Large-Scale fabrication and optical characterization of the proposed Device** **(a)**: Positioning of the wafer in the sample holder as seen from the back-view. **(b)**: Measurement areas in the fabricated wafers. Experimental absorption result for Device 1 with h=50 nm and **(c)**: t_{SiO_2}= 2μm, **(d)**: t_{SiO_2}= 1.55μm, when fabricated on a wafer. Absorption spectrum under obliquely-incident radiation at an incidence angle of **(e)**: 30°, and **(g)**: 45°. Device 1 as seen with **(g)**: naked eye, **(h)**: thermal camera. **(i)**: Thermal microscope image of Device 1. The ellipsometry measurements are taken from Area 5. 26

3.1 **The proposed design and its unit-cell (a)** Device I to excite GMRs. **(b)** Unit-cell of Device I, detailing the 2D grating, as seen from the top-view. **(c)** Dielectric layers, as seen from the side-view, and illumination by p-polarized plane wave. Transmission and Reflection spectra for Device I **(d)** under p-polarized; **(e)** under s-polarized incident plane wave. $|E|^2/|E_0|^2$ at XZ plane during **(f)**: on-resonance at 602.5 nm; **(g)**: off-resonance at 750 nm; $|H|^2$ at XZ plane during **(h)**: on-resonance, **(i)**: off-resonance. $|E|^2$ and $|H|^2$ are the modulus of electric and magnetic field inside Device I, $|E_0|^2$ and $|H_0|^2$ denote that of incident light. GWS extends from z=0 to z=460 nm. 34

3.2 **Achieving near-absolute polarization insensitive refractive index sensing in Device I with the 2D-grating (a)** Comparison of the unit-cells of Device I and the design incorporating 1D grating under different rotations. **(b)** Reflection map of Device I for the polarization angles spanning from 0° (p, TM-polarization) to 90° (s, TE-polarization). **(c)** Device II with the adsorbed biolayer. Spectral shift of the guided-mode resonance depending on the **(d)**: refractive index, n_{bio}, **(e)**: thickness, t_{bio}, of the biolayer. 37

3.3 **Dependence of the reflection spectrum and the refractive-index sensing properties of Device I on the structural parameters.** Reflection spectrum of Device I under varying **(a)**: Grating thickness, $t_{Si_3N_4}$,**(c)**: unit-cell periodicity in the y-direction, P, **(e)**: Width of each stripe, w. When changing one parameter, we kept the other parameters at their optimum value. FWHM, sensitivity and FoM of Device II when **(b)**: $t_{Si_3N_4}$, **(d)**: P, and **(f)**: w are changed. FWHM is measured for Device I without the biolayer attachment, while sensitivity is measured for Device II by comparing the S3 and S4 cases, with t_{bio}=30 nm. In the unit-cell periodicity sweeps, width of grating is kept as $w = \frac{2P}{15}$. All results are taken with p-polarized incident wave. 41

3.4 **Fabrication and optical characterization of the proposed nanosensor.** **(a)**: Top-view SEM micrograph of the fabricated bare device, **(b)**: Schematic diagram of the optical characterization setup. **(c)**: Experimental transmission spectra for the bare, Al_2O_3 coated and ZnO coated devices, under p-polarized incident light, **(d)**: The shift of the excited GMRs. **(e)**: Experimental transmission spectra for the bare, Al_2O_3 coated and ZnO coated devices, under s-polarized incident light, **(f)**: Insensitivity of fabricated devices to incident light-polarization by comparing the excitation wavelengths of GMRs under p- and s-polarized light for each device. In **(c)**, and **(e)**, spectrum of each device is connected to their associated optical microscope image. 46

4.1 **The proposed design, its unit-cell and the structure with the classical 1D grating** **(a)** Device I to excite GMRs and enhance light-graphene interaction. **(b)** Unit-cell of Device I, detailing the 2D grating, seen from top-view. **(c)** Dielectric layers and the monolayer graphene of Device I, seen from side-view. **(d)** The structure with the commonly used 1D-grating. In **(c)**, the device is illuminated by p-polarized plane wave. 56

4.2 **Excitation of GMRs and enhancement of light-graphene interaction.** Transmission, Reflectance and Absorption spectra for the proposed device **(a)** without graphene, **(b)** with graphene, under s-polarized (TE) light; **(c)** with graphene, under p-polarized (TM) light; **(d)** with 1D grating and graphene, under TE and TM polarized light to show polarization dependency. 58

4.3 **Distribution of electric and magnetic field in the on and off-resonant conditions.** $|E|^2/|E_0|^2$ at XZ plane during **(a)**: on-resonance at 703.82 nm; **(b)**: off-resonance at 751.9 nm; $|H|^2$ at XZ plane during **(c)**: on-resonance, **(d)**: off-resonance . $|E|^2$ and $|H|^2$ are the modulus of electric and magnetic field inside the device, $|E_0|^2$ denotes that of incident light. Graphene is located at z=0. . 60

4.4 **(a)** Comparison of the unit-cells of the proposed design and the 1D-grating design under different rotations of Device I. **(b)** Absorption map of Device I for the polarization angles spanning from 0° (p,TM-polarization) to 90° (s,TE-polarization). 62

4.5 **Dependence of absorption spectrum of Device I to structural parameters**. Absorption spectrum of Device I under varying **(a)**: PMMA thickness, t_{PMMA}, **(b)**: PMMA width, w, **(c)**: Ta_2O_5 thickness, $t_{Ta_2O_5}$, **(d)**: unit cell periodicity in y-direction, P. When varying one parameter, we kept the other parameters at their optimum value. In the unit-cell periodicity sweeps, width of grating is kept as w=0.2P. The results are taken with p-polarized incident wave. 66

4.6 **Structure of Device II, used to achieve perfect absorption by critically coupling graphene to excited GMRs.** t_{SiO_2} denotes the SiO_2 thickness. 70

4.7 **Achieving perfect absorption by critically coupling guided-mode to graphene**. Absorption spectrum of Device II under **a** s-polarized, **(b)**: p-polarized light. **(c)**: $|E|^2/|E_0|^2$ at XZ plane during resonance **(d)**: $|H|^2$ at XZ plane during resonance. **(a)** also shows the absorption spectrum in the absence of monolayer graphene. 72

4.8 Absorption spectrum of Device II under varying **(a)**: Glass thickness, t_{SiO_2}, **(b)**: Polarization angle. **(c)**: Tuning the perfect absorption in the visible and mid-infrared ranges. $t_{Ta_2O_5}$=160, 180, 300, 300, 400 nm; P=350, 400, 550, 500, 600 nm, t_{SiO_2}= 380, 420, 260, 240, 540 nm for Devices 3,4,5,6 and 7, respectively. t_{PMMA}= 350 nm and w= 0.2P, for all designs. **(d)**: Layer-dependent absorption of Device II. 73

5.1 **Achieving one-way absorption/reflection with adjacent transparency windows in a narrowband design. (a)** The proposed device to achieve one-way absorption/reflection with transparency in sidebands functionality. SiO_2 layer is drawn transparently to make the FSR visible as well. **(b)** Unit-cell of FSR, elaborating the 2D grating, as seen from the top-view. **(c)** Transmission and Reflection spectra of the FSR-SiO_2 structure under p-polarized incident plane wave. **(d)**: Spectral response of the FSR-SiO_2 structure when thickness of the SiO_2 spacer, t_{SiO_2} is changed. Spectral response of the narrowband device under **(e)**: forward, **(f)**: backward illumination. **(g)** Reflection map of FSR-SiO_2 structure for the polarization angles spanning from 0° (p, TM-polarization) to 90° (s, TE-polarization) 80

5.2 **(a)**: $|E|^2/|E_0|^2$ at XZ plane during resonance at 1.82μm. **(b)**: $|H|^2$ at XZ plane during resonance. $|E|^2$ and $|H|^2$ are the modulus of electric and magnetic field inside Device I, $|E_0|^2$ and $|H_0|^2$ denote that of incident light. GWS extends from z=0 to z=220 nm. Forward illumination absorption spectrum of the narrowband design under varying **(c)**: SiO_2 spacer thickness, $t_{Si_ON_2}$,**(d)**: ITO thickness, t_{ITO}. Effect of t_{ITO} on the **(e)**: Absorption and **(f)**: Transmission spectra of the narrowband design under backwards illumination. Spectral response of the broadband device under **(g)**: forward, **(h)**: backward illumination. 83

Chapter 1

Introduction

This chapter is on part reprinted with permission from: 1. **Deniz Umut Yildirim**, Amir Ghobadi, Mahmut Can Soydan, Okan Atesal, Ahmet Toprak, Mehmet Deniz Caliskan, and Ekmel Ozbay, ACS Photonics, 2019, 6 (7), 1812-1822, DOI: 10.1021/acsphotonics.9b00636, 2. **Deniz Umut Yildirim**, Amir Ghobadi, Mahmut Can Soydan, Murat Gokbayrak, Ahmet Toprak, Bayram Butun, and Ekmel Ozbay, The Journal of Physical Chemistry C, 2019, 123 (31), 19125-19134, DOI: 10.1021/acs.jpcc.9b04748. 3. **Deniz Umut Yildirim**, Amir Ghobadi, and Ekmel Ozbay, Near-absolute polarization insensitivity in graphene based ultra-narrowband perfect visible light absorber. Scientific Reports, 2018, 8, 15210. https://doi.org/10.1038/s41598-018-33609-2, 4. **Deniz Umut Yildirim**, Amir Ghobadi, Mahmut Can Soydan, Andriy E. Serebryannikov, and Ekmel Ozbay, "One-way and near-absolute polarization insensitive near-perfect absorption by using an all-dielectric metasurface," Optics Letters, 2020, 45, 2010-2013.

1.1 Background

The advances in nanofabrication in the last few decades provided the opportunity to observe strong light-matter interactions in synthetic, man-made materials known as metamaterials whose sub-wavelength inclusions offer exotic properties, such as negative refraction[1, 2], artificial magnetism[3], asymmetric transmission[4], cloaking[5, 6], and lasing[7, 8]. Their sub-wavelength thick counterparts, which are called metasurfaces, are also finding increased applications in ultra-thin flat lenses, spatial light modulators, spectral filters, and polarization control[9, 10, 11, 12, 13, 14, 15, 16]. Strong light-matter interactions also enable the harvesting of the confined electromagnetic radiation by an absorbing layer such as metals, or semiconductors, which could lead to the realization of perfect absorption of light[17, 18]. This resonant response can be narrowband, which has applications in sensing, imaging, and color-filtering[19, 20, 21, 22, 23, 24, 25, 26, 27, 28]. On the other hand, their broadband counterparts are promising in the areas of thermal photovoltaics[29], hot-electron based photodetectors[30] and passive radiative cooling[31, 32, 33].

However, some of the above-mentioned applications necessitate replacing the metals, which are the usual building blocks of metamaterials, with dielectric structures. This is because, metals cannot provide a spectrally selective absorption/reflection and their resonance quality-factors are limited due to their inherent ohmic losses[17, 33, 34]. Moreover, metals are prone to oxidation and corrosion under harsh conditions, which limit their long-term stability. Thinner structures are also desired in certain large-scale applications, in which the weight of the overall system dominate the cost. As a consequence, transparent dielectric metasurfaces stand out as strong candidates for many applications.

This thesis explores four important applications areas of dielectric metasurfaces, 1. Passive radiative coolers for spacecraft, 2. Colorimetric refractive index sensors, and 3. Color filters based on monolayer graphene. 4. Resonant one-way absorption/reflectors with transmissive sidebands.

1.1.1 Passive Radiative Coolers and Optical Solar Reflectors

Temperature stabilization and its uniform distribution are vital for spacecraft and satellites because most of their components become less reliable when operated outside of their acceptable temperature range. Propellant freezing, thermal cycling damage to the equipment, and instrument/antenna/camera misalignment are additional issues to be avoided during all of the mission phases[35, 36]. The coating system called Optical Solar Reflectors (OSRs), which are secondary-surface mirrors, therefore, play a crucial role for the optimum performance of spacecraft and satellites and success of their missions[35, 36, 37, 38]. OSRs simultaneously minimize the direct and indirect solar energy input to the spacecraft while passively emitting the thermal energy generated on the board. OSRs are then required to have a small solar absorptance (α_s) over the blackbody radiation spectrum of sun at 5778 K, corresponding to the ultraviolet (UV), visible (VIS), and near-infrared (NIR) parts of the electromagnetic-spectrum. Concurrently, OSRs should have a large thermal emissivity (ϵ_{IR}) in the mid-infrared (MIR) and far-infrared (FIR) parts of the spectrum (thermal-infrared) related to the blackbody radiation at room temperature, 300 K. OSRs can be regarded as spectrally selective filters, i.e. they are broadband mirrors in the solar spectrum, but perfect absorbers in the thermal infrared. A Figure of Merit (FoM) for an OSR can, therefore, be defined as ϵ_{IR}/α_s. Another critical consideration for an OSR is the stability over the course of the mission. This is because an OSR is affected during their missions by contamination, high-vacuum, UV-radiation, and charged particles. The general result is an increase in α_s, with a negligible effect on ϵ_{IR}. There are different strategies and material choices to design an OSR, and they can be classified under two categories: conventional methods of using white paint, second-surface mirrors using quartz or teflon[35, 36]; and metamaterial based solutions[37, 38].

Under the category of conventional methods, white color is often painted on the exterior surfaces and radiators of a spacecraft due to having a large ϵ_{IR}/α_s ratio. However, these paintings are very prone to environmental degradation due to

UV radiation that darkens the pigments[35, 36]. Second-surface reflectors based on silver (Ag) or aluminum (Al) backed quartz films combine the high reflection of the metal layer with the strong absorption/emission of quartz in the thermal infrared to achieve very high ϵ_{IR}/α_s. In addition, quartz is highly insensitive to UV radiation and darkening, so it has very stable thermo-optical properties. Nevertheless, having large emissivity in the thermal infrared range requires using thick tiles of quartz ranging from 250 μm to a few cm. Moreover, the rigid and brittle tiles are prone to breaking while handling and are inflexible. This adds significant weight and, consequently, launch and assembly costs for the spacecraft. The other type of secondary-surface mirrors replace quartz with fluorinated ethylene propylene (FEP) Teflon film. The resultant Ag/FEP and Al/FEP materials provide flexibility and an excellent beginning-of-life ϵ_{IR}/α_s ratio. However, FEP is highly susceptible to degradation during its lifespan, primarily due to charged-particle damage and atomic oxygen. This makes the lifespan of Ag/FEP and Al/FEP materials shorter compared to quartz tiles [35, 36, 37]. Thus, the conventional methods cannot simultaneously offer high-performance, low-weight and the associated costs at the same time.

Attempts on achieving broadband absorption by metamaterials mostly focused on metal-insulator-metal (MIM) based cavities, with top-metal layer patterns of trapezoids[39, 40], nanodiscs[41, 42], pyramids[43], gratings[44], nanopatches[45, 46, 47], multiple narrowband resonators[48], elongated shapes[49], and tapered structures[50, 51, 52]. Nonetheless, the broadband absorption comes at the expense of requiring a lithography step during fabrication. This constitutes a major complication when applications for spacecraft coating are considered, due to not being large-area compatible, and not offering mass-production with high-throughput, upscaling, and repeatability. One solution to this problem can be utilizing planar multilayer designs[53, 54] . However, these designs only rely on interference and having a broad absorption in thermal infrared may require multiple deposition cycles with large thickness, resulting in bulky devices. As an alternative method, disorder and randomness are shown to result in a broader absorption spectrum compared to planar designs, which is due to the light trapping and confinement in nano units, as well as exciting multiple resonances whose

superposition contribute to a broad response[55, 56]. Nevertheless, these designs require multiple fabrication steps and utilize slow chemical processes, so there is still room for improvement in achieving disorder and randomness in the devices with higher-throughput. OSR applications also place major restrictions on the material choices because the requirement of simultaneously realizing solar reflection and a broadband absorption in thermal infrared.

Recently, transparent conductive oxides (TCOs), such as indium tin oxide (ITO), Aluminum-doped ZnO (AZO) and gallium-doped ZnO (GZO) emerged as strong candidates for infrared plasmonics, while being highly transparent in the solar spectrum[57, 58, 59]. Their relatively high loss in thermal infrared promises plasmonic resonances with low quality factors, and a broad absorption spectrum. Conversely, their low-loss dielectric response in the visible range would not contribute significantly to absorption. This means high ϵ_{IR}, but low α_s are simultaneously achievable. Indeed, an AZO based OSR with a square shaped unit-cell is recently demonstrated[37] with an ϵ_{IR}/α_s ratio as high as 4.9, although electron-beam lithography (EBL) is employed in the fabrication. As a result, a lithography-free route is still sought in the literature for large-scale compatibility.

1.1.2 Colorimetric Refractive Index Sensors

Biosensors play a vital role in improving the overall well-being of the society. The detection techniques used in biosensors can be broadly divided into label-free and label-based techniques[60]. Traditional methods of label-based techniques enabled us to gain an improved understanding on many biological processes and cellular actions[61, 62, 63, 64]. However, using fluorescent dyes, radioactive labels, and staining agents essentially limit the scope of the experiment as they require prior knowledge of the target's presence and the label may interfere with the process[65]. Therefore, there has been significant effort made toward developing label-free biosensors that can allow any sample to be analyzed with minimal preparation and assay times.[60]. Over the last decade, label-free biosensing has made great improvements thanks to the developments in

nanotechnology[66]. Strong light-matter interactions in nanophotonic structures have shown high-sensitivity, cost-effectiveness and practicality in many areas, such as biomedicine[67, 68, 69, 70], drug detection[71], reaction monitoring[72], and environmental control[73]. Among the label-free assays, colorimetric biosensing has, in particular, attracted much attention because the rapid color change output upon changing the external environment can be read out in the field, i.e. at the point-of-care, by naked eye. Therefore, this technology is not confined to the laboratory, does not require expensive or advanced instrumentation, and the data readout can be carried out in a wider clinical practice without requiring trained personnel[74]. Insensitivity to incident-light polarization is also highly desirable as it would eliminate the requirement of polarizing equipment. In a practical setting, sensitivity to polarization would also mean that a sample reflects different colors depending on its azimuthal orientation with respect to the observer, when an arbitrarily polarized light is incident on it. A polarization-insensitive structure, on the other hand, would reflect the same color at all azimuthal orientations. Combining all of these, a colorimetric sensor with polarization-insensitivity results in simpler instrumentation for interfacing, faster and more reliable readout with more self-contained devices of smaller footprints, and a lower-cost.

In the broad field of optical and label-free sensing, there are many competing technologies. Among these, sensors based on surface-plasmon polaritons (SPPs) or localized surface plasmon resonances (LSPRs) of metallic structures[68, 69, 71, 72, 75, 76] have seen the most extensive industrial adoption. Both methods can yield resonances in the visible range of electromagnetic spectrum with polarization-insensitive unit-cell arrangements and, therefore, enable colorimetric detection with high-sensitivity. However, plasmonic sensing has inherently limited performance in terms of resonance linewidth, which is broadened by the optical losses due to free electrons and local heating[67, 70]. Localized heating may also alter the composition of analytes[77] and prevent *in vivo* sensing. Moreover, metals are prone to be oxidized and corroded under high temperatures and harsh environments which, in turn, limit their long-term performance stability. On top of that, the excitation of SPPs requires p-polarized light, hence

a polarizer, and phase-matching mechanisms, such as prisms[78], resulting in sophisticated optics. As a consequence, transparent dielectric nanoresonators stand out as strong candidates for not only biosensing, but also for nanophotonics[79].

All-dielectric nanophotonics is a rapidly developing field because the resonant nanostructures, such as silicon nanoparticles, not only support electric type (dipole, quadrupole, etc.) resonances, as in metallic nanoparticles, but also magnetic multipole Mie resonances [79], with tailorable[80] and actively-tunable[81, 82] resonance features. Similar to their plasmonic counterparts, the spectral position of these resonances also strongly depend on the properties of the dielectric environment, yet they can achieve higher quality-factors due to lower optical losses[79, 83]. These offer interesting opportunities for biosensing and refractive-index sensing. The present studies in this field mostly utilized silicon[67, 70, 84] with sensitivities comparable to LSPR sensors. Although silicon has a negligible loss in the near-infrared region, its high refractive-index in the visible region comes at the price of increased absorption due to interband transitions. Indeed, TiO_2 and GaP are shown to have better scattering efficiencies in the visible range[85], yet their application to colorimetric sensing without optical losses requires further research.

Dielectric materials with negligible optical losses, when arranged periodically, can also show guided-mode resonance (GMR) phenomenon [86, 87, 88]. GMRs define the phase-matched coupling between the free-space radiation and a waveguide's supported (guided) modes, and they have a leaky nature due to the periodicity of the structure[86, 87, 88]. They result in resonances with narrow linewidth and high sensitivity to the changes in the surrounding medium's refractive index, which are very-well suited to colorimetric sensing applications[89, 90] with negligible optical losses. Sensitivity also benefits from utilizing a grating with sharp features, owing to the high localization of the electromagnetic fields around these regions[91]. The problem with GMR-based devices that utilize 1-dimensional (1D) gratings as their coupling element is sensitivity to incident-light polarization[92, 93].

1.1.3 Color filters based on Graphene Perfect Absorbers

Ever since the experimental isolation of graphene in 2004 [94], this monolayer of carbon atoms in a honeycomb lattice has attracted enormous attention because of its unique electronic, optical, and mechanical properties [95, 96, 97], and paved the way for the advent of other two-dimensional materials [98, 99]. The ultra-wideband spectral response and the huge carrier mobilities make graphene a strong candidate as a backbone of novel nanophotonic and optoelectronic devices. Indeed, graphene-based solar cells [100] , saturable absorbers for the mode-locked ultra-fast lasers[101, 102], photodetectors[103, 104] , transparent electrodes[105, 106], optical modulators[107, 108] and third harmonic generation[109, 110] are demonstrated. Further incorporation of graphene into high-performance optical devices makes strong light-graphene interaction compulsory. Localized surface plasmons and surface plasmon polaritons supported by graphene in the terahertz (THz) and mid-infrared (MIR) regimes can enhance this interaction and perfect absorption can be achieved[111, 112, 113]. In contrast, in the visible and near-infrared range (Vis-NIR), graphene's optical response is dominated by interband transitions, giving a real conductivity with no plasmonic response and graphene effectively mimics a dielectric with considerable loss [114]. Unpatterned and suspended graphene absorbs $A = \pi\alpha = 2.3\%$ of the normally incident light without spectral selectivity, defined by the fine structure constant $\alpha = e^2/\hbar c$. $A = \pi\alpha = 2.3\%$ is actually a significant value for a one-atom thick material. Nevertheless, the absolute strength of the absorption is low and it limits graphene's further application in optoelectronics, an example related to our work being low responsivity in photodetectors[115, 116].

Since graphene plasmons cannot be excited outside the THz and MIR ranges, graphene has to be coupled to other resonant mechanisms to improve the light absorption in the Vis-NIR ranges. Enormous research efforts have been devoted to enhancing the local optical field around graphene and increase light-graphene interaction. The methods to achieve these can be classified into four categories. First, graphene can be placed inside a Fabry-Pérot (FP) cavity[117, 118]. This method can confine large optical fields and significantly enhance the absorption

in graphene. However, these designs require deposition of a large number of dielectric layers (25 pairs of AlAs and AlGaAs for the bottom reflector and 7 pairs of SiO_2 and Si_3N_4 layers for top reflectors, reported in ref. [117]) on top of graphene. This results in not only fabrication difficulty, but also bulky devices. Another option is placing graphene near plasmonic nanostructures [119, 120] and relying on the near-field enhancement effect of surface plasmons or surface plasmon polaritons. This method suffers from absorption peak broadening because of the background absorption coming from the metals, which is detrimental to color sensitivity. Moreover, significant Joule losses decrease device efficiencies[121].

The third and fourth methods can be classified together as coupling of graphene to guided-mode resonances. The difference between two methods is the structures where GMRs are excited. The third method is to couple graphene to the GMRs of photonic crystal slabs (PhCs) [122] or 1-dimensional photonic crystals (1DPCs), excited by sub-wavelength grating (SWG) couplers[123, 124]. The guided-mode leaks out evanescent waves to graphene. Critical coupling of the guided-modes to graphene then produces perfect absorption. Notably, the latter can achieve an ultra-narrow absorption bandwidth of 0.03nm due to placing graphene far away from 1DPC[124]. Although promising in theory, this method enforces extreme fabrication accuracy on not only the SWG, but also on the 1DPCs to achieve the target wavelength and store very high energy in 1DPC to achieve critical coupling. Similar to the methods that adopt FP cavity, this method also results in bulky components. The final method is to excite the GMRs of either unmodulated slab-waveguide structures beneath the grating, [125, 126, 127], or the grating itself [128], which acts as a waveguide whose core is refractive-index modulated bulk. These GMRs then interact with graphene to increase light-graphene interaction. Compared to the third method, this method offers more compact designs and a more facile fabrication process. This is because it does not require 1DPC, but only a SWG, two or three dielectric films with only one being patterned, and possibly a perfect back metal mirror or Bragg reflector. However, the downside is the larger bandwidth because low-Q resonances can be coupled to graphene, due to the smaller distance between GMR and graphene. Thus, there is a fundamental trade-off between the two methods in terms of the fabrication

complexity and Q-factor of resonances. While the previous studies for the guided-mode resonances focused mainly on the absorption enhancement, polarization insensitivity remained an issue, because of incorporating 1-dimensional SWGs. Although polarization-insensitivity between s and p-polarizations is achieved by the square lattice in ref. [122], the bandwidth, measured as full-width at half-maximum (FWHM), 14 nm is quite high because of the circular shape of the holes. The sharp features of gratings allow for enhanced field localizations and high-Q resonances. Hence, an ideal unit-cell would use a rectangular grating structure with rotational symmetry to preserve both strong light absorption and achieve polarization insensitivity.

1.1.4 Resonant One-way Absorber/Reflectors with Transmissive Sidebands Functionality

Differing from some of the above-mentioned metamaterial and metasurface applications, some applications may require multifunctional devices, that is, having different functions at a specific wavelength range, while having different functions in the adjacent bands. [129, 130]. A practical multifunctional device may be one yielding perfect, one-way electromagnetic wave absorption in a required frequency band, while supporting transparency in the neighboring bands. In such a device, perfect absorption is to be achieved during resonance, while illumination from the opposite direction causes total reflection [131]. Although the widely used metal-insulator-metal (MIM) cavity architecture [39] may provide near-unity perfect absorption (reflection) in forward (backward) illumination, there are no adjacent transparency windows and no frequency-selectivity due to the inherent characteristics of the optically thick bottom metal mirror.

Dielectric metasurfaces, comprised of periodically arranged sub-wavelength inclusions can be engineered to display the guided-mode resonance (GMR) phenomenon [86]. GMRs define the phase-matched coupling of the free-space radiation to the supported (guided) modes of a waveguide, and the periodicity of the structure results in the leaky nature of these resonances. By utilizing these,

frequency-selective perfect reflectors (FSRs) can be actualized with the desired bandwidth characteristics [28]. It is also desirable to have polarization insensitivity as a feature of these FSRs, which, while readily available in bulk metal bottom reflectors. While much work is focused on 1D grating structures that are inherently polarization-sensitive [92], by focusing on 2D arrays it is possible to have near-absolute polarization insensitivity.

1.2 Thesis Outline

Chapter 2 is dedicated to the design, fabrication and characterization of a metal (Aluminum)- insulator (Silicon Dioxide) - Oxide (ITO) cavity that is to be used as an optical solar reflector metasurface. Disordered and densely packed ITO nanoforests are utilized as the top-layer of the cavity and the overall metasurface is shown to experimentally yield an ultra-high thermal emissivity, ϵ_{IR} of 0.968, while the solar absorptivity, α_s, is limited to 0.168. With these values, a record-high Figure of Merit of 5.73 is verified.

In chapter 3, we use a novel, 2-dimensional all-dielectric grating metasurface structure, excite its guided-modes and use it to sense the changes in the dielectric environment surrounding the grating. We qualitatively confirmed colorimetric sensing along with near-absolute insensitivity to the polarization state of the incident light. Quantitatively, experimental sensitivity of 235.2 nm/RIU and a linewidth of 19 nm are verified.

In chapter 4, we aim to enhance light-graphene interactions by the method of coupling graphene to the guided-modes of a slab-waveguide, excited by the grating coupler structure that is similar to the one in Chapter 3. This compact structure allowed us to numerically confirm narrowband perfect (98.7%) absorption with a linewidth as small as 0.8 nm, as well as geometrical tunability over a very broad range of 400 nm in the visible and NIR spectral ranges. Our novel grating structure also allowed us to have insensitivity to incident-light polarization.

In chapter 5, we propose a straightforward metasurface approach to obtain absorption/reflection under forward/backward illumination cases, when a resonance is excited. Simultaneously at the frequency bands away from the resonance, the structure is mostly transmissive. To achieve this, we use a near-absolute polarization insensitive grating-waveguide structure as a frequency-selective reflector to mimic the bottom thick metal layer in an MIM cavity. Our proposed device achieved (90%) absorption/(98.5%) reflection under forward/backward illumination cases. By adjusting geometrical parameters, we also show the possibility of tuning the resonance frequency and the linewidth, as we both show a narrowband design with 19 nm FWHM value, as well as a broadband design that yields a bandwidth as high as 300 nm.

Finally, chapter 6 presents a conclusion on the thesis.

Chapter 2

Disordered and Densely Packed ITO Nanorods as an Excellent Lithography-Free Optical Solar Reflector Metasurface

This chapter is on part reprinted with permission from: **Deniz Umut Yildirim**, Amir Ghobadi, Mahmut Can Soydan, Okan Atesal, Ahmet Toprak, Mehmet Deniz Caliskan, and Ekmel Ozbay, ACS Photonics, 2019, 6 (7), 1812-1822, DOI: 10.1021/acsphotonics.9b00636.

2.1 Introduction

In this section, we use disordered and densely packed Indium Tin Oxide (ITO) nanorod forests as the top layer of a metal-insulator-oxide cavity. The outstanding light trapping capability of the scaffold increased the residing time of thermal-radiation in the device. This trapped light is then harvested by the hybrid system of ITO and SiO_2. As a result, perfect broadband absorption over

the entire thermal-infrared, ranging from 2.5 μm to 25 μm is achieved and the experimental thermal-emissivity, ϵ_{IR}, reached as high as 0.968. At the same time, solar absorptance, α_s, is also minimized to an experimental value of 0.168, owing to the low-loss dielectric characteristic of ITO in this spectral range. In fabricating the nanorod forests, we exploited the inherent line-of-sight type coating of Physical Vapor Deposition (PVD) systems, such as thermal evaporator and sputtering[132], to eliminate the need for lithography. In the method, which is known as oblique-angle deposition[133, 134, 135], the substrate is placed at an angle to the source, enabling the creation of quasi-3D structures[136, 137] with drastically different properties[138, 139]. This chapter is organized as follows: In the first part of this chapter, we utilize the finite-difference-time-domain (FDTD) method to numerically investigate broadband light absorption in thermal-infrared and broadband reflection in solar spectrum, in a metasurface comprised of periodic nanodiscs. We scrutinize the effects of the geometrical dimensions of a single nanodisc, and cavity thicknesses on absorption spectrum, ϵ_{IR}, α_s, and FoM, to shed light on optimizing the actual device. In the second part, we demonstrate our oblique-angle deposition strategy in detail and present the experimental results for the optimized OSR. We compare these results with the numerical results of the periodic disc design, and experimental results for designs utilizing planar ITO. Overall, our robust, large-area compatible and ultra-high performance OSR holds great promise in not only space missions, but also in radiative cooling and thermal imaging.

2.2 Results and Discussion

2.2.1 Theoretical and Numerical Design and Optimization of the OSR Metasurface

Our proposed device in Fig. 2.1(a) is designed to obtain the required spectral response of an OSR, that is, broadband reflection in the solar spectrum, while

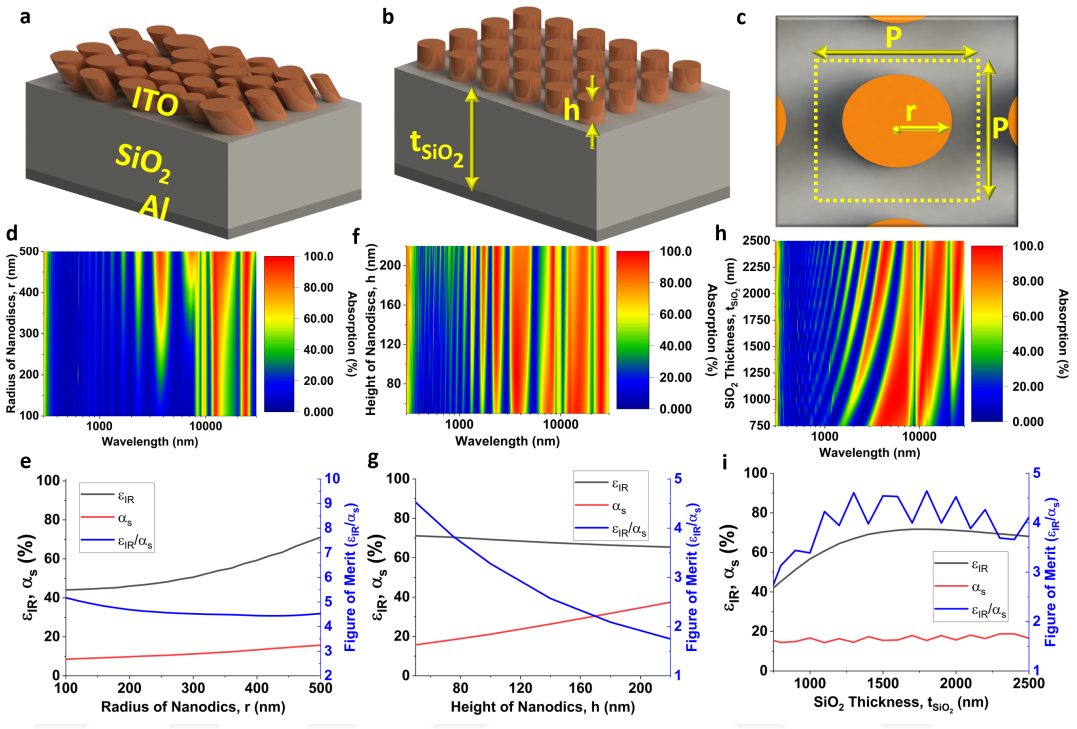

Figure 2.1: Schematics of Devices 1 and 2 and the parameter sweeps on the geometrical dimensions of Device 2. **(a)** Device 1 to achieve broadband absorption in thermal-infrared and broadband reflection in solar spectrum. **(b)** Device 2 to test the effect of geometrical dimensions of a nanodisc on absorption spectrum, thermal emissivity and solar absorptivity. **(c)** Top-view of Device 2, showing the geometrical parameters in detail. Absorption spectrum of Device 2 under varying **(d)**: Nanodisc radius, r, **(f)**: Thickness of nanodiscs, h, **(h)**: thickness of the SiO_2 spacer, t_{SiO_2}. OSR parameters Device 2 when **(e)**: r, **(g)**: h, and **(i)**: t_{SiO_2} are changed.

achieving broadband absorption in the thermal-infrared, due to its highly diffracting/scattering and electromagnetic wave (EMW) trapping nature. This proposed structure, which we call Device 1, consists of a metal-insulator-oxide (MIO) cavity, where a thick metal back-reflector, aluminum (Al), is used to redirect the otherwise transmitted EMWs back into the cavity. The spacer, SiO_2, is used to create the necessary phase accumulation to redirect the EMWs mostly to the top absorbing layer of our MIO cavity, which makes use of ITO nanorods. ITO is a plasmonic material in the thermal-infrared, so the nanorods can be used to excite localized surface plasmon resonances (LSPRs). LSPRs define the non-propagating

excitations of the conduction electrons that are coupled to the incident electromagnetic radiation. When the nanoparticle dimensions become comparable to wavelength, the plasmons are confined to the surface of nanoparticles and the collective harmonic oscillations result in a dipolar response with a specific resonance wavelength. The resonance wavelength and its Q-factor are highly related to the morphology (size, shape, spacing, and density) of the nanostructures[78]. Therefore, in understanding the operation of Device 1, it is pivotal to first grasp how individual nanorod dimensions and the cavity thickness affect the spectral response as well as the OSR parameters, ϵ_{IR}, α_s, and ϵ_{IR}/α_s.

To understand how the performance is affected by the geometrical parameters, we initially scrutinized the LSPRs supported by nanodiscs/nanorods of radius r, thickness h, that are periodic in two directions with a period of P, when the spacer thickness is chosen as t_{SiO_2}. We name this testing device as Device 2, whose schematic is shown in Fig. 2.1(b), and its unit-cell from the top view is shown in Fig. 2.1(c). To clarify the difference between Devices 1 and 2, Device 1 is the device that will be fabricated and characterized in the upcoming parts of this chapter. It has nanorods whose size, shape, radii and spacing are defined randomly during the fabrication, while h is controlled by deposition rate and time. On the other hand, Device 2 has periodic nanodiscs with precise radii and spacing, which can be controlled by EBL. It is defined to compare the optical performance of a patterned top layer to that of Device 1.

In the numerical analysis of Device 2, we utilize finite-difference-time-domain (FDTD) simulations. Details of the simulation setup are outlined in the Experimental Section. With the aid of FDTD method, we calculated the spectral absorption, $A(\lambda, T)$, of Device 2. Based on the calculated absorption data and the spectral radiance $B(\lambda, T)$, given in Eq. 2.1, the ϵ_{IR} and α_s values are calculated based on Eq. 2.2.

$$B(\lambda, T) = \frac{2hc^2}{\lambda^5} \frac{1}{e^{\frac{hc}{\lambda k_b T}} - 1} \tag{2.1}$$

$$\epsilon_{IR}, \alpha_s = \frac{\int_{\lambda_1}^{\lambda_2} A(\lambda, T) B(\lambda, T) d\lambda}{\int_{\lambda_1}^{\lambda_2} B(\lambda, T) d\lambda} \tag{2.2}$$

where h, c and k_b are Planck's constant, speed of light in vacuum and Boltzmann constant, respectively. The integration limits λ_1 and λ_2 are taken as 300 nm-2500 nm and 2.5 μm-25 μm respectively for the solar spectrum and thermal infrared. λ is the spectral wavelength and T is the temperature, which is 5778 K for solar spectrum and 300 K for the thermal radiation. Eq. 2.2 then represents the spectrally weighted absorbance of the metasurface OSR. In the numerical simulations, the dispersion effect of Al, SiO_2, and ITO are retrieved with ellipsometry measurements.

We first fixed t_{Al} at 125 nm (throughout this chapter), P at 1100 nm, h at 50 nm, t_{SiO_2} at 2000 nm and swept r. Our primary purpose in these set of simulations is to find out the effect of the density, or fill factor of the nanodics in the absorption spectrum and the OSR parameters. In Fig. 2.1(d) we show the spectral response of Device 2 for different values of r. Firstly, it is seen that the high-loss plasmonic optical nature of ITO in thermal infrared results in a broad absorption spectrum, while in the solar spectrum, the oscillations in absorption corresponds to response of a Fabry-Pérot cavity; due to ITO's low-loss dielectric nature. Fig. 2.1(e). shows how OSR parameters respond to changes in r. In the thermal-infrared, it is evident that as the nanodiscs get closer to each other with decreasing r, in other words, as the discs become denser, their "interconnectedness" increases, and the coupling of dipole oscillations become stronger[59], and broad LSPRs can be supported. In the solar spectrum, increase in r corresponds to a larger fill factor of ITO compared to vacuum, so the dielectric losses increase. The increase in the α_s, nevertheless, outweighs the increase in ϵ_{IR}, so the FoM, ϵ_{IR}/α_s is essentially larger for the more isolated nanodiscs.

Next, we investigated the role of height of each nanodisc in the absorption spectrum and the OSR parameters. For this purpose, we kept P at 1100 nm, r at 500 nm, t_{SiO_2} at 2000 nm, and swept h. We preferred to keep the nanodiscs densely packed as it imitates our proposed densely packed nanorods better. The absorption spectrum for different values of Fig. 2.1(f) shows that, in the solar spectrum, the height causes an increase in the absorption because the EMWs interact more with ITO before reaching the cavity. In thermal-infrared though, longer nanodiscs caused a decrease in the absorption strength, as the strength

of EMWs reaching to the cavity is now reduced, and reflection due to ITO is increased[49]. The OSR parameters based on our findings is plotted in Fig. 2.1(g), which clearly shows that a thin layer of ITO is beneficial for both ϵ_{IR} and α_s, consequently for the figure of merit as well.

The cavity thickness, t_{SiO_2} is of fundamental importance in an MIM cavity configuration. For our design, we used a Salisbury screen configuration[140], with a thickness of $\lambda_0/4n_{SiO_2}$, where n_{SiO_2} is the real part of the complex refractive index of SiO_2. Due to transmission-line theory[141], and the quarter-wavelength separation of the aluminum ground plane from the ITO layer, the former acts an open circuit at the position of the latter. It is in this way that matching the impedance of ITO layer to free-space is sufficient to achieve perfect absorption. However, in the case of our metasurface OSR, SiO_2 has a strong dispersion in the thermal-infrared due to phonon vibrations around 10 μm and 20 μm. This strong dispersion in n_{SiO_2} means $t_{SiO_2} = \lambda_0/4n_{SiO_2}$ will be a greatly varying value in the thermal-infrared. Moreover, the resultant Reststrahlen bands show an increased reflectivity in the thermal-infrared, which is detrimental to ϵ_{IR}.

To optimize the cavity thickness based on these considerations, we kept P at 1100 nm, h at 50nm, r at 500 nm, and swept t_{SiO_2}. Absorption spectrum in Fig. 2.1(h) clearly shows that the cavity resonances evolve to larger wavelengths as we increased t_{SiO_2}. While smaller cavity thicknesses (750-1250 nm) supported the resonances in the 5 μm- 10 μm range, the thicker cavities (1500-2500 nm) supported LSPRs in 20 μm- 30 μm range. Resonances around 10-15 μm are supported for all of these thicknesses. To find the optimum cavity thickness, the spectral overlap of $A(\lambda, T)$ with the thermal-radiation spectrum, which peaks around 10 μm, is of most importance. The calculation results for the OSR parameters are outlined in Fig. 2.1(i). In Fig. 2.1(i), it can be observed that ϵ_{IR} is almost constant for a wide range of 1.5 μm to 2 μm, while the fringes in α_s is again related to the Fabry-Pérot cavity. As a result, the FoM also has fringes.

Overall, this numerical analysis of Device 2 shows that it can support broad LSPRs in the thermal-infrared and reach a moderate FoM of 4.5 at the cost of requiring a throughput-limiting lithography step. Moreover, Figs. 1d, 1f and 1h all

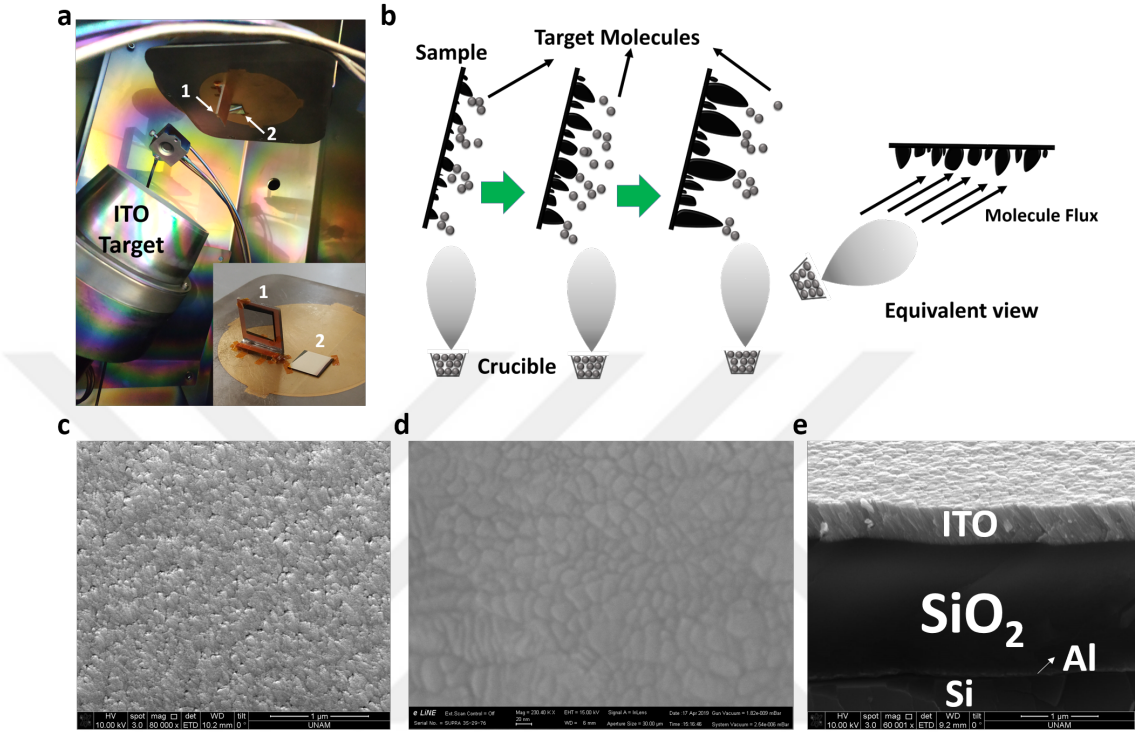

Figure 2.2: Fabrication of the metasurface OSR and the formation of ITO nanoforests. **(a)**: Placement of samples in the sputtering chamber before coating of ITO, **(b)**: Schematic illustration of line-of-sight coating in a sputtering system and the formation of tilted nanowires. **(c)**: Low and **(d)**: High resolution top-view SEM micrographs of one of the fabricated devices. **(e)**: cross-sectional SEM image a sample metasurface OSR.

demonstrate the main limiting factor associated with Device 2 in achieving larger FoM. Device 2 has a highly ordered ITO pattern, so its diffracting/scattering and EMW trapping features are poor. This causes a significant portion of the EMWs to be reflected by SiO_2 at the Reststrahlen bands. These back-reflected EMWs cannot be efficiently retrapped by the ITO layer and, consequently, they leave the device without being harnessed. In these spectral regions, the EMW-ITO interaction is inherently limited and most of the absorption is due to absorption of the EMWs in the SiO_2 layer. This will be analyzed in further detail in the next part of the chapter. As a result, better trapping and harvesting of this reflected radiation while not increasing the solar absorption is of pivotal to achieve an FoM that is competitive to existing OSR solutions.

Fabrication and Characterization of the Metasurface OSR with Disordered and Densely Packed ITO Nanoforests as the Top-Layer

The results of the previous sub-section show that there is significant room for increasing ϵ_{IR} above 0.8, while keeping α_s at a low value. This can be achieved by using a thin layer of disordered and densely packed ITO nanorod forests. For this aim, we fabricated Device 1 with the procedure outlined in the Experimental section. The fabrication step with the most significance is realizing the top-ITO layer. To achieve it, we utilized sputtering system but placed our samples at an oblique-angle to the ITO target. Such a deposition scheme is known as oblique-angle deposition, and it combines the inherent line-of-sight coating of PVD systems with shadowing to achieve quasi-3D nano-sized columnar fills with an intrinsic tilt and porosity. Fig. 2.2(a) shows placement of two samples in the sputtering system. While sample 1 is placed at an oblique angle to the ITO target, sample 2 is placed in an ordinary manner for planar deposition, which is used for comparison purposes and for extracting the dielectric permittivity of ITO. The inset of Fig. 2.2(a) shows the placement of samples in the sample holder plate, and the special FR-4 apparatus that we designed to place the oblique-angled sample.

In the oblique-angle deposition, a standard planar thin-film deposition, as in Sample 2, is transformed into preferential deposition of random nucleation sites, formed during the initial stages of deposition. Continued deposition results in the deposition on these nucleation sites, while no deposition takes place in the shadowed regions. Consequently, disordered and densely packed nanocolumns emerges and they are intrinsically tilted towards the source. Such a process flow, along with an equivalent picture is illustrated schematically in Fig. 2.2(b). The formation of such nanorod forests is verified by using planar and cross-sectional scanning electron microscopy (SEM) micrographs, as presented in Figs. 2.2(c-d), and 2.2(e), respectively. The device in these figures have a 400 nm coating of ITO (which is larger than that of ITO in the devices to be mentioned later in this chapter) in order to better demonstrate the details of the nanoforests, as well as

the tilting of nanowires toward the source.

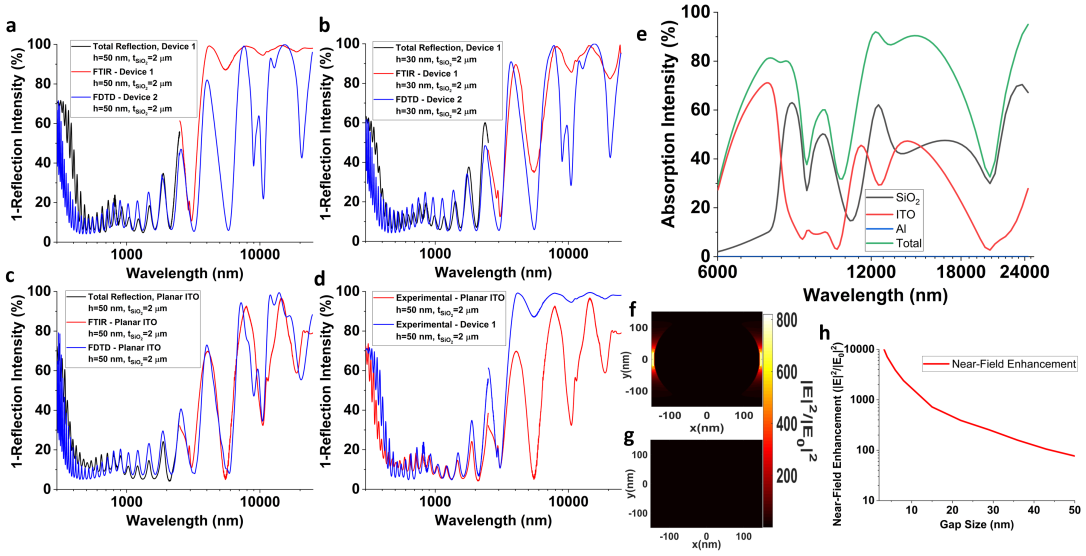

Figure 2.3: Optical Characterization of the fabricated devices with disordered ITO nanorods, comparisons to numerical simulations of Device 2 and experimental result of a planar design, physical explanations on ϵ_{IR} enhancement in the proposed Device. **(a)**: Experimental absorption result for Device 1 with h=50 nm and t_{SiO_2}= 2μm compared to the numerical simulations of Device 2 with the same h and t_{SiO_2}, **(b)**: Experimental absorption result for Device 1 with h=30 nm and t_{SiO_2}= 2μm compared to the numerical simulation Device 2 with the same h and t_{SiO_2}. **(c)**: Experimental absorption result for a planar device with h=50 nm and t_{SiO_2}= 2μm compared to numerical simulations for same device, **(d)**: Comparison of the absorption spectra of the planar device and Device 1 with h=50 nm and t_{SiO_2}= 2μm. **(e)**: Contribution of each layer to the absorption in thermal-infrared. **(f)**: Localization and enhancement of electric-field between nanodiscs of P=300 nm, r=142.5 nm. **(g)**: $|E|^2/|E_0|^2$ value recorded at a planar ITO layer. **(h)**: Near-field enhancement, $|E|^2/|E_0|^2$ values as a function of gap size between nanodiscs. In **(f)**, **(g)** and **(h)**, the $|E|^2/|E_0|^2$ values are recorded at 15 μm, and at the midgap position.

In finding the reflection spectrum of the fabricated devices, measurements in

the UV/VIS/NIR ranges are carried out in a total reflection spectrophotometer. In the thermal-infrared, Fourier Transform Infrared Spectroscopy (FTIR) technique is utilized and the details for optical characterization are given in the Experimental section. The absorption spectrum for the fabricated devices are then found by $A = 1 - R$.

In our initial set of fabrication and experiments, we fabricated Device 1 with the thickness of the ITO layer as 50 nm and the SiO_2 thickness as 2μm. The experimental absorption spectrum of this device, in comparison to the FDTD simulations of Device 2 using periodic discs of 50 nm thickness presented in Fig. 2.3(a). In the FDTD simulations, the periodicity of the discs is set as 1100 nm and its diameter is 1 μm. The result in Fig. 2.3(a) demonstrates a remarkable enhancement of light-matter interaction in Device 1 compared to Device 2, and consequently ultrabroadband-absorption in the thermal-infrared, resulting in an outstanding ϵ_{IR} of 0.962.

From the space missions perspective, it is equally important to keep α_s within acceptable limits while increasing ϵ_{IR}. It is critical to mention that our designed scaffold with high diffraction/scattering and light trapping also means solar radiation interacts more with the low-loss dielectric ITO, which may result in higher α_s. To alleviate this, a thin ITO layer is needed to simultaneously provide a large ϵ_{IR}, while not emphasizing losses in the solar spectrum. In Fig. 2.3(a), it is seen that Devices 1 and 2 produce similar absorption profiles in the solar spectrum below the bandgap of ITO, where the losses due to ITO is not significant. However, below 400 nm, interband transitions of ITO become a prominent loss mechanism and strong light-matter interactions in the Device 1 produces more absorption than Device 2. Nevertheless, using only 50 nm ITO thickness allowed us to keep α_s at 0.168. The FoM reached a record-high value of 5.73. Another important observation from Fig. 2.3(a) is that the spectral positions of the peaks and dips in the absorption spectrum have great agreement between the FDTD simulations of Device 2 and the experimental result of Device 1. This is because, these peaks and dips are determined by the phase accumulation during the round-trip in the SiO_2 cavity, and the added phases due to reflections at ITO-SiO_2 and SiO_2-Al boundaries.

In an attempt to further improve the FoM, it is more important to decrease α_s rather than increasing ϵ_{IR}, as the former is already very close to unity in Device 1 with h=50 nm and t_{SiO_2}= 2μm. Moreover, the numerical results for Device 2 show that thicker layers of ITO accentuate α_s more than ϵ_{IR}, so FoM is deteriorated. Therefore, in our second set of experiment thicker layers of ITO are not investigated, and we reduced the thickness of the ITO layer to 30 nm. The experimental absorption spectrum of this device is shown in Fig. 2.3(b), along with the spectrum for Device 2 with , while the other geometrical parameters are the same as before. In the solar spectrum, the intention of decreasing α_s is accomplished, as it decreased to 0.161, due to the smaller thickness of ITO. In the thermal-infrared, however, Device 1 with h=30 nm has worse absorption when compared to h=50 nm case, due to the poorer light-trapping capability of the scaffold. Similar to the h=50 nm case, Device 1 still outperforms Device 2 in the h=30 nm case, as ϵ_{IR} reached 0.884 and the FoM is 5.49.

We also compared Device 1 with another lithography-free design that utilizes a planar ITO layer, to further represent the power of the designed ITO nanoforests as a light-trapping scaffold. The experimental result for the planar device with h=50 nm and t_{SiO_2}= 2 μm is first shown in Fig. 2.3(c) as well as the FDTD simulations for this device. In Fig. 2.3(d), we compare the experimental results for Device 1 and the planar design with the h=50 nm and t_{SiO_2}= 2 μm parameters. While the planar design achieves an α_s of 0.151, its ϵ_{IR} is only 0.697, so the FoM is limited to 4.61. The planar design gives the worst ϵ_{IR} because it lacks both the light-trapping capability of Device 1 and the LSPRs supported in Devices 1 and 2. However, it does not suffer from diffraction/scattering and the resultant excited guided-modes of the structure[142]. Overall, the ITO nanoforest design still outweighs the planar design.

Our proposed device is experimentally confirmed to provide an excellent scaffold for ultra-broadband thermal-infrared absorption and provides far superior ϵ_{IR} compared to Device 2. There are five underlying physical reasons for this. First and foremost, the strong dispersion and phonon reflection of SiO_2 at Reststrahlen bands was the primary reason for limiting ϵ_{IR} of Device 2 under 0.8. In those regions, incident radiation is back-reflected, and a significantly smaller

portion of the radiation is trapped and harvested in the device. To make matters worse, the back-reflected EMWs cannot be efficiently retrapped in Device 2 by the periodic ITO nanodiscs, due to their poor diffraction/scattering and trapping features. Therefore, these back-reflected EMWs are not harnessed in Device 2, and light-ITO interaction is limited in these areas. This is analyzed in more detail and verified numerically by placing three three-dimensional (3D) monitors on the Al, SiO_2, and ITO layers, and calculating the contribution of each layer to absorption in the thermal-infrared. We used the formula in Eq. 2.3,

$$\frac{dP_{loss}}{dV} = \frac{1}{2} w \epsilon^{''}(w) |E|^2 \tag{2.3}$$

where P_{loss} is the absorbed power due to conduction losses and dielectric hysteresis, V is the volume, w is the angular frequency, $\epsilon^{''}(w)$ is the imaginary part of the complex permittivity and $|E|^2$ is the modulus of the complex electric-field inside each layer[93]. dP_{loss}/dV is integrated over each layer and normalized to the incident power to obtain absorption of each layer.

The absorption spectrum in Fig. 2.3(e) clearly shows that in the phonon reflection bands (around 10 and 20 μm) of SiO_2 absorption of the transmitted light in the cavity is the main driver behind the absorption spectrum. However, this strong reflection is mitigated in Device 1, which is clearly visible upon comparing the absorption spectra of Device 1 and Device 2 around 10 μm and 20 μm in Fig. 2.3(a). This is a direct result of the rough and highly diffracting/scattering top-layer ITO scaffold. While the thermal-radiation is reflected in Device 2 at Reststrahlen bands, in Device 1, the scaffold traps this thermal-radiation (or, in other words, the residing time of thermal-radiation in the structure is improved) and it is absorbed by the hybrid system of broad plasmonic resonances supported by ITO and phonon bands of SiO_2. The fact that thinner ITO layers suffer more from reflection losses (by comparing Figs. 3a and 3b) also supports the argument that increasing the residing time of EMWs in Device 1 and coupling them to the ITO/SiO_2 hybrid is the main driver in enhanced absorption.

Secondly, ITO offers a plasmonic response with relatively high losses[143], so the excited LSPRs inherently have a large linewidth. Thirdly, the randomness in the morphology of the nanorods, as confirmed in the SEM images in Figs. 2d

and 2e, results in multiple adjacent LSPRs of different strength, spectral position, and linewidth. Since our fabrication route generates random geometries, the superposition of the excited LSRPS then contribute to a flat, perfect absorption over an ultra-broad bandwidth. Fourthly, the gap distances between the tilted nanorods is found to be very small, and not uniform. It is shown in the literature that extremely small gaps between plasmonic nanostructures result in the extreme enhancement and localization of optical fields[144]. We show the near-field enhancement of optical fields between the ITO nanodiscs, due to the dipolar LSPRs in Fig. 2.3(f), as an exemplary case from Device 2. The optical field inside the ITO layer of a planar device is also calculated, and the result is shown in Fig. 2.3(g). Comparison of Figs. 3f. and 3g. demonstrate that the plasmonic resonance, and the corresponding electromagnetic hotspots between the nanodiscs does not exist in the planar case. This is the reason why the planar design had the poorest ϵ_{IR}. In Fig. 2.3(h), we indicate that further decreasing the gap distance between the nanodiscs result in higher enhancement of optical fields. This extreme localization results in larger optical losses, as a result of Eq. 2.3. Thus, the formation of deep sub-wavelength gaps between the nanowires, as demonstrated in Figs. 2d and 2e, triggers the existence of intense local fields and these hotspots lead to strong light absorption in the thermal infrared. Moreover, when the distance between the nanostructures become very small, the position of plasmon resonances is determined by the gap size, rather than the individual dimensions of the nanostructures. The randomness in the porosity of the deposited film, as shown in Fig. 2.2(c), is then a contributor to the perfect absorption.

Lastly, the random nanorods in Device 1 diffract light in more directions, compared to the periodic discs of Device 2. Therefore, Device 1 may be aiding the coupling of a larger portion of incident radiation to the surface-plasmon polaritons (SPPs)[78] in the SiO_2-Al interface.

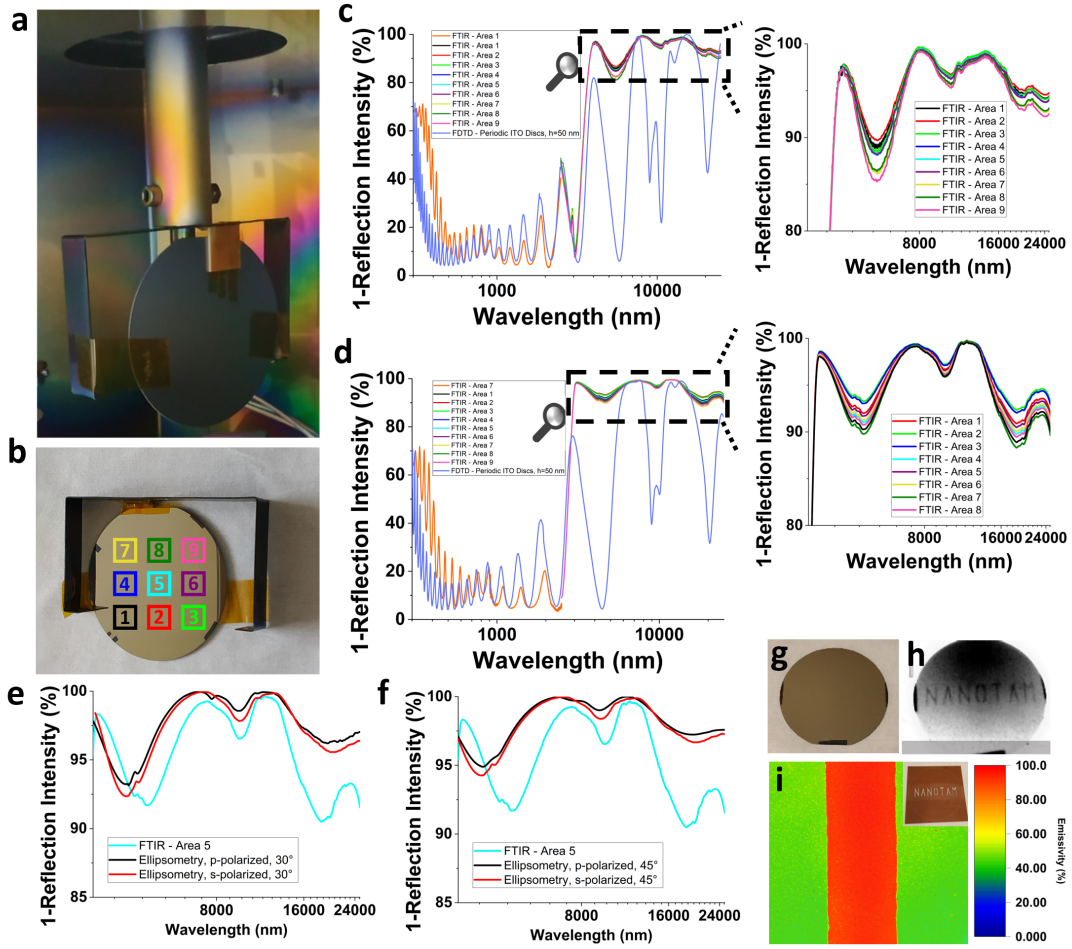

Figure 2.4: Large-Scale fabrication and optical characterization of the proposed Device **(a)**: Positioning of the wafer in the sample holder as seen from the back-view. **(b)**: Measurement areas in the fabricated wafers. Experimental absorption result for Device 1 with h=50 nm and **(c)**: t_{SiO_2}= 2μm, **(d)**: t_{SiO_2}= 1.55μm, when fabricated on a wafer. Absorption spectrum under obliquely-incident radiation at an incidence angle of **(e)**: 30°, and **(g)**: 45°. Device 1 as seen with **(g)**: naked eye, **(h)**: thermal camera. **(i)**: Thermal microscope image of Device 1. The ellipsometry measurements are taken from Area 5.

Large-scale Fabrication of the proposed device and Optical Characterization

Oblique-angle deposition not only offers a substantial enhancement to the OSR performance, it also enables a facile route for large-scale fabrication, which is of paramount importance to establish a competitive OSR technology to the planar conventional devices. As a proof-of-concept, Device 1 with h=50 nm and t_{SiO_2}= 2μm is fabricated on a 4-inch silicon wafer. The wafer is placed in the sputtering chamber at an angle to the source, similar to Fig. 2.2(a). To do that, the plate is removed, and the wafer is directly fixed in the sample holder as shown in Fig. 2.4(a), which shows the attachment of wafer from the back side. The same apparatus used for small area samples is also used to put the wafer at an oblique angle and two strips are adhered to the sides of wafer for additional support. The wafer is characterized from 9 different areas, which are shown in Fig. 2.4(b) to indicate the adaptation of oblique-angle deposition technique to large-scale fabrication, and also examine the uniformity of the coating. The experimental results are shown in Fig. 2.4(c). The solar absorption is measured only from Area 5 and α_s is calculated as 0.167, which is almost identical to the small-area fabrication. On the other hand, spectral response in thermal-infrared is measured from all 9 areas. To further discern the variations in the absorption spectra between different areas, we zoomed into 3 μm to 25 μ region. It is seen that the regions further away from the source has slightly lower absorption, which is attributed to the minor non-uniformity in ITO thickness within the wafer. Nevertheless, the smallest ϵ_{IR} is found to be 0.957, while its highest value reached 0.97, so the variations within the wafer is not significant.

Experimental results up to now have demonstrated the optimized optical performance of the metasurface OSRs. Nevertheless, decreasing the thickness of SiO_2 is still desirable to decrease the launch and assembly costs and the weight of the OSRs, when they are used to coat a spacecraft. The numerical results of Device 2 has shown that several different cavity thicknesses can result in almost equal FoM. It can be seen in Fig. 2.1(i) that a cavity thickness between 1.5 μm and 1.6 μm gives the peak FoM, while also being the most tolerant area to thickness

inaccuracies. Device 1 with h=50 nm and t_{SiO_2}= 1.55μm is fabricated on a 4-inch wafer and is characterized in the same way as before. Experimental result for this device and numerical result for Device 2 with the same h and t_{SiO_2} are shown in Fig. 2.4(d). The experimental results show similar characteristics to Fig. 2.4(c) and the physical reasoning outlined until now apply to this sample. The maximum ϵ_{IR} is calculated as 0.968, while its minimum value is 0.952. α_s is found to be 0.169. Therefore, almost identical performance to ITOD50CAV2000 device is achieved with a smaller thickness of SiO_2.

Another important consideration for an OSR in space missions is its spectral response under obliquely-incident radiation. To scrutinize this, spectral response of Device 1 with h=50 nm and t_{SiO_2}= 1.55μm under obliquely-incident radiation is measured experimentally in the thermal-infrared, from 3 μm to 25 μm, by utilizing ellipsometry method. The results at 30 and 45 degrees incidence angles are shown in Figs. 2.4(e) and 2.4(f), respectively; for both p- and s-polarized incident radiations. The blue-shifting of the spectral response as well as increased absorption behavior are observed in these results.

In this chapter up to this point, we have demonstrated that the outstanding performance of our proposed device fulfills the key functionality of an OSR, that is, a very high ϵ_{IR}, a small α_s, large-scale compatibility and uniformity. Our proposed device has a thickness around 2 μm, which is at least two orders of magnitude smaller than that of the conventional OSRs. Nevertheless, application of these devices to the radiative cooling of spacecraft in real-time necessitates further studies in scrutinizing the heat transfer and finding the cooling rates. In addition to these, the ongoing studies will focus on application these ideas to flexible substrates, and tests involving the mechanical, thermal, UV, and radiation resistance of the proposed devices. The perfect absorption in the thermal-infrared range and the experimentally obtained ϵ_{IR} of 0.968 are also very promising in the areas of thermal-imaging cameras with labeled-security. As a proof-of-concept, a mask with drilled holes to create the labeling word "NANOTAM" is placed on the wafer before sputtering. After fabricating Device 1 with h=50 nm and t_{SiO_2}= 1.55μm, the wafer is observed with a thermal camera. Lithography is

not preferred to create the label in order not to sacrifice from large-scale compatibility. The view of the wafer with naked eye is given in Fig. 2.4(g), and the "NANOTAM" label is barely recognizable. However, when this wafer is inspected under a thermal camera, the large emissivity difference between the ITO coated vs. non-coated areas make the label clearly discernible, as shown in Fig. 2.4(h). In Fig. 2.4(i), we show a thermal microscope micrograph from one of the areas. The sharp contrast between the ITO coated areas (appear red due to very high thermal-emissivity) vs. the non-coated areas is clearly distinguishable. It is also important to note from Fig. 2.4(i) that the areas with only SiO_2 coating still have an ϵ_{IR} of 0.5. This further supports our argument that the perfect absorption in the proposed devices are a result of the hybrid system of ITO and SiO_2.

2.3 Experimental Section

2.3.1 Fabrication of the metasurface OSR

For the fabrication of the small-area samples, first, a typical commercial square-shaped Silicon substrate with 225 mm^2 area has been cleaned with Acetone, Isopropanol (IPA), and deionized water, and then has been dried with N2 flow, to be used as a substrate. The surface was further treated using oxygen plasma for 20 minutes before starting the deposition of thin films. Same procedure is followed for the 4-inch wafers. Firstly, 125 nm thick aluminum back-reflector is coated by using an electron-beam evaporator system (Leybold Univex 350) at a chamber pressure of 3e-6 to 5e-6 mbar and at a rate of 2 Å/s. Next, a SiO_2 layer with the thicknesses mentioned in the main text are coated by using a Plasma-Enhanced Chemical Vapor Deposition (PECVD) system (SAMCO). This process is carried out with SiH_4 and N_2O flow rates of 300 sccm at a temperature of 350 °C. Finally, an ITO layer is coated in an RF-magnetron sputtering system (Leybold Univex 350) at a processing pressure of 2.2e-3 mbar, RF power of 125 Watts, and a rate of 1.3 Å/s. The flow rate of high purity (99.999%) sputtering Argon (Ar) gas, free of oxygen, was 7 sccm during the process. No oxygen was

added during the deposition. The sample holder is not rotated during the process.

2.3.2 Optical Characterization

To measure the thermal emissivity, ϵ_{IR}, of the samples with disordered ITO nanoforests and planar ITO thin film structures, reflectance in the thermal-infrared spectrum was measured over the range of 2.5 to 25 μm using an FTIR microscope with a numerical aperture of 0.4 (Bruker- Vertex 70v, Hyperion microscope). The instrument employs a mid-infrared source, KBr beamsplitter and nitrogen-cooled Mercury Cadmium Telluride (MCT-D313) detector. A 125 nm aluminum coated SiO2/Si substrate was used as reference. Solar absorptance of all the samples are obtained by measuring the UV/VIS/NIR reflectance over the range from 300 nm to 2.5 μm. In these measurements, a commercial total reflection spectrophotometer (Agilent Cary 5000), utilizing a diffuse reflectance accessory (DRA) of a diameter of 110mm is used. White polytetrafloroetilen (PTFE) is used as a reference. Oblique-angle measurements in the thermal-infrared is carried out by using J.A. Woollam Co. Inc. IR-VASE Mark II ellipsometer. The emissivity difference between ITO coated vs. non-coated areas are investigated by using a commercial thermal camera (Seek Thermal). The microscopy images for the same purpose is taken by nitrogen-cooled InfraScope^{TM} MWIR Temperature Mapping Microscope from Quantum Focus Instruments (QFI) Corp.

2.3.3 Numerical Simulations

In the FDTD simulations, we illuminated the unit-cell with a broadband plane-wave at normal incidence whose electric-field is polarized in the x-direction. In the x and y directions of the simulation region, we used periodic boundary conditions, while in the z-direction perfectly matched layers (PML) are adopted and they are placed 4 wavelengths away from the structure. We used a single monitor that was at an adequate distance away from the structure to collect the reflected EMWs and calculate the reflected (R) power, that is normalized to the incident power.

Due to the fact that the bottom Al thickness was chosen to be much larger than the skin-depth of EMWs at the spectral regions of interest, the transmitted power (T) was considered to be negligible. After verifying this in the simulations, we calculated the spectral absorption by using $A = 1 - R$. To be able to increase the stability of the simulations and spectral resolution of the absorption spectrum, all of the FDTD simulations were divided into three regions: wavelength from 300nm to 2.5μm, 2.5 μm to 15 μm and 15 μm to 30 μm.

Chapter 3

Colorimetric and Near-Absolute Polarization Insensitive Refractive-Index Sensing in All-Dielectric Guided-Mode Resonance based Metasurface

This chapter is on part reprinted with permission from: **Deniz Umut Yildirim**, Amir Ghobadi, Mahmut Can Soydan, Murat Gokbayrak, Ahmet Toprak, Bayram Butun, and Ekmel Ozbay, The Journal of Physical Chemistry C, 2019 ,123 (31), 19125-19134, DOI: 10.1021/acs.jpcc.9b04748.

3.1 Introduction

In this study, we propose a novel design that utilizes a 2-dimensional sub-wavelength grating-waveguide structure to excite its guided-mode resonances

(GMRs). We employ the finite-difference-time-domain (FDTD) method to numerically show that the coupling of incident light to the GMRs yields perfect reflection of light (98.7%) with 0.58 nm of full-width at half-maximum (FWHM) at 602.5 nm, under p-polarized incident light. In the literature, the refractive index sensing performance is frequently evaluated by changing the refractive index of the entire environment[145, 146, 147, 148]. We, however, investigated a scenario that is closer to biosensing, by considering the deposition conformal dielectric layers (an example can be NH_2 (Amine) groups) coated over the device. The highest sensitivity reached as high as 110 nm/refractive index unit (RIU), for the biolayer thickness of 30 nm, yielding a very high Figure of Merit (FoM) of 190. Moreover, the proposed device preserves perfect reflection $> 98\%$ at all source polarization angles as well as the spectral position of the resonance. We then transferred these numerical findings to the fabricated devices. Highly-sensitive sensing of adsorbed layers and change of surrounding refractive index is experimentally demonstrated by comparing a bare device, and two devices with 30 nm Alumina (Al_2O_3) and Zinc Oxide (ZnO) layers, coated by Atomic Layer Deposition (ALD). These proof-of-concept devices offered an high experimental sensitivity of 235.2 nm/RIU, with a resonance linewidth of 19 nm. Examination of samples with the naked eye showed that each sample with a different coating has a distinct color, owing to the high sensitivity and narrow linewidth. The samples also preserved the reflected color upon 90 degrees of rotation, so insensitivity to incident-light polarization is also verified. Excellent agreement is obtained between the numerical and experimental results in terms of the spectral position of the resonances and sensitivity. The spectral tunability of the resonances is shown numerically, by changing the key geometrical parameters of the device. We first elucidate the resonance mechanism in an optimized grating-substrate structure. We then demonstrate the polarization insensitivity and sensing performance of the device and scrutinize the effect of geometrical parameters on the figure of merit of the device. Finally, we present the experimental results for the fabricated devices.

3.2 Results and Discussion

3.2.1 Exciting guided-mode resonances of a grating-waveguide structure with polarization-insensitivity

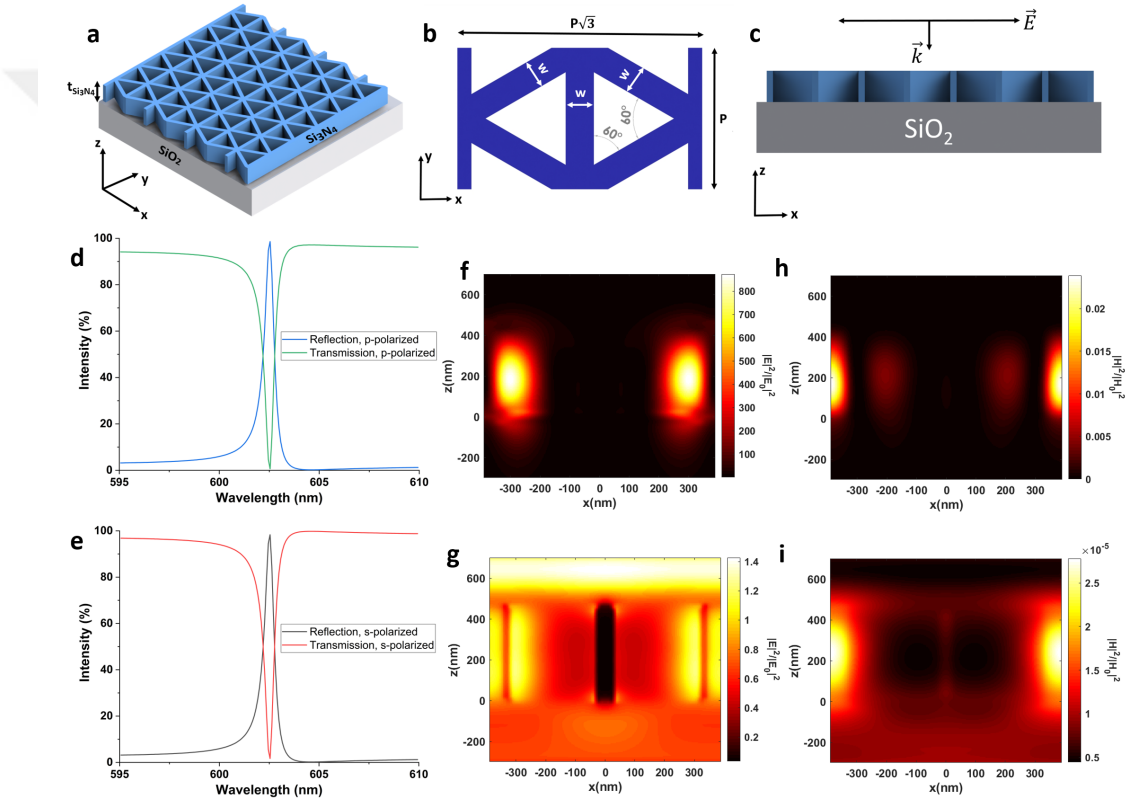

Figure 3.1: The proposed design and its unit-cell **(a)** Device I to excite GMRs. **(b)** Unit-cell of Device I, detailing the 2D grating, as seen from the top-view. **(c)** Dielectric layers, as seen from the side-view, and illumination by p-polarized plane wave. Transmission and Reflection spectra for Device I **(d)** under p-polarized; **(e)** under s-polarized incident plane wave. $|E|^2/|E_0|^2$ at XZ plane during **(f)**: on-resonance at 602.5 nm; **(g)**: off-resonance at 750 nm; $|H|^2$ at XZ plane during **(h)**: on-resonance, **(i)**: off-resonance. $|E|^2$ and $|H|^2$ are the modulus of electric and magnetic field inside Device I, $|E_0|^2$ and $|H_0|^2$ denote that of incident light. GWS extends from z=0 to z=460 nm.

Our proposed device in Fig. 3.1(a) is designed to excite the guided-modes of a unique 2-dimensional, sub-wavelength, periodically modulated, high-refractive index Silicon-Nitride (Si_3N_4) waveguide core. Due to the introduced periodicity in this structure, it additionally exhibits properties of a grating, and essentially a phase-matching coupler element[86, 88]. This grating-waveguide structure (GWS) is supported by Quartz (SiO_2) substrate. We call this design Device I. The near-absolute polarization insensitive hexagonal unit-cell is based on our group's previous studies on ultra-narrowband perfect visible light absorption in monolayer graphene[26], and wideband plasmonic light absorbers[149]. Fig. 3.1(b) illustrates the details of our novel 2D sub-wavelength grating from the top-view. Two dielectric layers and the excitation conditions are shown from the side-view in Fig. 3.1(c). The critical design parameters in determining the spectral position of GMRs is the thickness of the grating region, $t_{Si_3N_4}$; the periodicity, P, of the unit cell in y-direction, the width of each grating stripe, w.

To investigate the spectral response of Device I, we utilize finite-difference-time-domain simulations. Details of the simulation setup are outlined in the Methods Section.

Firstly, we set the geometrical design parameters $t_{Si_3N_4}$, P and w to their optimum values of 460 nm, 450 nm, and 60 nm, respectively. We then looked at the amount of power that is reflected or transmitted from Device I to gain insight about the resonance excitation. The simulation result in Fig. 3.1(d) shows a sharp guided-mode resonance manifesting itself as a peak in reflection (98.7%) and a dip in transmission at 602.5 nm. The absorption due to the dispersion of dielectrics is negligible but not zero, which is why reflection cannot fully reach 100%. The same simulation is also performed by changing incident light polarization from p to s-polarization (E-field is now polarized in y-direction) and the result is shown in Fig. 3.1(e). Comparing these figures, the most important observation is that the spectral position of the resonance and the reflection intensity at resonance are almost identical, owing to the unit-cell. The physics governing the excitation the GMRs is explained in detail in the Methods section.

To discern the resonance-behavior, we plotted the electric and magnetic-field

(E-field and H-field) profiles at two different wavelengths, when Device I is off-resonant or on-resonant. We demonstrate a comparison of the fields for these two situations in Figs. 3.1(f-i). These figures clearly indicate a strong field enhancement and the localization of both fields inside the GWS region. Both fields are enhanced close to three orders of magnitude with respect to the incident light. It is the strong field localization and the large optical energy stored in the waveguide core that is responsible for the very small linewidth of the GMR. The electric field and magnetic field profiles in Figs. 3.1(f,h), respectively, implies that the fundamental mode of the slab waveguide is excited. This is entirely expected because of the relatively small thickness of the waveguide core region with respect to the wavelength, $t_{Si_3N_4}/\lambda$, as the excitation of higher order modes of a waveguide requires larger core thickness[93, 150].

Another intriguing feature of GMRs is their Fano lineshape. It emerges because of the interaction between the sharp resonance channel and the broad radiation continuum[151]. The sub-wavelength nature of the grating results in only zeroth order diffracted wave to propagate, while all other diffracted orders are evanescent. Therefore, the incident-wave is coupled evanescently to the guided-mode.

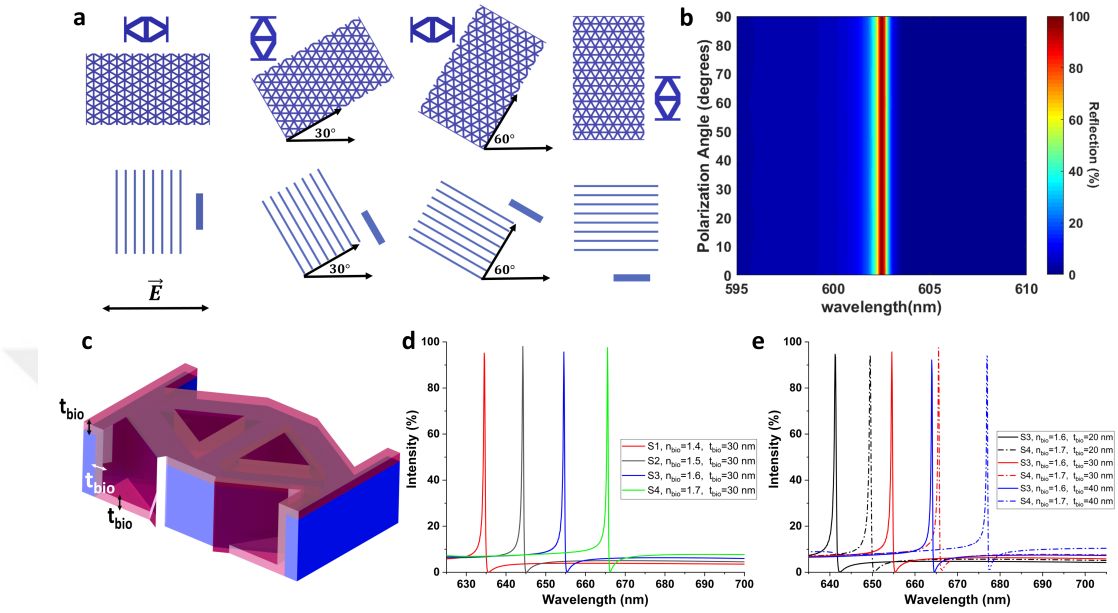

Figure 3.2: Achieving near-absolute polarization insensitive refractive index sensing in Device I with the 2D-grating **(a)** Comparison of the unit-cells of Device I and the design incorporating 1D grating under different rotations. **(b)** Reflection map of Device I for the polarization angles spanning from 0° (p, TM-polarization) to 90° (s, TE-polarization). **(c)** Device II with the adsorbed biolayer. Spectral shift of the guided-mode resonance depending on the **(d)**: refractive index, n_{bio}, **(e)**: thickness, t_{bio}, of the biolayer.

We now concentrate on the polarization-insensitivity of Device I. We explained the reasoning behind using the hexagonal 2D unit-cell to achieve polarization insensitivity explicitly in our early works [26]. Briefly, the idea behind achieving polarization insensitivity is to come up with a unit-cell whose interaction with the incoming E-field changes as little as possible for all polarization angles. This is equivalent to stating that E-field with a fixed polarization angle has to "observe" the same unit-cell upon rotating the latter arbitrarily. By doing so, form birefringence, and the different excitation conditions between the TE and TM Bloch modes, defined by the periodicity of the structure[93] are minimized, which are the main reasons why 1D gratings are polarization-sensitive.

To compare the unit-cell Device I with the devices using 1D grating, we kept the polarization angle of the incident wave at ϕ= 0 degrees, and rotated both unit-cells for 0, 30, 60, and 90 degrees. The result of this comparison is shown in Fig. 3.2(a). From Fig. 3.2(a), it can be seen that our hexagonal unit-cell has 60° of rotational symmetry, while the 1D grating has different unit-cells for all polarization angles. The hexagonal unit-cell is in different orientations for the 0° (60°) and 30° (90°) cases, but the interaction of E-field with the unit-cells are nearly identical (see Supporting Information of ref.[26] for a more detailed discussion). We examined the polarization insensitivity of Device I in more detail by sweeping the polarization angle of the source from 0° to 90°. The result in Fig. 3.2(b) clearly demonstrates that Device I preserves almost constant reflection at a nearly fixed spectral position.

3.2.2 Refractive-index sensing with the proposed Device

Our discussion of the guided-mode excitation, and its theoretical treatment in the Methods section also points out the fact that the propagation constant of the guided-mode, β, and therefore n_{eff} strongly depend on the refractive indexes of the GWS and the superstrate regions. To analyze this, we consider a scenario where an aqueous or gaseous solution containing target analytes is delivered over Device I with the help of a microfluidic channel. The accumulation of the target analytes on the surface will change the refractive indexes n_{super} and n_w, where the latter can be thought as a weighted average of $n_{Si_3N_4}$and the background refractive index. Since β is a constant under fixed grating periodicity, the resonance wavelength is shifted, from Eq.S5. This wavelength shift can be directly related to the addition of the biolayers and Device I can be calibrated differently for different relevant molecules. The small changes in the properties of the dielectric medium can be read if the sensor has large sensitivity values.

The shift of the resonance wavelength is usually quantified in the literature by altering the entire refractive index of the simulation region[145, 152, 153, 154, 155, 146, 147, 148]. The possible down-side of this method, however, is that

the target molecules are typically confined to a very thin region that may be smaller than the decay length of the guided-mode in the superstrate. In such a case, the optical fields are not decayed to negligible values in the air region above the biolayer. Therefore, if the biolayer refractive index is assigned to the entire superstrate region, including the air, these optical fields now interact with n_{bio}, instead of air, and shift the GMRs considerably. As a result, the interaction of the optical fields with the superstrate is overestimated compared to its actual (air on top a thin biolayer) case. This causes the shift of GMRs to be significantly larger than their true values. Consequently,the accumulation of target analytes can be analyzed better by regarding them as a thin deposition layer on the GWS, and treating sensitivity as a function of biolayer thickness. Only if the biolayer thickness is much thicker than the decay length of the guided-mode, can n_{bio} be safely assigned to entire simulation region.

To measure the sensitivity of Device I, we modeled the biolayer as a dielectric film, deposited as a conformal layer over Device 1. Device I with the attached biolayer is called Device II, which is shown in Fig. 3.2(c).

To evaluate sensing, we initially fixed the biolayer thickness, t_{bio}, as 30 nm, while varying its refractive index, n_{bio}. The shift of the GMR peak in Device II is presented in Fig. 3.2(d). By taking the largest spectral shift of the GMR, $\Delta\lambda$, the maximum sensitivity[145, 152, 153, 154, 155, 146, 147, 148] (S^{max}) of Device II is found as $S_{\max} = \Delta\lambda/\Delta n = (665.53nm - 654.55)/(1.7 - 1.6) = 110nm/RIU$. Based on Fig. 3.2(d), S^{max} is obtained between S4 and S3 cases, i.e. between n_{bio}=1.6 and n_{bio}=1.7. For our proposed device, it is observed that as the biolayer refractive index gets larger, it becomes more sensitive. This is expected because of the following reason. Under fixed fill-factor of GWS with Si_3N_4, the biolayer with a larger refractive index has a higher influence on n_w, n_{super}, and consequently n_{eff}, even if it has a constant thickness.

To examine how changing biolayer thickness, t_{bio}, affects the performance of Device II, we considered S3 and S4 cases, and the results are shown in Fig. 3.2(e). Two important observations can be made from Fig. 3.2(e). First, as t_{bio} is increased, the GMRs continue to shift for constant n_{bio}, due to the increased

interaction of optical fields with the biolayer. At the same time, as the biolayer gets thicker, the GMRs shift more for the same Δn value of 0.1. This is because a thicker biolayer has a greater filling factor and again a higher influence on n_w, so Device II becomes more sensitive and can have larger $S_{\max}$ values, when a thicker biolayer are attached on it.

With the calculated sensitivity (S) value of 110 nm/RIU and the FWHM of 0.58 nm, the Figure of Merit of our sensor reached as high as $FoM = S/FWHM = 190$. We also observed that the resonances get narrower as the biolayer refractive index is increased. This is also expected by the coupled-mode theory[86], which found that the linewidth is proportional to the difference between the dielectric permittivities of grating material and the surrounding medium, $\Delta\epsilon$.

We close this subsection by pointing out that the attachment of biological analytes may also change the geometrical dimensions that may shift the resonance frequency. Therefore, biosensing is realizable by Device I in addition to refractive index sensing as outlined up to now. To point out an important design consideration, however, in refractive-index sensing the overlap of the electromagnetic mode outside the guiding layer should be maximized to resolve all of the changes in the superstrate. Conversely, in biosensing, this overlap should only cover the ultra-thin layer that the analytes attache to[156, 67]. As another possible application, the biolayer thickness dependent shift of the resonance wavelength, under constant n_{bio}, implies that this shift can be measured as a function of time to quantify the binding kinetics. These applications are an ongoing study at the present time.

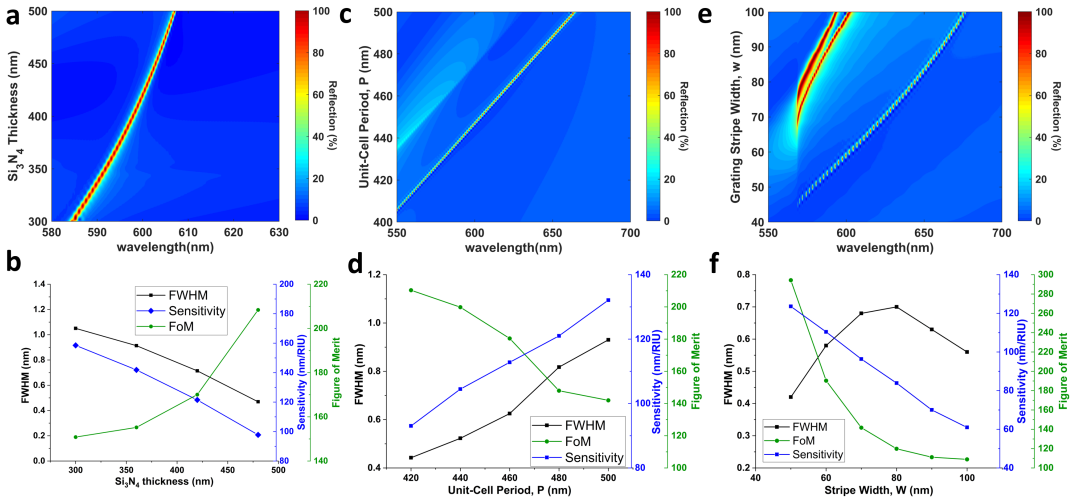

Figure 3.3: Dependence of the reflection spectrum and the refractive-index sensing properties of Device I on the structural parameters. Reflection spectrum of Device I under varying **(a)**: Grating thickness, $t_{Si_3N_4}$,**(c)**: unit-cell periodicity in the y-direction, P, **(e)**: Width of each stripe, w. When changing one parameter, we kept the other parameters at their optimum value. FWHM, sensitivity and FoM of Device II when **(b)**: $t_{Si_3N_4}$, **(d)**: P, and **(f)**: w are changed. FWHM is measured for Device I without the biolayer attachment, while sensitivity is measured for Device II by comparing the S3 and S4 cases, with t_{bio}=30 nm. In the unit-cell periodicity sweeps, width of grating is kept as $w = \frac{2P}{15}$. All results are taken with p-polarized incident wave.

Technological tolerances of the proposed device and effect of geometrical parameters on GMR properties and sensing performance

The results and discussions up to now demonstrate that GMRs can be excited when the phase-matching condition is satisfied, i.e. one of the evanescent diffracted order can be coupled to one of the guided waveguide modes. Although the waveguiding effects on the Bloch modes[88] of the periodically patterned waveguides are complicated, we can still have a solid understanding on how the

spectral position of GMRs and the sensing properties of Device I and Device II depend on the structural parameters $t_{Si_3N_4}$, P and w.

To start with the spectral position of GMRs, Eqns. S5, S6, S7 show that it strongly depends on the effective refractive index, n_{eff}, of the guided-mode if we regard GWS as an asymmetric dielectric slab waveguide. This is done by considering the GWS as a medium with an effective dielectric permittivity[93, 157]. For the linewidth of the resonance, one can resort to either one of coupled-mode theory, a multiple-interference model based on geometrical ray picture or quality-factor of a standard waveguide[86, 87]. For our analysis, we will employ the findings of coupled-mode theory[86], which states that in addition to $\Delta\epsilon$, the linewidth is proportional to the thickness of the grating, $t_{Si_3N_4}$, but inversely proportional to the propagation constant of guided-mode β. The sensitivity, especially when the biolayer is a very thin layer, depends on the spatial extent of the mode and its overlap with the biolayer[156, 67]. This is controlled by the evanescent decay length of the guided-mode in the superstrate region, and thus n_{eff} again.

Eqns. S6 and S7 clearly show that n_{eff} is determined primarily by normalized core thickness, $t_{Si_3N_4}/\lambda$ and its average refractive index, n_w. Significantly, the modes with higher β, and n_{eff} are confined more tightly to the core and the optical fields have smaller evanescent decay lengths in the substrate and superstrate regions. This has two critical implications. Firstly, this smaller decay length associated to larger n_{eff} results in less overlap of optical fields with the adsorbed layer and poorer sensing performance. Secondly, the linewidth is reduced because of increasing β. This highlights the fundamental trade-off between the two key parameters defining the performance of a sensor, linewidth and sensitivity. While a small linewidth requires a guided-mode with a large quality factor (Q-factor), and hence large β, sensitivity necessitates a strong interaction of the optical field with the superstrate medium, and thus a mode with looser confinement, larger leakage, smaller n_{eff}. With this treatment of Device I and Device II, we will now explain the dependence of the above-mentioned features on the physical dimensions.

In Fig. 3.3(a), we show how the thickness of Si_3N_4 GWS, $t_{Si_3N_4}$, affects the spectral response of Device I. The thickness of the waveguide core has a strong influence on n_{eff}, as shown in Eqns. S6, S7, so it also has a large impact on the spectral position of resonance under a fixed grating period, as in Eqn. S5. It is clear from Fig. 3.3(a) that the spectral position of GMR changes almost linearly with $t_{Si_3N_4}$. This makes the GMRs easily tunable to the application-at-hand, but also prone to fabrication inaccuracies. In addition, as $t_{Si_3N_4}$ is increased, n_{eff} increases[93, 26] as well as the Q-factor of the guided-mode[86], so we see a decrease in the linewidth. Indeed, in Fig. 3.3(b), we plotted the variation of Device II's sensing parameters with the thickness of GWS and the linewidth steadily decreases, as $t_{Si_3N_4}$ increases. However, the sensitivity of the sensor suffers due to the smaller interaction of the guided-mode with the biolayer. Nevertheless, as $t_{Si_3N_4}$ increases the decrease in FWHM outweighs the decrease in sensitivity, so FoM improves. However, increasing this thickness too much may obstruct or prevent the fabrication of the design because it may prevent the lift-off process or if the device is to be fabricated with etching, the long exposure time to etchant would also make the sharp features rounded[158], and the electromagnetic hot-spots may be lost. Decreasing the thickness too much, on the other hand, may result in the cut-off of the mode.

The next parameter that we modified is the periodicity, P, of the unit-cell. The reflection map shown in Fig. 3.3(c) indicates that the resonance wavelength changes linearly with the unit-cell periodicity, but the effect on n_{eff} is opposite to that of $t_{Si_3N_4}$. To illustrate, while increasing $t_{Si_3N_4}$ under fixed P increases n_{eff}, increasing the periodicity under fixed $t_{Si_3N_4}$ decreases β and n_{eff}, from Eq. 3.3. Its effect on the sensing parameters is plotted in Fig. 3.3(d), and they are in agreement with our reasoning by n_{eff}. Device II with larger unit-cell period has large sensitivity and large bandwidth due to a more loosely confined mode, while the opposite is true for small periodicity. As the period gets smaller, the Figure of Merit is again dictated by the decrease in the linewidth as opposed to the decrease in the sensitivity. Lastly, the linear dependence of resonance position to the periodicity gives Device I great tunability, but also sensitivity to fabrication imprecisions. Decreasing the periodicity too much can give Device II

very large FoM at the cost of a more strenuous electron-beam lithography step while fabricating the grating. Increasing the periodicity too much may cause GMR to disappear, due to decreased β and n_{eff}, from Eq. 3.5.

Finally, we examined the effect of the width of each stripe, w, of the 2D GWS, and obtained the reflection map in Fig. 3.3(e). We divide our analysis to two in this section: w above 60 nm and w below 60 nm. For the former, we observed that as w is increased beyond the mode cut-off, it causes the red shift of the resonance wavelength. Additional higher order modes also start coupling to the waveguide, as it is increased even further. All of these can be explained by considering the fill-factor of the grating material, and the resultant average refractive index of the GWS[88, 93]. Increasing w increases the fill-factor of Si_3N_4 with respect to superstrate, so the GWS assumes a larger average refractive index, n_w. Based on asymmetric dielectric slab waveguide theory[93, 150], this allows the waveguide to support more modes and increases the effective mode index, n_{eff}, of existing modes. Therefore, Eq. 3.5 requires the red shifting of resonance wavelength, because β is a constant under constant grating period, P. The increased mode confinement causes a decrease in the linewidth, as shown in the right-half portion of Fig. 3.3(f). For the sensitivity, increasing the width too much is very detrimental because not only the filling factor of the superstrate material, and thereby its weight in n_w decreases, but also the spatial overlap of the guided-mode with the superstrate reduces. The decrease in sensitivity with increased w is clearly visible in the right-half portion of Fig. 3.3(f). This region offers an interesting possibility for sensing, however. Instead of measuring the wavelength of a single GMR, one can look at the difference of the spectral positions of two resonances. This would eliminate the effect of noise sources, as their effect is common in both modes.

When w is too small, the guided-mode proceeds toward the mode cut-off, and it eventually cannot be supported anymore, as the bottom portion of Fig. 3.3(e) shows. Interestingly, however, this region offers a very small linewidth although the mode is loosely confined to the core. This can be understood by considering the limiting case where GWS acts as a grating, but n_w of the waveguide is exactly equal to the larger one of n_{super} and n_{sub}. In such a case, the linewidth tends

to go to zero[159]. The small width of each stripe also means that the weight of the background material will be very prominent on n_w and the sensitivity will be greatly improved. Both small bandwidth and large sensitivity promises ultra-high FoM as the left-half portion of Fig. 3.3(f) shows. Although this region appears ideal for refractive-index sensing, it also has the largest intolerances to the fabrication errors because slight flaws can cause losing the entire GMR phenomenon.

To wrap up, the geometrical parameters should be determined based on the main requirement of the application-at-hand, i.e. whether a small linewidth or large sensitivity is desired, because improving one tends to diminish the other. For Figure of Merit, it should be remembered that targeting small FWHM outweighs targeting large sensitivity. In general, a device that is more tolerant to fabrication inaccuracies will offer more sensitivity instead of a small linewidth.

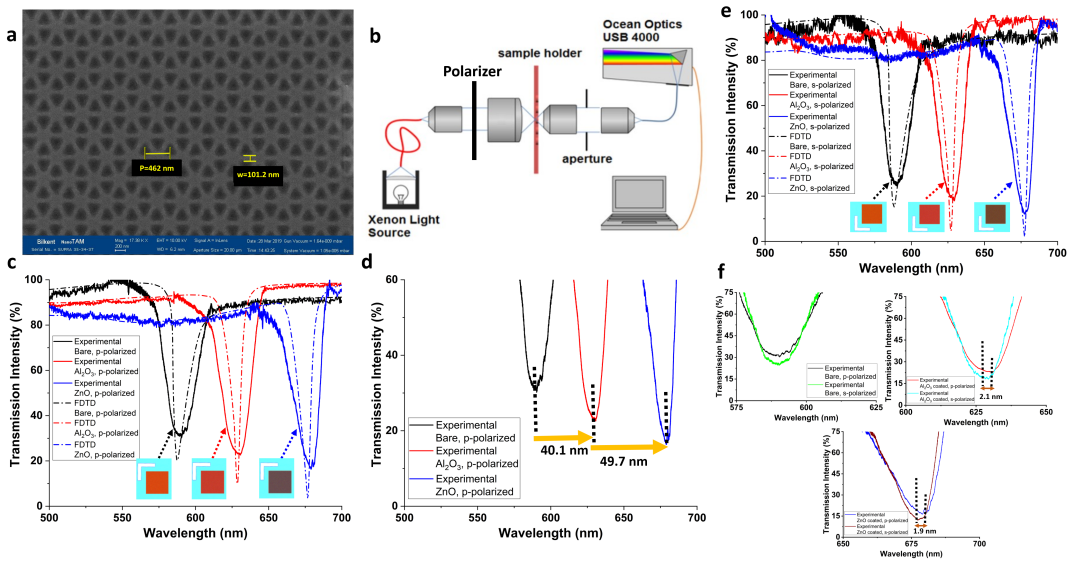

Figure 3.4: Fabrication and optical characterization of the proposed nanosensor. **(a)**: Top-view SEM micrograph of the fabricated bare device, **(b)**: Schematic diagram of the optical characterization setup. **(c)**: Experimental transmission spectra for the bare, Al_2O_3 coated and ZnO coated devices, under p-polarized incident light, **(d)**: The shift of the excited GMRs. **(e)**: Experimental transmission spectra for the bare, Al_2O_3 coated and ZnO coated devices, under s-polarized incident light, **(f)**: Insensitivity of fabricated devices to incident light-polarization by comparing the excitation wavelengths of GMRs under p- and s-polarized light for each device. In **(c)**, and **(e)**, spectrum of each device is connected to their associated optical microscope image.

3.2.3 Fabrication and Characterization of the Proposed Guided-mode Resonance based Nanosensor

The numerical results up to now have demonstrated that colorimetric and near-absolute polarization-insensitive sensing of the changes in the refractive index of the surrounding medium is possible in a lossless, all-dielectric nanosensor, owing to the excitation of guided-mode resonances. As a proof-of-concept, we fabricated the proposed device with the procedure outlined in the Methods section. To

investigate refractive-index sensing, the bare sample is compared with two other samples, on which 30 nm of Al_2O_3 and ZnO are coated, respectively, with ALD. ALD is preferred because it best imitates the attachment of target analytes by producing uniform, conformal, and pinhole-free layers with very high thickness precision. Fig. 3.4(a) shows the scanning electron microscopy (SEM) the top view of the patterned, bare nanosensor. In fabricating the proposed device, P is set constant at 460 nm, while w is chosen as 100 nm, in an effort to increase the tolerance to the fabrication inaccuracies. $t_{Si_3N_4}$ is chosen as 150 nm in order not to excite higher-order modes of the waveguide. In finding the transmission spectrum, a custom-made optical-setup, whose details are given in the Methods section, is used. Fig. 3.4(b) show the schematic diagram of the optical-setup. The slight adjustments we have made in the FDTD simulation setup to better model the experimental conditions are outlined in the Methods Section.

In our initial set of experiments, we characterized the bare, Alumina coated, and ZnO coated samples under p-polarized light. The experimental transmission spectrum for these devices, compared with their corresponding FDTD simulations are given in Fig. 3.4(c). The results in Fig. 3.4(c). show that the resonance position of all the samples are in good agreement with the numerical results, but the experimentally measured resonances are broadened and have larger dip magnitudes. This is primarily because of the following: in the FDTD simulations, we utilized perfect and infinite periodicity of a unit-cell, imported from Fig. 3.4(a). In reality, however, there are slight variations between the individual hexagonal unit-cells and the number of them is finite. These perturbations, i.e. deviations from ideal conditions, contribute to more leakage of the guided-mode which in turn broadens and weakens the resonance. Similar to our discussion in the numerical part, the linewidth is observed to be the narrowest when $\Delta\epsilon$ is the smallest. Indeed, the best FWHM is observed for ZnO coated samples, and it is 22.1 nm. As aforementioned, the position of the resonances and their shift with changing background is mainly controlled by the fill factor of the grating material, and there is perfect agreement with the numerical and experimental results. The shift of resonances is investigated further in detail in Fig. 3.4(d). to determine the sensitivity. The resonance shift between larger n_{bio} materials (Al_2O_3

and ZnO) are higher, as also observed in the numerical analysis. The maximum experimental sensitivity of proposed our all-dielectric nanosensor is recorded as $S_{\max} = \Delta\lambda/\Delta n = 49.5nm/(1.983 - 1.778) = 241nm/RIU$, which is comparable to its plasmonic counterparts. Next, we performed the same set of experiments with s-polarized light, and the experimental results are plotted in Fig. 3.4(e). The results and discussions are similar to p-polarization case. In s-polarization case, however, the resonances all have smaller linewidths and smaller dip values. The smallest linewidth is reached as low as 19 nm, while the maximum sensitivity is measured as $S_{\max} = 235.2nm/RIU$. Similar to the previous numerical results, the decrease in the linewidth predominates the decrease in sensitivity. The satisfactory experimental Figure of Merits of 10.9, 12.3 are obtained for p-polarized and s-polarized incident radiations, respectively.

For practical settings, the observation of the samples with the naked eye is of paramount importance. In our observed nanosensor devices, we observed clearly distinguishable color differences between different samples (of only 30 nm adsorbed layer), as in Figs. 3.4(c,e), by merely using a simple optical microscope. The nearly identical color of the samples is an indication of insensitivity to the polarization of incident light, which is verified quantitatively by comparing the transmission spectra of the samples under p- and s-polarized incident light. The results are demonstrated in Fig. 3.4(f)., where it can be seen that the bare samples have nearly the same resonance position, whereas for the coated samples, the difference between peak positions is only 2 nm. As a result, colorimetric and near-absolute polarization insensitive detection of ultra-thin layers of adsorbed molecules is verified by using minimal instrumentation. This makes our proposed device highly applicable to point-of-care personal diagnostics and field analyses.

3.3 Methods

3.3.1 Fabrication of the Nanosensor Device

For the fabrication of the samples, first, a typical commercial square-shaped Quartz substrate with 144 mm^2 area has been cleaned with Acetone, Isopropanol (IPA), and deionized water, and then has been dried with N2 flow, to be used as a substrate. The surface was further treated using oxygen plasma for 5 minutes before starting the deposition of thin films. Firstly, 150 nm thick Si_3N_4 layer is coated by using a Plasma-Enhanced Chemical Vapor Deposition (PECVD) system (SAMCO). This process is carried out with SiH_4, NH_3, and N_2 flow rates of 160, 6, and 500 sccm, respectively, at a temperature of 275 °C, RF power of 130 W, and pressure of 75 Pa. Electron beam lithography (RAITH E-Line Plus) was employed to fabricate the hexagonal grating unit-cell, with the resist ZEP520A resist. Electron beam exposure is then performed with a beam writer at an accelerating voltage of 30 kV, aperture size of 7 μm, working distance of 6 mm, and 22 pA beam current. To obtain our desired dimensions, we used an exposure dose of 60 $\mu C/cm^2$. After the exposure, the samples are developed at room temperature, by utilizing xylene solution for 4 minutes, followed by immersion in IPA for 30 seconds. Then, inductively coupled plasma (ICP) reactive-ion etching (RIE) is performed (SAMCO), with the following etching conditions: Flow rates of SF_6 and Argon at 4 sccm and 20 sccm, respectively, and at an RF power of 10 W and pressure of 0.6 Pa. The ZEP resist is subsequently stripped by an ultrasonic bath in NMP at 50 °C, for 15 minutes. Fig. 3.4(a). shows the hexagonal grating pattern with P=460 nm and w=100 nm.

3.3.2 Optical Characterization

A custom-made optical setup has been used for the transmission measurements of the samples. The setup comprises of a spectrometer (OceanOptics-USB4000), a

personal computer (PC), and a Xenon light source (Spectral Products ASB-XE-175). Light is transmitted by a multimode optical fiber to a lens that illuminates the nanosensor through a collimating lens. In between this lens and the input, the light is polarized by a mounted linear polarizer with indexed rotation (Thorlabs RPS1X15). Collimated and polarized light is focused onto the sample by a focusing lens, and then transmitted through the biosensor and collected by the imaging lens. The image is projected onto an aperture that enables only the signal from the selected region of the sample being measured to be transmitted. Another focusing lens couples this signal to the collection fiber. The spectrum is then measured by the spectrometer. The dispersion effect of the dielectric layers mentioned in this study is determined by J.A. Woollam Co. Inc. V-VASE ellipsometer, and they are in good agreement with the models based on Sellmeier equation[160]. These optical constants are input to the numerical simulations.

3.3.3 Numerical Simulations

In the FDTD simulations, we illuminated the unit-cell with a broadband plane-wave at normal incidence whose electric-field is polarized in the x-direction ($\phi = 0$, p-polarization), as in Fig. 3.1(c). In the x and y directions of the simulation region, we use periodic boundary conditions, while in the z-direction perfectly matched layers (PML) are adopted and they are placed 4 wavelengths away from the structure. We use two monitors that are an adequate distance away from the structure to find the reflected (R) and transmitted (T) power, normalized to the incident power. In simulating the fabricated devices, all of the FDTD simulations are performed by importing the SEM image of the structure in Fig. 3.4(a) to the Lumerical FDTD solver software[161], and defining it as the top layer. The biolayer is defined as shown in Fig. 3.2(c). with the biolayer thickness, t_{bio} of 30 nm. All of the structures are modeled with rounded top-edges and a radius of the curvature of 10 nm.

3.3.4 Theoretical Analysis of excitation of guided-mode resonances in the proposed 2D- grating

To shed some light on the physics behind this behavior, when the device is off-resonant, none of the diffracted wave orders from the grating can satisfy the conditions to become a guided-mode of the waveguide. So, the device essentially behaves as a multilayer film that mostly transmits the incoming wave, and some part is reflected due to Fresnel reflection. At resonance, however, a diffracted order can excite a guided-mode of the waveguide core. As the guided-mode propagates, the periodicity in the waveguide core causes it to continually radiate and leak energy to far-field. Accordingly, the phenomenon can be named as terms leaky-mode or quasi-guided mode resonance, as well[162]. The sharp increase in the reflection is due to the fact that the re-radiated waves interfere destructively with the directly transmitted waves, but constructively with the reflected waves. A more rigorous analysis is given in the Supporting Information.

To make the analysis more rigorous, the phase difference, Φ between directly transmitted waves, and secondary transmitted waves that after the guided-mode is re-diffracted is given by Eq.3.1[86]. On the other hand, a waveguide mode is supported if it satisfies the self-consistency constraint, given in Eq.3.2[93, 150]. Comparing these two equations shows that if Eq.3.2 (properly exciting a guided-mode) is satisfied, then Φ needs to be an odd integer multiple of π by Eq.3.1, so the transmitted waves to interfere destructively, and transmission is suppressed.

$$\Phi = 2ht_{Si_3N_4} + \Phi_{w,sub} + \Phi_{w,super} - \pi \tag{3.1}$$

$$m2\pi = 2ht_{Si_3N_4} + \Phi_{w,sub} + \Phi_{w,super} \tag{3.2}$$

where $h = k_0\sqrt{n_w^2 - n_{eff}^2}$ is the transverse component of the wavevector in the waveguide-grating, $k_0 = 2\pi/\lambda_0$ is free-space wavenumber, λ_0 is the free-space wavelength, n_w is the refractive index of the GWS, n_{eff} is the effective refractive index of the guided-mode in the core, and m is the order of the mode. The first term in both equations is due to the phase accumulated as guided-mode travels propagates inside the waveguide. The π term in Eq.3.1 is because, each diffraction

causes $\pi/2$ phase difference[163]. $\Phi_{w,sub}$ and $\Phi_{w,super}$ come from the total-internal reflection at the waveguide-substrate, and waveguide-superstrate boundaries, and the expressions for these are given in Eqns. 3.3 and 3.4, respectively[86].

$$\Phi_{w,sub} = -2\tan^{-1}[(\frac{n_w}{n_{sub}})^{2\rho} * \frac{p}{h}] \tag{3.3}$$

$$\Phi_{w,super} = -2\tan^{-1}[(\frac{n_w}{n_{super}})^{2\rho} * \frac{q}{h}] \tag{3.4}$$

where $p = k_0\sqrt{n_{eff}^2 - n_{sub}^2}$ $q = k_0\sqrt{n_{eff}^2 - n_{super}^2}$ and are the exponential decay constants in substrate (SiO_2) and superstrate regions, respectively. ρ is 0 for TE, 1 for TM modes; n_{super} and $n_{sub} = n_{SiO_2}$ are the refractive indices of the superstrate and substrate.

The effective index of refraction associated with the guided-mode inside the waveguide is not only controlled by Eq.3.2, but also with the phase-matching condition. In other words, the real part of the complex wavevector component of the guided-mode in the direction of its propagation is equal to the components coming from the reciprocal lattice vector of grating and the incident wave[86, 87]. Eq.3.3 provides the phase-matching condition for the devices with 2D grating[157], such as Device I in the main text, under normally incident light.

$$\begin{aligned} k_{x,g} &= mK_x = n\frac{2\pi}{\Lambda_x} = n\frac{2\pi}{P\sqrt{3}} \\ k_{y,g} &= mK_y = l\frac{2\pi}{\Lambda_y} = l\frac{2\pi}{P} \\ \beta &= |k_{x,g}\hat{\mathbf{x}} + k_{y,g}\hat{\mathbf{y}}| \\ n_{eff} &= \frac{\beta\lambda_0}{2\pi} \end{aligned} \tag{3.5}$$

where β is the propagation wavenumber along the guiding direction, Λ_x (K_x) and Λ_y (K_y) is the grating periods (reciprocal lattice vectors) along x and y-directions, respectively. n (l) is the diffraction orders along x (y)-direction, and $k_{x,g}$ ($k_{y,g}$) is the wavevector component of the guided-mode along x (y)-direction.

Plugging-in Eqns. 3.3 and 3.4 inside Eq. 3.2 results in the well-known transcendental mode equations for TE and TM modes, given by Eqns. 3.6 and 3.7,

respectively.

$$\tan(ht_{Si_3N_4}) = \frac{p+q}{h(1-\frac{pq}{h^2})} \tag{3.6}$$

$$\tan(ht_{Si_3N_4}) = \frac{\overline{p}+\overline{q}}{h(1-\frac{\overline{pq}}{h^2})} \tag{3.7}$$

where $\bar{p}$ and $\bar{q}$ are defined as $p * n_w^2/n_{sub}^2$, $q * n_w^2/n_{super}^2$, respectively.

Chapter 4

Near-absolute polarization insensitivity in graphene based ultra-narrowband perfect visible light absorber

This chapter is on part reprinted with permission from: **Deniz Umut Yildirim**, Amir Ghobadi, and Ekmel Ozbay, Near-absolute polarization insensitivity in graphene based ultra-narrowband perfect visible light absorber. Scientific Reports, 2018, 8, 15210, https://doi.org/10.1038/s41598-018-33609-2.

4.1 Introduction

In this section, we employ the finite-difference-time-domain (FDTD) method to numerically propose a novel design that uses a 2-dimensional sub-wavelength grating structure to excite the GMRs of an unmodulated slab waveguide. The critical coupling of the GMRs to graphene yields 99.2% light absorption with 0.8 nm FWHM at 678 nm, under p-polarized (TM) light. The proposed device

preserves perfect absorption > 98% at all source polarizations as well as the spectral position of the resonance. To the best of our knowledge, this is the first study that illustrates an FWHM below 1 nm with near-absolute polarization independence. Furthermore, the presence of a waveguide structure, instead of 1DPCs or FP cavities, relaxes the device fabrication. The spectral position of the resonance is easily tunable by changing the key geometrical parameters of the device. We first show the enhancement of graphene absorption in a simple optimized grating-core-substrate structure and scrutinize the effect of geometrical parameters on the device characteristics. In the second part, we add a metal back mirror and optimize the geometry accordingly to achieve critical coupling, and hence perfect absorption with the ultra-narrow bandwidth. We discuss the design considerations to maximize absorption strength and minimize absorption bandwidth, for each case.

4.2 Results and Discussion

4.2.1 Exciting guided-mode resonances of a slab-waveguide to improve light-graphene interaction.

Our proposed device in Fig. 4.1(a) is designed to excite the guided-modes in the high-refractive index Tantalum pentoxide (Ta_2O_5), unmodulated core dielectric region by a unique 2-dimensional sub-wavelength polymethyl-methacrylate (PMMA) dielectric grating. The structure is supported by glass (SiO_2) substrate. We call this two-port structure Device I. Fig. 4.1(b) shows the top-view of Device I to indicate the details of our novel 2D sub-wavelength grating, which is based on our previous effort on achieving polarization-insensitivity in wideband plasmonic absorbers[149]. The dielectric layers and monolayer graphene of Device I are shown in Fig. 4.1(c). The critical design parameters in determining the spectral position of GMRs and the absorption strength are the thickness of the core region, $t_{Ta_2O_5}$; the periodicity, P, of the unit cell in y-direction, the grating width w, and the grating thickness t_{PMMA}.

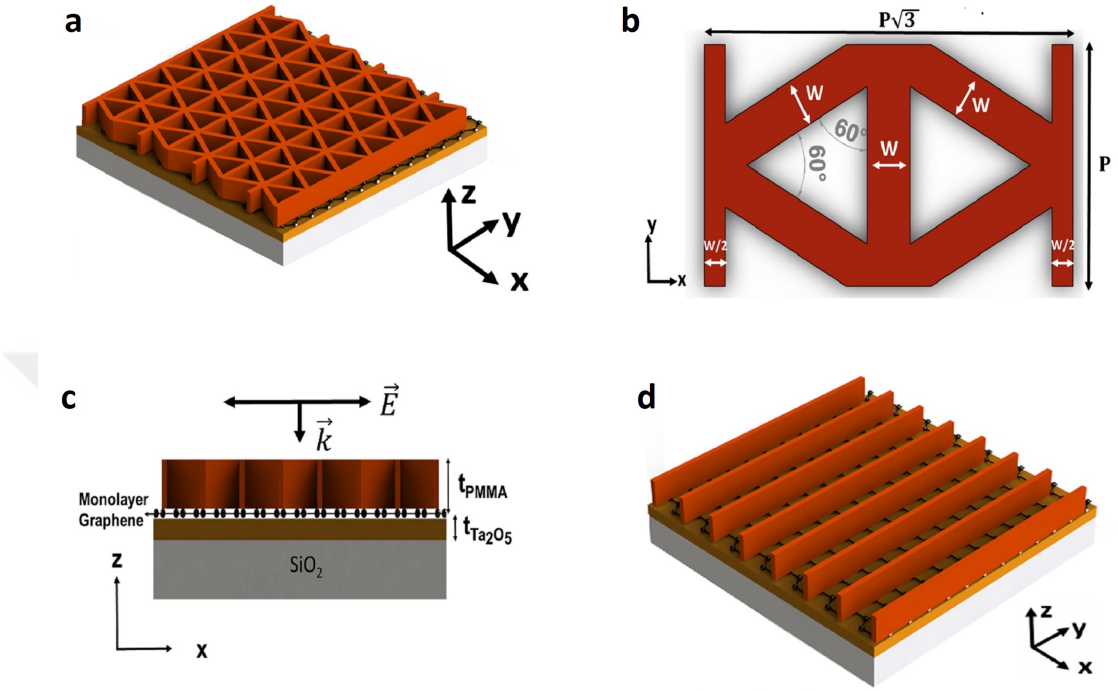

Figure 4.1: The proposed design, its unit-cell and the structure with the classical 1D grating (a) Device I to excite GMRs and enhance light-graphene interaction. **(b)** Unit-cell of Device I, detailing the 2D grating, seen from top-view. **(c)** Dielectric layers and the monolayer graphene of Device I, seen from side-view. **(d)** The structure with the commonly used 1D-grating. In **(c)**, the device is illuminated by p-polarized plane wave.

To investigate the spectral response of Device I, we utilize finite-difference-time-domain simulations. In the numerical simulations, we illuminated the unit-cell with a broadband plane-wave at normal incidence whose electric-field is polarized in x-direction ($\phi = 0$, p-polarization). In the x and y directions, we use periodic boundary conditions, while in the z-direction perfectly matched layers (PML) are adopted and they are placed 5 wavelengths away from the structure. We use two monitors that are at an adequate distance away from the structure to find the reflected (R) and transmitted (T) power. Absorption is then found by using $A = 1 - R - T$ formula. The dispersion effect of the dielectric materials are retrieved by ellipsometric measurements, and they are in good agreement with the models based on Sellmeier equation[160]. In the material fits, the only non-zero extinction coefficient comes from Ta_2O_5, and is equal to 10^{-5}. It is then reasonable to regard the device as lossless without graphene. Graphene is

modeled as a 2-dimensional material with infinitesimal thickness and a complex surface conductivity that includes the chemical potential, scattering rate and temperature effects, based on Kubo formulation [164]. The surface conductivity is divided into intraband and interband contributions, as given in Eqns. 4.1 and 4.2, respectively.

$$\sigma_g(w, \mu_c, \Gamma, T) = \sigma_g^{intra}(w, \mu_c, \Gamma, T) + \sigma_g^{inter}(w, \mu_c, \Gamma, T)$$

$$\sigma_g^{intra}(w, \mu_c, \Gamma, T) = \frac{je^2}{\pi\hbar^2(w - j2\Gamma)} \int_0^\infty \epsilon(\frac{\partial f_d(\epsilon)}{\partial \epsilon} - \frac{\partial f_d(-\epsilon)}{\partial \epsilon})d\epsilon \tag{4.1}$$

$$\sigma_g^{inter}(w, \mu_c, \Gamma, T) = \frac{-je^2(w - j2\Gamma)}{\pi\hbar^2} \int_0^\infty (\frac{f_d(-\epsilon) - f_d(\epsilon)}{(w - j2\Gamma)^2 - 4(\epsilon/\hbar)^2}d\epsilon \tag{4.2}$$

where j is the imaginary unit, e is the elemental charge, w is the angular frequency, T is the temperature, $\hbar = h/2\pi$ is the reduced Planck's constant, Γ is the scattering rate, and μ_c is the chemical potential. $f_d(\epsilon) = (e^{(\epsilon-\mu_c)/k_bT} + 1)^{-1}$ is the Fermi-Dirac distribution and k_b is Boltzmann's constant.

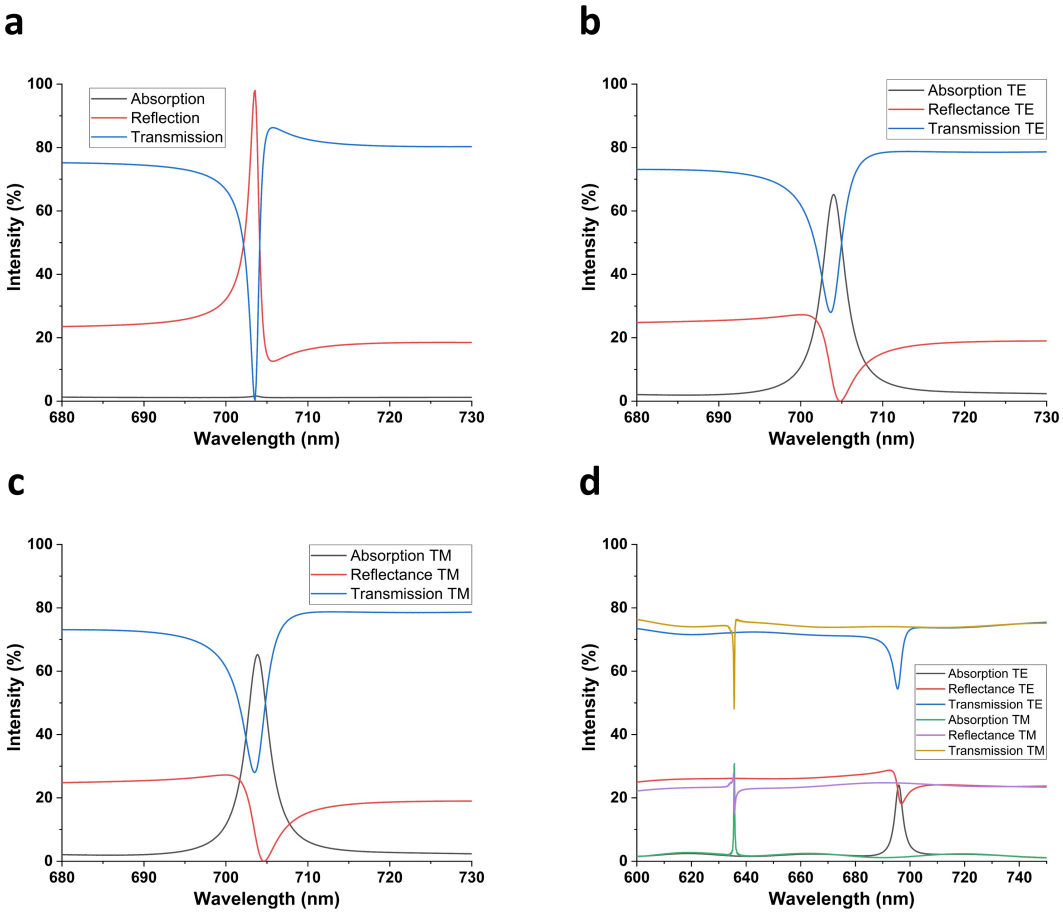

Figure 4.2: Excitation of GMRs and enhancement of light-graphene interaction. Transmission, Reflectance and Absorption spectra for the proposed device **(a)** without graphene, **(b)** with graphene, under s-polarized (TE) light; **(c)** with graphene, under p-polarized (TM) light; **(d)** with 1D grating and graphene, under TE and TM polarized light to show polarization dependency.

First of all, we set the design parameters $t_{Ta_2O_5}$, P, w, and t_{PMMA} to their optimum values of 90 nm, 500 nm, 100 nm (0.2P) and 220 nm, respectively. We simulated Device I without graphene to gain insight about the resonance excitation and to confirm that the device is almost lossless. The simulation result in Fig. 4.2(a) shows a sharp guided-mode resonance peak at 703.565 nm, and only 1% absorption due to Ta_2O_5. It is then safe to associate the absorption in subsequent simulations to graphene. In Fig. 4.2(a), when the device is off-resonant,

no diffracted order is coupled to the waveguide, so the device essentially acts as a multilayer film that mostly transmits the incoming wave, and some part is reflected due to Fresnel reflection. When on-resonant, however, one of the diffracted orders couple to the guided-wave in slab waveguide core. The initially diffracted waves of incident wave and the re-diffracted waves of the guided-wave then interfere destructively to produce a transmission filtering response. Essentially, the condition for the particular diffracted order to be guided and the other diffracted orders interfering destructively lead to the same condition[86]. Another condition for the occurrence of the resonance is the phase-matching condition, i.e. the real part of the complex wavevector component in the travelling direction of the guided-mode is equal to the components coming from the reciprocal lattice vector of grating and the incident wave[86, 111, 126]. Eq. 4.3 provides the phase-matching condition for the devices with 1D grating, as in Fig. 4.1(d) under normally incident light. We call the device in Fig. 4.1(d) Device 0.

$$\begin{aligned} \beta = k_0 n_{eff} &= m\frac{2\pi}{\Lambda} \\ n_{eff} &= m\frac{\lambda_0}{\Lambda} \end{aligned} \tag{4.3}$$

where β is the propagation wavenumber along the guiding direction, k_0 is the free-space wavenumber, n_{eff} is the effective refractive index of the mode inside the core, m is the diffraction order, λ_0 is the free-space wavelength and Λ is the grating period. Writing an analytical expression for the phase-matching condition in Device I is cumbersome because our grating diffracts incoming waves in not only the x-direction but also in the y-direction, as opposed to the explicitly used devices with 1D grating [123, 124, 125, 126, 127, 128] does. Therefore, the guided-mode's propagation direction is not simply the x-direction as in Device 0. This makes numerical methods necessary to fully discern the resonances. Another interesting feature of GMRs is their Fano lineshape. It arises due to the interaction between a sharp resonance channel and the broad radiation continuum[151]. Critically, the zeroth order diffracted wave is a propagating wave, while all other diffracted orders are evanescent due to the sub-wavelength nature of the grating. Therefore, we have evanescent coupling of the incident wave to the guided-mode.

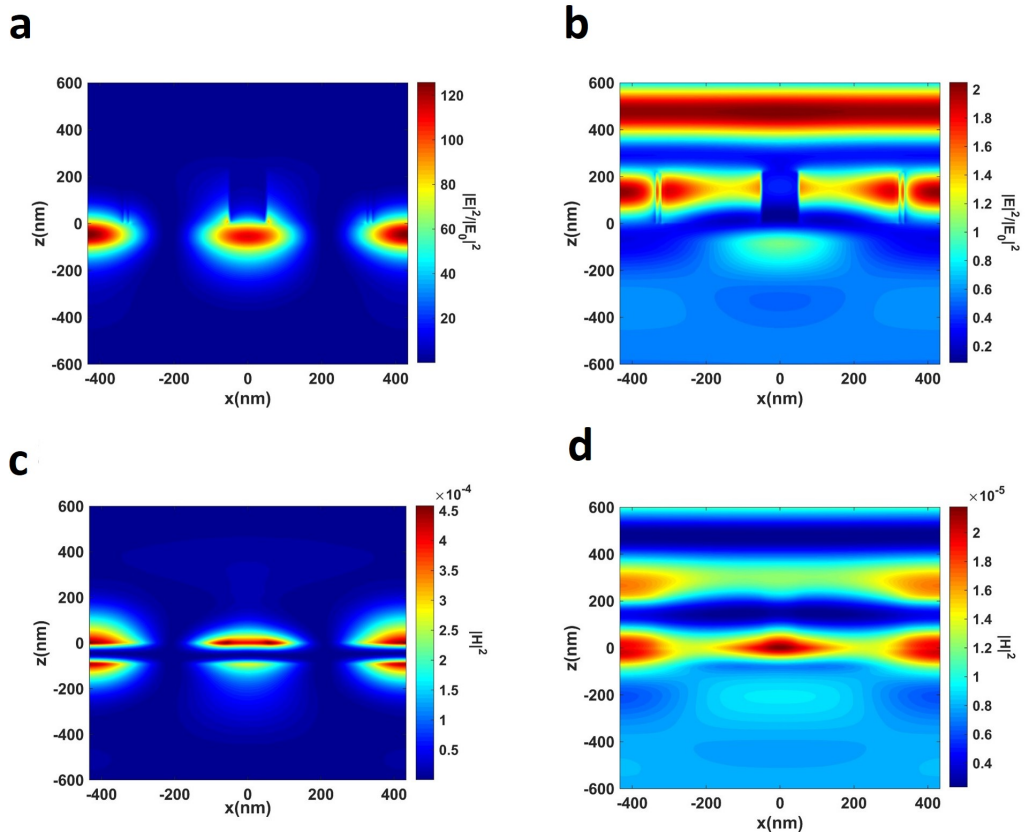

Figure 4.3: Distribution of electric and magnetic field in the on and off-resonant conditions. $|E|^2/|E_0|^2$ at XZ plane during **(a)**: on-resonance at 703.82 nm; **(b)**: off-resonance at 751.9 nm; $|H|^2$ at XZ plane during **(c)**: on-resonance, **(d)**: off-resonance . $|E|^2$ and $|H|^2$ are the modulus of electric and magnetic field inside the device, $|E_0|^2$ denotes that of incident light. Graphene is located at z=0.

We then sandwiched monolayer graphene between the grating and Ta_2O_5 to increase the light-graphene interaction, thanks to the guided-wave confined in the waveguide[116]. The spectral response of the configuration is shown in Figs. 4.2(b,c), for the s (plane of incidence is XZ plane, E-field polarized in y-direction) and p (plane of incidence is XZ plane, E-field polarized in x-direction) polarized incident waves, respectively. From these figures, it is obvious that the structure gives almost identical results in terms of both the absorption strength and the

resonance's spectral position (65.22% at 703.82 nm for p, 65.17% at 705.05 nm for s). The FWHM of the resonance is also maintained at 3.5 nm. To demonstrate the polarization insensitivity of Device I compared to Device 0, we examined the spectral response of the latter with the structural parameters of the former under s and p-polarized lights. Fig. 4.2(d) shows the absorption spectrum for Device 0. Although Device 0 can be optimized to maximize absorption strength, the key point in Fig. 4.2(d) is that both the spectral position and the strength of absorption are affected from incident light's polarization. Ref.[126] also found that simple 1D grating and unmodulated slab waveguide structure has a theoretical maximum absorption of 60% without the addition on back-mirror. We, therefore, attribute both the near-stable spectral position of resonance and slightly enhanced absorption to our novel grating design.

Figs. 4.2(b,c) demonstrate that absorption at the resonance arises mostly due to the detriment of reflection, while a considerable amount of transmission still remains, in harmony with the results reported in ref.[126]. While Fig. 4.2(a) for Device I without graphene shows almost the complete suppression of transmission, in Device I with graphene it can never be zero because of two reasons. First, the guided-wave itself is leaky and leaks out evanescent waves to not only graphene (which is the reason of absorption enhancement) but also to the substrate. More importantly, the re-diffracted waves of the guided-mode cannot fully cancel out the initially diffracted waves because of their decreasing amplitude due to graphene.

To get further comprehension about the improvement in the light-graphene interaction, we extracted the electric and magnetic field profiles for both off-resonant and on-resonant cases. A comparison of the fields in the off and on-resonant cases, shown in Fig. 4.3, clearly indicates a strong field enhancement and localization on graphene. While $|E|^2$ is enhanced two orders of magnitude with respect to the incident light, $|H|^2$ is enhanced one order of magnitude. The enhanced optical field on graphene is directly responsible for the absorption enhancement, in accordance with Eq. 4.4[93],

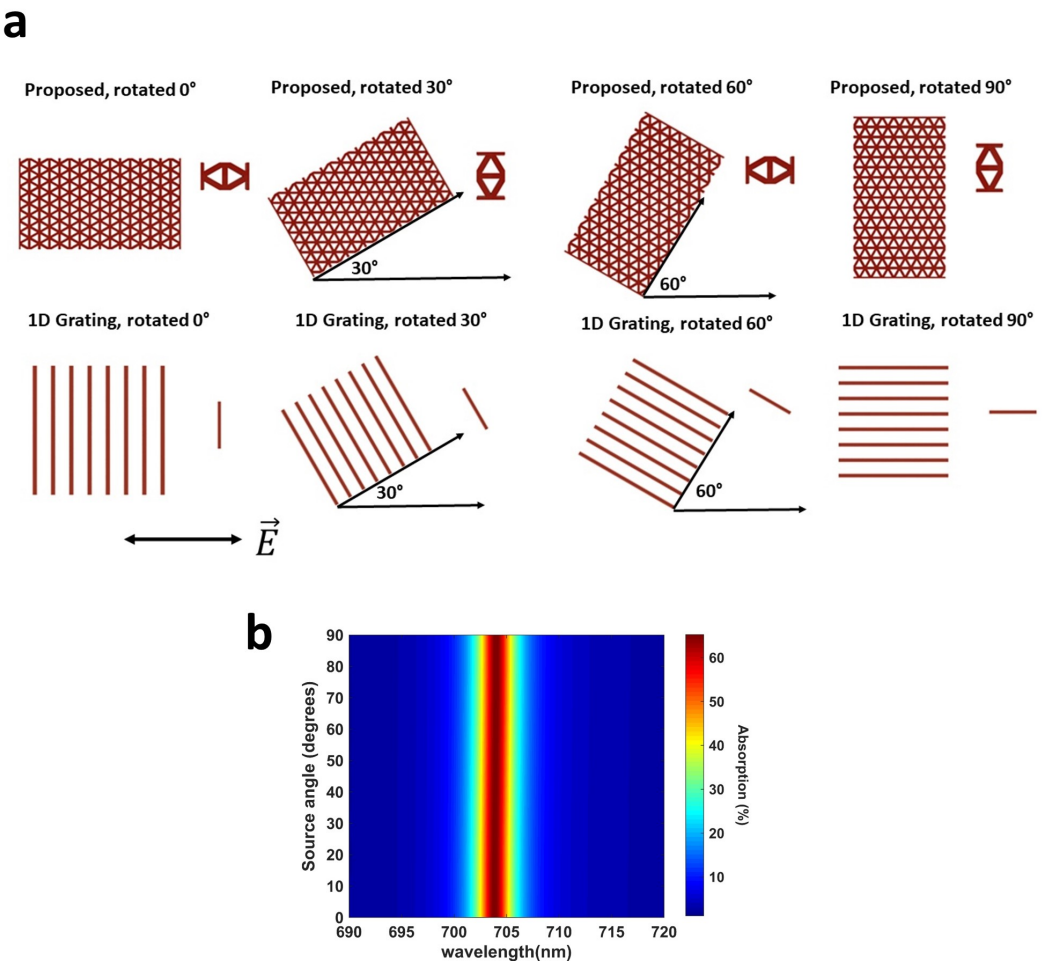

Figure 4.4: **(a)** Comparison of the unit-cells of the proposed design and the 1D-grating design under different rotations of Device I. **(b)** Absorption map of Device I for the polarization angles spanning from 0° (p,TM-polarization) to 90° (s,TE-polarization).

$$A(\lambda) = \frac{\int\int_{x,y\in layer} w\epsilon_0 n'' n' |E|^2 dxdy}{I(\lambda)} \tag{4.4}$$

where ϵ_0 is the vacuum permittivity, λ and $I(\lambda)$ are the wavelength and the intensity of the light, respectively, n'' and n' denote the imaginary part (extinction coefficient) and real part of the complex refractive index, respectively. The

enhancement of fields is slightly higher than the designs incorporating slab waveguide as the guiding layer [125, 126, 127]. We also observe that the standing wave pattern is created in both the z and x-directions. While the former is because of the waveguiding effect, the latter is due to the refractive index modulation in the x-direction[124]. The electric field profile in Fig. 4.3(a) implies that the first order mode of the slab waveguide is excited. This is entirely expected because of the deep sub-wavelength thickness of the core region, as the excitation of higher order modes of a waveguide requires larger core thickness[93].

4.2.1.1 Reasoning of our 2D SWG to achieve polarization insensitivity

Because it is the most important aspect of our design, we devoted this subsection to the further dissection of polarization insensitivity in Device I, by analyzing what causes the devices with 1D grating, such as Device 0, to be polarization sensitive in the first place. Firstly, different boundary conditions imposed on different polarization states, which results in form birefringence. In addition, when the guided-mode travels along the periodically segmented waveguide[92], the periodicity of the grating defines Bloch modes. Different effective refractive indices of the Bloch modes in the grating region[88] consequently define different effective mode refractive indices for TE and TM modes of the waveguide. The excitation condition of TE and TM modes are different on top of this[93, 165]. Thus, the devices utilizing 1D gratings show polarization dependency[88] as they excite the GMRs at different wavelengths. Moreover, dissimilar field distributions result in different absorption strengths.

Without considering the waveguiding effects and the complicated properties of Bloch modes, we adopted Rytov's formulas given in Eqns. 4.5 and 4.6 for s and p-polarized waves as our guideline in achieving polarization independence. Rytov's formulas use different boundary conditions forced on different polarization states

to find the effective permittivity of the medium to the zeroth order, for deep-subwavelength 1D gratings with sufficient thickness [166].

$$n_{\parallel}^2 = f n_1^2 + (1-f) n_2^2 \tag{4.5}$$

$$\frac{1}{n_{\perp}^2} = f \frac{1}{n_1^2} + (1-f) \frac{1}{n_2^2} \tag{4.6}$$

where f is the fill-factor of grating, n_1 and n_2 are the refractive indices of the grating material, and its surrounding, respectively. $n_{\parallel}$ and $n_{\perp}$ are the refractive indices of the effective medium for the s-polarized (E-field parallel to grating grooves), and p-polarized waves (E-field perpendicular to grating grooves), respectively. Any arbitrary incident polarization can then be decomposed into a superposition of s and p-polarizations to find the effective refractive index as a weighted sum of $n_{\parallel}$ and $n_{\perp}$.

From Eqns. 4.5 and 4.6, we see that it is the different interaction of different polarizations with the 1D grating that is causing polarization sensitivity. Thus, in an absolutely polarization insensitive design, the interaction of E-field with the unit-cell must be the same for all polarization angles. Equivalently, E-field with a fixed polarization angle has to "see" the same unit-cell upon rotating it arbitrarily[149]. To compare Device I with the devices using 1D grating, we kept the polarization angle at ϕ= 0 degrees, and rotated the unit-cells of each for 0, 30, 60, and 90 degrees. The result of this comparison is shown in Fig. 4.4(a). From Fig. 4.4(a), two main conclusions can be made. The first one is that although our grating cannot provide infinite rotational symmetry, its unit-cell repeats itself at every 60°, i.e. we have 60° of rotational symmetry. On the other hand, the 1D grating has different unit-cells, and hence different E-field-unit cell interactions for all polarization angles. Even though the proposed unit-cell for the 0° (60°) and 30° ((90°) are different, the interaction of E-field with the unit-cells are somewhat identical. This is because, in the first case, E-field interacts perpendicularly with two gratings [one in the center, one in the corners (2x1/2)] and it is at 30 degrees of angle with the other four tilted ones. In the second case, however, E-field is parallel to the former two gratings, but it is at 60 degrees of angle with the tilted ones to compensate for the change in the former. We explored the polarization independence of Device I in more detail by sweeping the polarization angle of the

source from 0° to 90°. Our finding in Fig. 4.4(b) clearly shows that the structure maintains almost constant absorption at a nearly fixed spectral position.

4.2.2 Technological tolerances, effect of geometrical parameters on GMRs

Results of the previous subsection demonstrate that GMRs can be excited when the phase-matching condition is satisfied, and the evanescent wave from the diffraction grating can be coupled to one of the guided waveguide modes. Although the waveguiding effects on the Bloch modes of the periodically patterned waveguide are complicated, we can still sufficiently understand how the spectral response of Device I depends on the structural parameters, by considering the optical field around graphene. Optical fields at the Ta_2O_5-PMMA (core-PMMA) and Ta_2O_5-SiO_2 (core-substrate) boundaries are highly related to the effective mode index, n_{eff}, of the guided-mode if we regard the structure as an asymmetric dielectric slab waveguide. This is done by considering the SWG as a medium with an effective dielectric permittivity[93]. Therefore, we start our discussion here by briefly reviewing the fundamental results of asymmetric dielectric slab waveguide theory[93, 150].

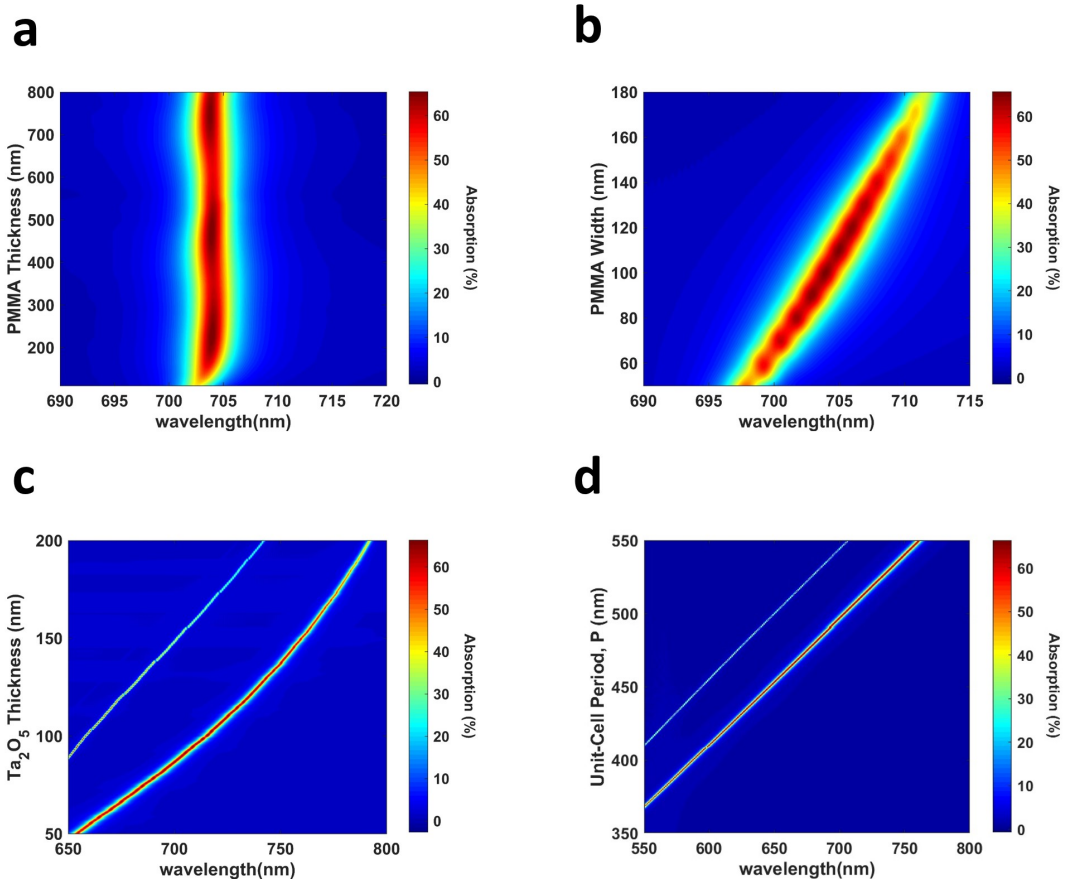

Figure 4.5: Dependence of absorption spectrum of Device I to structural parameters. Absorption spectrum of Device I under varying **(a)**: PMMA thickness, t_{PMMA}, **(b)**: PMMA width, w, **(c)**: Ta_2O_5 thickness, $t_{Ta_2O_5}$, **(d)**: unit cell periodicity in y-direction, P. When varying one parameter, we kept the other parameters at their optimum value. In the unit-cell periodicity sweeps, width of grating is kept as w=0.2P. The results are taken with p-polarized incident wave.

Eq. 4.7 and Eq. 4.8 are the guided-mode conditions in an asymmetric dielectric slab waveguide for TE and TM modes, respectively,

$$\tan(ht_{Ta_2O_5}) = \frac{p+q}{h(1-\frac{pq}{h^2})} \tag{4.7}$$

$$\tan(ht_{Ta_2O_5}) = \frac{\overline{p}+\overline{q}}{h(1-\frac{\overline{pq}}{h^2})} \tag{4.8}$$

where $h = k_0\sqrt{n_{Ta_2O_5}^2 - n_{eff}^2}$ is the transverse component of wavevector in the core, $p = k_0\sqrt{n_{eff}^2 - n_{SWG}^2}$ $q = k_0\sqrt{n_{eff}^2 - n_{SiO_2}^2}$ and are the decay constants in PMMA, SiO_2 regions, respectively. n_{SWG} is the effective refractive index of the SWG, different for TE and TM modes. $\bar{p}$ and $\bar{q}$ are defined as $p * n_{Ta_2O_5}^2/n_{SWG}^2$, $q * n_{Ta_2O_5}^2/n_{SiO_2}^2$, respectively.

It is clear from Eqns. 4.7 and 4.8 that n_{eff} is determined primarily by the thickness of the core to the wavelength ratio (normalized core thickness, $t_{Ta_2O_5}/\lambda$) and the refractive indices of the core and cladding films. Significantly, the modes with higher n_{eff} are more tightly confined in the core, so they have low and almost equal leakage to both PMMA/graphene and substrate. However, for Device I, it is shown in Figs. 4.2(b,c) that most of the absorption is due to harnessing the reflection, and it is the transmission losses that prevent the absorption from reaching 100%. Since the transmission can never be made zero in a two-port system, the optimum design must have the maximum optical field at the core-PMMA boundary, while keeping that at the core-substrate boundary minimum. This would ensure that most of the leaked power of the guided-mode is exploited as absorption, and not transmission. In one extreme, if we increase n_{eff} to a value close to the core refractive index, the field confinement is better at the core, and so is the Q-factor of resonance. Therefore, the power leaking out to the graphene/PMMA becomes small and close to that leaking to glass. This results in nearly 50% absorption. In the other extreme, when n_{eff} is too small, the mode would leak too much energy to not only PMMA but also to substrate, so absorption again cannot dominate over transmission. Thus, obtaining maximum attainable absorption requires an intermediate n_{eff}. Our discussion up to now highlights the fundamental trade-off and design consideration in the 2-port Device I, the changes to increase absorption and decrease the bandwidth also increase transmission to balance the former or even decrease it. To make things worse, increasing absorption would decrease the amplitude of the re-diffracted waves, so they cancel the originally diffracted waves less with destructive interference. This again increases transmission. Combining the phase-matching condition with this treatment of Device I, we will now explain the dependence of the absorption spectrum on geometrical parameters.

We first concentrate on the effect of PMMA thickness, t_{PMMA} on the absorption spectrum of Device I. For this purpose, we varied it over a very broad range, from 110 nm to 800 nm. The absorption spectrum in Fig. 4.5(a) shows that GMR excited at 703.82 nm is robust with respect to PMMA thickness. This implies that the PMMA thickness has only a tiny effect on the field configuration inside the core, agreeing well with the previously reported results[126, 167]. There are two main points to be made from Fig. 4.5(a). First of all, when the PMMA thickness is below a certain value, the resonance becomes weaker, because optical field around graphene decreases. This happens because the mode radiatively decays without being recombining with itself, as explained by the complex coupling coefficient between the incident field and guided-mode[86]. Secondly, the oscillation in the absorption spectrum starting after t_{PMMA}=200 nm also agrees well with Ref. [86], and it arises because of the constructive and destructive interferences between the diffracted fields from the bottom and top of grating.

Next, we investigated the effect of the width of the grating, w. The value of w is changed from 50 nm to 180 nm and we obtained the absorption map in Fig. 4.5(b). We observed that an intermediate value of PMMA SWG width is required for the maximum possible absorption, and the resonance wavelength red-shifts as the thickness increases. Both of these can be explained by considering the fill-factor of SWG that changes the effective refractive index of it [88, 93, 125, 126]. Increasing PMMA width increases the fill-factor of the grating. Thus, the SWG assumes a larger effective refractive index for both polarizations, as outlined in Eqns. 4.5 and 4.6 for the 1D-grating. This, in turn, increased the effective mode index. Eq. 4.3 for 1D grating, therefore, requires the red-shifting of resonance wavelength. The same argument applies to our 2D grating as well. When w is too high, the absorption is small because there is a considerable amount of Fresnel reflection from the air-PMMA boundary that cannot be converted to absorption. Increased n_{eff} also decreases the leakage to PMMA/graphene. On the other hand, when w is too small, the effective mode index reduces too much toward the mode cut-off that the leakage to SiO_2 starts dominating. The second explanation can be that the coupling efficiency is decreased with the thin grating. From this result, we observe that Device I can maintain the absorption strength for a large interval

of the grating width.

In Fig. 4.5(c), we show how the thickness of the Ta_2O_5 core region of the waveguide, $t_{Ta_2O_5}$, effects the response of Device I. Core thickness has a strong influence of n_{eff}, as shown in Eqns. 4.7 and 4.8, so it also has a large impact on the spectral position of resonance under a fixed grating period, as Eq. 4.3 shows for the 1D grating. This concept qualitatively applies to our 2D grating as well. Fig. 4.5(c) shows that the spectral position of the resonance changes almost linearly with Ta_2O_5 thickness, making the GMRs easily tunable, but also prone to fabrication inaccuracies. It is worth mentioning that the change in the resonance wavelength is smaller in ratio than that in the $t_{Ta_2O_5}$ because the wavelength needs to simultaneously satisfy both the phase-matching condition and the mode-equation with constant grating period, while $t_{Ta_2O_5}$ only controls the mode-equation[93, 150]. For example, when $t_{Ta_2O_5}$ is increased, the increase in the resonance wavelength is smaller in ratio, so $t_{Ta_2O_5}/\lambda$ ratio increases. This increases n_{eff}, agreeing with Eq.4.3. Finally, when $t_{Ta_2O_5}$ is increased too much, n_{eff} increases too, so we see that the absorption decreases and stays near 50%. This supports our previous argument that under large confinement to the core, absorption and transmission approach to 50% due to low and almost equal leakage to both PMMA/graphene and substrate. In Fig. 4.5(c), we also see the excitation of a second, narrower resonance that occurs at smaller wavelengths with weaker absorption strength. Hence, Device I can be used to simultaneously excite and tune the GMRs.

The last parameter that we modified is the periodicity, P, of the unit-cell. The absorption map shown in Fig. 4.5(d) indicates that resonance wavelength changes linearly with the unit-cell periodicity, but the effect on n_{eff} is opposite to that of $t_{Ta_2O_5}$. To exemplify this, while increasing $t_{Ta_2O_5}$ under fixed P increases n_{eff}, increasing the periodicity under fixed $t_{Ta_2O_5}$ increases the resonance wavelength by a smaller ratio to decrease n_{eff}, from Eq.4.3. This satisfies the mode-equations, too, because decreasing $t_{Ta_2O_5}/\lambda$ ratio also results in smaller n_{eff}[93, 150]. This is the main reason why Fig. 4.5(d) shows a low absorption strength, but smaller bandwidth when the period is small because the effective mode index is high. Lastly, the linear dependence of resonance position to the periodicity gives Device

I great tunability, but also sensitivity to fabrication imprecisions.

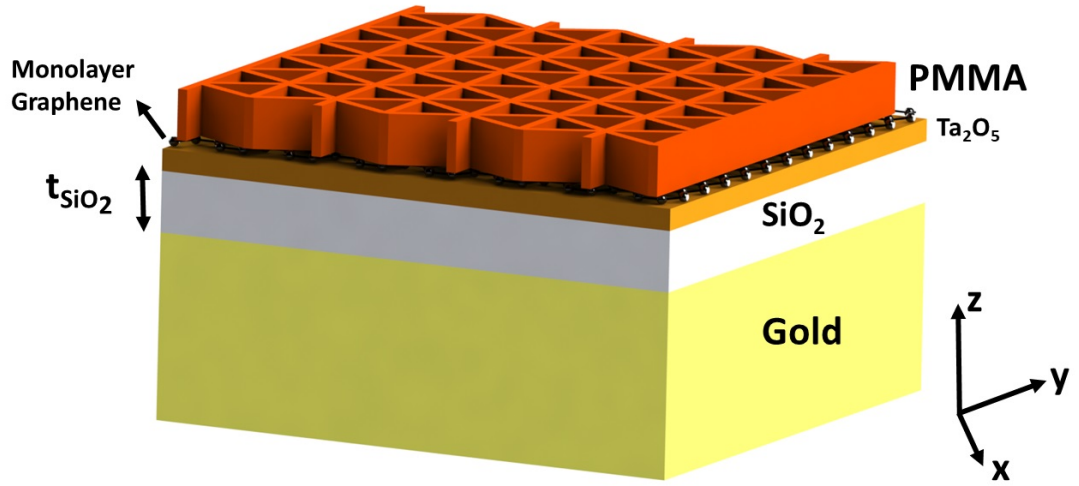

Figure 4.6: Structure of Device II, used to achieve perfect absorption by critically coupling graphene to excited GMRs. t_{SiO_2} denotes the SiO_2 thickness.

4.2.3 Achieving perfect absorption with ultra-narrow bandwidth

In a two-port system, such as Device I, perfect absorption can be achieved if the conditions of coherent perfect absorption (CPA) are satisfied, whereupon the interference and dissipation leads to perfect absorption [122, 126]. However, the optical properties of graphene in the visible range are not suitable to construct a coherent perfect absorber [126, 122]. In Device I, the main reason why 100% absorption cannot be achieved was the considerable amount of light that leaves the system, acting as transmission losses. In this respect, the total absorption of light can be achieved if the transmission channel is suppressed[167]. This can be accomplished by placing either a metallic mirror or a dielectric Bragg mirror [122, 125]. Then, all of the previously transmitted power can be redirected back

to graphene and interact with it. Coupled mode theory with time reversibility and energy conservation arguments result in the absorption spectrum described by the Lorentzian function in Eq. 4.9 [168].

$$A(\omega) = \frac{4\delta\gamma_e}{(\omega - \omega_0)^2 + (\delta + \gamma_e)^2} \tag{4.9}$$

where ω_0 is the resonance frequency, γ_e is the external leakage rate of the resonator and δ is the intrinsic loss rate due to monolayer graphene. Critical coupling and total absorption of incident light is achieved when the system is at resonance and when the leaked energy from the guided-mode is matched to the intrinsic absorption rate in graphene[93, 122, 123, 124, 125, 167, 169].

To achieve perfect absorption and retain the sub-micron thickness of Device I, we added a thick gold layer beneath Device I, to arrive at Device II, shown in Fig. 4.6. The gold layer in Device II acts a back-mirror. Its thickness, taken as 100 nm in simulations, is much larger than the skin-depth of the light at the wavelength range of interest, so the amount of light leaving Device II is insignificant. Two-port Device I, therefore, became one-port Device II. Gold layer of Device II can be replaced by a dielectric Bragg mirror, which would make the device all-dielectric and give a wider tunability range in the visible spectrum, at the expense of a more difficult fabrication process and bulkier design. Since there is negligible transmission, the absorption can now be found by simply $A = 1 - R$ formula, and maximizing it requires minimizing the reflection, which is due to the externally leaked energy from the system that is not harnessed on graphene. This can occur due to either undercoupling or overcoupling of the GMR to graphene[122]. In both cases, the external leakage rate is not equal to the intrinsic absorption in graphene. The fact that critical coupling depends on the external leakage rate makes SiO_2 thickness a critical parameter, as it controls the FP cavity modes in it [125] and consequently reflection losses [167].

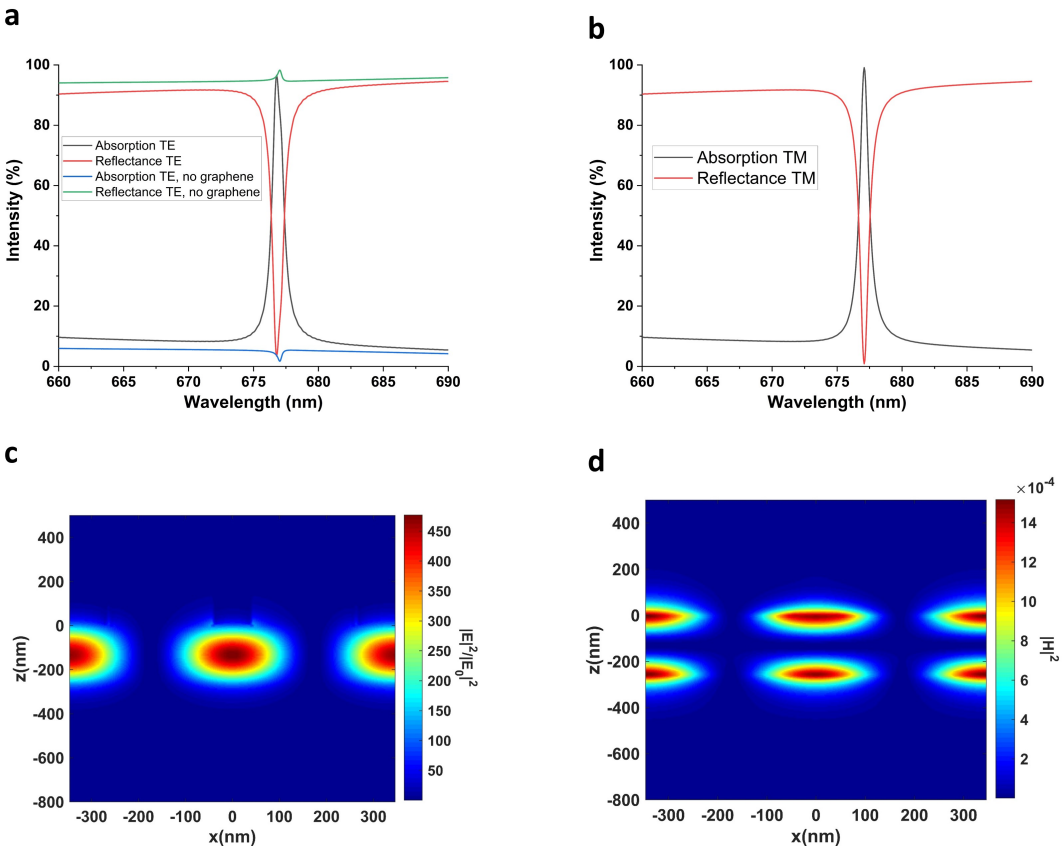

Figure 4.7: Achieving perfect absorption by critically coupling guided-mode to graphene. Absorption spectrum of Device II under **a** s-polarized, **(b)**: p-polarized light. **(c)**: $|E|^2/|E_0|^2$ at XZ plane during resonance **(d)**: $|H|^2$ at XZ plane during resonance. **(a)** also shows the absorption spectrum in the absence of monolayer graphene.

To achieve critical coupling, we set the geometrical parameters to their optimized values, i.e. $t_{Ta_2O_5}$, P, w, t_{PMMA}, and t_{SiO_2} to 260 nm, 400 nm, 80 nm (0.2P), 350 nm, and 360 nm, respectively. In the simulations, the dispersion of gold is modeled by ellipsometric measurements. The absorption spectrum for Device II with its optimized parameters is shown in Figs. 4.7(a,b), under s and p-polarized light, respectively. In these figures, we see a very sharp resonance at 676.8 nm (677 nm) with the absorption strength of 98% (99.2%) for s (p)-polarized light. The bandwidth of the resonance for both TE and TM polarization is 0.8 nm, thus giving a very high Q-factor of about 850. Here, Q-factor is defined by

Q=$\lambda/\Delta\lambda$. Fig. 4.7(a) also demonstrates the absorption of Device II in the absence of graphene. The absorption without graphene is as low as 1%, because the layer thicknesses (including t_{SiO_2}) are arranged carefully so that complete reflection occurs at resonance. When present, graphene is then responsible for the remaining 98% absorption as well as a slight blue-shift of GMR. Figs. 4.7(c,d) demonstrate the localization of electric and magnetic field in the core region of the waveguide. Comparing Figs. 4.7(c,d) to Figs. 4.3(a,c) shows that Device II stores larger energy in the core region, and the Q-factor achieved in Device II is higher as a result.

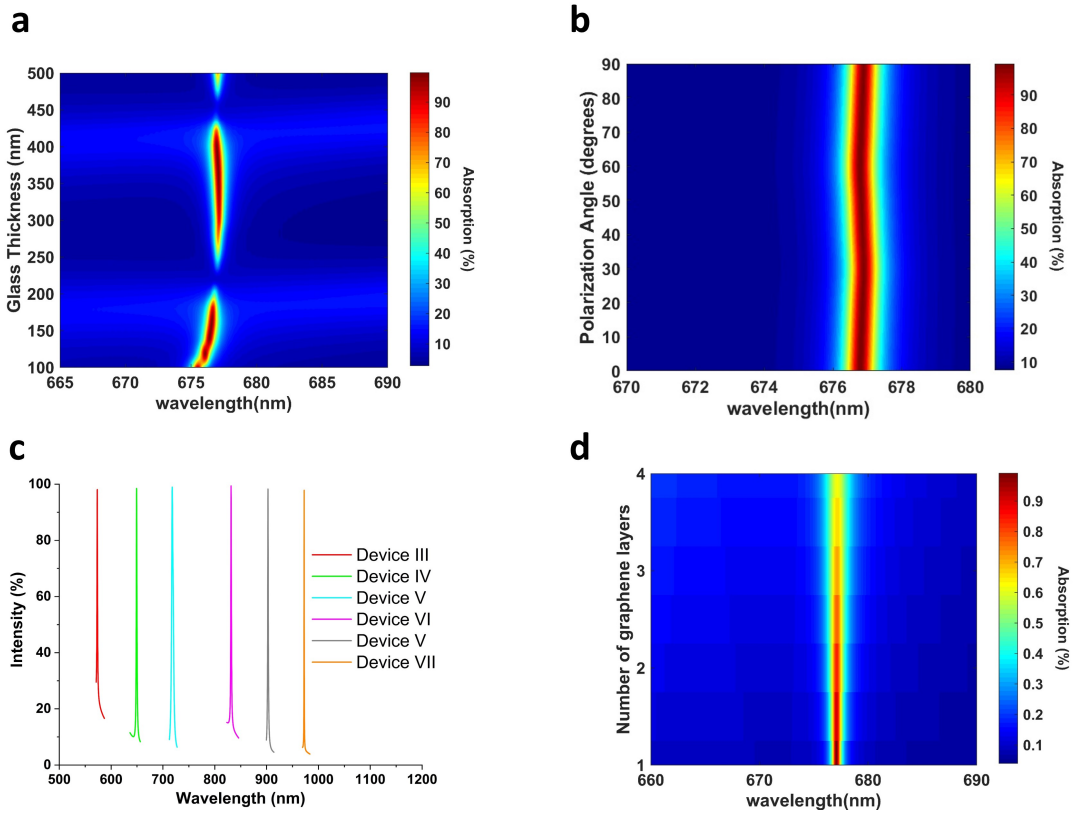

Figure 4.8: Absorption spectrum of Device II under varying **(a)**: Glass thickness, t_{SiO_2}, **(b)**: Polarization angle. **(c)**: Tuning the perfect absorption in the visible and mid-infrared ranges. $t_{Ta_2O_5}$=160, 180, 300, 300, 400 nm; P=350, 400, 550, 500, 600 nm, t_{SiO_2}= 380, 420, 260, 240, 540 nm for Devices 3,4,5,6 and 7, respectively. t_{PMMA}= 350 nm and w= 0.2P, for all designs. **(d)**: Layer-dependent absorption of Device II.

We now want to emphasize the key design strategy in achieving the ultra-narrow bandwidth. To achieve critical coupling in a system where the external leakage rate is low, a very high energy storage, or equivalently, a very high-Q GMR in the resonant structure is needed[122, 124]. Thus, the bandwidth is narrower in devices where graphene is placed far away from the optical field confined by GMR. Although this strategy results in a narrower bandwidth, the necessity of creating a very high-Q GMR puts vigorous stress on the fabrication process. To increase the Q-factor of resonances in Device II, it is better to confine the mode to the core, i.e. increase n_{eff}. The narrower resonances at larger core thicknesses and smaller unit-cell periods in Figs. 4.7(c,d) supports this argument. Therefore, the principal strategy in controlling the Q-factor is the thickness of the core region, $t_{Ta_2O_5}$, and the unit-cell periodicity, P. Increasing n_{eff} increases the energy storage inside the core region and decreases the leakage to the graphene. The critical coupling condition is then satisfied by the very high-Q GMR, and the resultant bandwidth is low. This is the reason why $t_{Ta_2O_5}$ in Device II is much higher than that of Device I, and P in Device II is smaller than that in Device I. t_{PMMA} and w are tailored accordingly to meet critical coupling condition.

To examine the effect of the SiO_2 thickness in the absorption spectrum, we varied it over a wide range from 100 nm to 500 nm, and the result is shown in Fig. 4.8(a). The key observation is that the absorption spectrum shows maxima and minima that are periodic with $\lambda/2n_{SiO_2}$, λ being the resonance wavelength. This is consistent with the results reported in refs. [125, 167] and it is because of the phase-shift introduced by the SiO_2 layer and the FP modes defined by it[125]. Another reason may be that the system evolves from critical coupling to overcoupling or undercoupling, as altering glass thickness changes external leakage rate[122], while the intrinsic loss rate remains almost the same. An interesting observation is that glass thickness starts having an effect on resonance wavelength below a certain value. Besides this, when t_{SiO_2} is close to the value resulting in absorption maxima, an increase in it causes the bandwidth to increase. This is because the external leakage rate controls the bandwidth of absorption, described by Eq.4.9.

We inspected the polarization-independence of Device II, and the result is

shown in Fig. 4.8(b). In terms of the absorption strength, Device II shows slightly more polarization dependence than Device I. This is because, as the Q-factor of GMR is increased, meeting the critical coupling condition becomes stricter. Hence, the spectrum becomes more sensitive to the energy stored in the GMR. Slight variations in this energy can then disturb the critical coupling condition. Nevertheless, the absorption strength is still above 98% for all source angles, and the spectral position of resonance shows even less dependence on polarization. It is worthwhile to mention that the proposed structure cannot become polarization insensitive if the thin absorbing film is inherently anisotropic. An example for such a case would be phosphorene. In that case, the puckered configuration of phosphorene and the resulting anisotropy[170] means that although the grating has 60° rotational symmetry, overall structure will not have this feature.

The sensitivity of GMR to geometrical parameters gives Device II a great tunability in visible and NIR ranges. As a general guideline, the resonance can be red-shifted by an increase in $t_{Ta_2O_5}$ and P, as in Figs. 7(c,d). To decrease the bandwidth, on the other hand, it is necessary to increase $t_{Ta_2O_5}$ but decrease P, so that n_{eff} increases. t_{SiO_2} is picked accordingly to satisfy the critical coupling condition. Tuning of the GMR between 570 nm and 970 nm is shown in Fig. 4.8(c). Device V in Fig. 4.8(c) is also an example of achieving multiple resonances from a single device. Device VII has an FWHM of only 0.5 nm, reaching an ultra-high Q-factor of approx. 2000. This is because graphene's intrinsic absorption starts declining for wavelengths larger than 850 nm. The main drawback of our design in terms of tunability is that the intrinsic absorption of gold starts to be significant below $\sim$ 600nm. Therefore, although 100% absorption can be achieved below 550 nm easily, it is not graphene that is responsible for perfect absorption. Replacing the gold mirror with dielectric Bragg mirror can extend the perfect absorption in graphene in the visible range. Aluminum and silver can also be used as the back-mirror, as their absorption starts dominating at significantly smaller wavelengths, but the latter's degradation in air is an issue to consider in fabrication process[171].

We now accentuate the fundamental difference in the design methodologies of Device I and Device II. In Device I, the effective mode refractive index had

to be kept at an intermediate value because too high or too weak confinement of the mode to the core was detrimental to absorption. However, in Device II we could be able to confine the mode as much as we can to the core, without considering transmitted losses, and critical coupling gives both perfect absorption and ultra-narrow bandwidth. The same design strategy in Device I would result in absorption and transmission approaching each other, and to 50%.

Up to now, this section dealt with achieving perfect absorption with monolayer graphene. However, the concept of critical coupling is general and can be applied to other 2D materials, such as transition-metal dichalcogenides (TMDs), and multilayer graphene to yield perfect absorption with polarization insensitivity. To explain the effect of multilayer graphene, we increased the number of graphene layers in the simulations, and the result is demonstrated in Fig. 4.8(d). The result of the addition of graphene layers is the decrease in absorption strength and the broadening of the absorption peak, without a change of resonance wavelength. All of these results are well-expected from coupled mode theory and Eq.4.9. Increasing the number of graphene layers would not affect the external leakage rate of the resonator as it is controlled by the mode confinement to the core. However, the intrinsic absorption rate would increase and the match between the external leakage rate and intrinsic absorption rate would then be lost. So, increasing the graphene layers drives the resonator towards undercoupling[168]. Other 2D materials, such as transition-metal dichalcogenides show stronger light-matter interaction than graphene, in the order of 10% in the visible range[172]. Compared to the intrinsic 2.3% absorption in graphene, larger intrinsic absorption in TMDs would mean satisfying the critical coupling condition requires a larger external leakage rate for matching. So, the absorption spectrum associated with them would be inherently broader. From the viewpoint of light sensing or biosensing applications, using graphene is advantageous due to narrower bandwidth. However, the broader resonances associated with TMDs would mean a larger average absorption in the visible spectrum and the presence of a direct bandgap combined with it makes monolayer TMDs a great candidate for photodetection and photovoltaics [173, 174].

The experimental verification of this work starts with the fabrication flow of

choosing a Silicon or quartz substrate. Choice of substrate does not affect Device II as the thick gold layer means that there will be insignificant amount of light reaching there. Thus, a thin (5-10 nm) Titanium layer can be coated beneath gold for better adhesion, without affecting the optical properties. After that gold, SiO_2 and Ta_2O_5 can all be coated by Physical Vapor Deposition (PVD) methods such as sputtering. Chemical Vapor Deposition (CVD) grown graphene can be transferred and PMMA grating structure can be realized by electron-beam lithography. The numerical findings of this section propose that the core thickness and the unit-cell periodicity are the most important factors in determining the resonance position and bandwidth, as well as the absorption strength. This makes the precise deposition of Ta_2O_5 and electron-beam lithography of the 2D grating structure the most important steps. The fabricated samples can be characterized by Fourier Transform Infrared Spectroscopy (FTIR) technique for the resonances in NIR, whereas confocal microscopy can be utilized for resonances in visible range. We believe that the deviations of experimental findings from theoretical results can be restricted to a controlled region by the physical laws and explanations presented in this section.

Chapter 5

One-Way and Near-Absolute Polarization Insensitive Perfect Absorption by using an All-Dielectric Metasurface

This chapter is on part reprinted with permission from: **Deniz Umut Yildirim**, Amir Ghobadi, Mahmut Can Soydan, Andriy E. Serebryannikov, and Ekmel Ozbay, "One-way and near-absolute polarization insensitive near-perfect absorption by using an all-dielectric metasurface," Optics Letters, 2020, 45, 2010-2013, https://doi.org/10.1364/OL.387350.

5.1 Introduction

In this section, we use a 2-dimensional sub-wavelength grating-waveguide structure to excite its GMRs, and subsequently use it as a near-absolute polarization insensitive frequency-selective reflector (FSR), on top of which there is a spacer

dielectric and an absorbing indium tin oxide (ITO) layer. We employ finite-difference-time-domain (FDTD) method to numerically show that the coupling of incident light to the GMRs yields a resonance band, in which perfect absorption of near-infrared radiation is obtained under forward illumination (90%) with 19 nm of full-width at half-maximum (FWHM) at 1.82 μm. In the backwards direction, the reflection reached as high as (98.5%), resulting in ultra-high forward-to-backward reflection ratio of 60. In the adjacent frequency bands, the transmission reached as high as 65%. We also show the tunability of the bandwidth of the resonant regions, as we also designed a device with a resonance bandwidth of 300 nm.

5.2 Results and Discussion

Our proposed device in Fig. 5.1(a) is an FSR-insulator-oxide (MIO) cavity. The bottom FSR, which employs a unique 2-dimensional, sub-wavelength, periodically modulated, high permittivity Germanium (Ge) grating, is used to redirect the otherwise transmitted electromagnetic waves (EMWs) back into the cavity. The spacer dielectric, SiO_2, is used to create the necessary phase accumulation to redirect the EMWs mostly to the top absorbing layer of our cavity, which is a planar layer of ITO, a lossy plasmonic material. The entire structure is supported by a Quartz substrate. It is important to mention that throughout this section, SiO_2 perfectly covers the grating grooves and extends above it. Furthermore, forward (backward) excitation is defined as the case when EMWs are incident from the ITO (substrate) side, i.e. when EMWs propagate in the -z (+z) direction, defined in Fig. 5.1(a). Fig. 5.1(b) illustrates the the unit-cell of our 2D sub-wavelength grating FSR from the top-view. In this device, the position of the resonant spectral region and its Q-factor are highly related to the thickness of the grating region, t_{Ge}; the periodicity, P, of the unit cell in y-direction, the width of each grating stripe, w. The effect of all of these factors on GMRs and fabrication complexity are investigated in detail in our recent works [26, 28]. The cavity resonance condition due to the accumulated phase in a round-trip in the cavity, and the strength of absorption in both forward and backward cases are

determined by t_{SiO_2} and t_{ITO}, respectively.

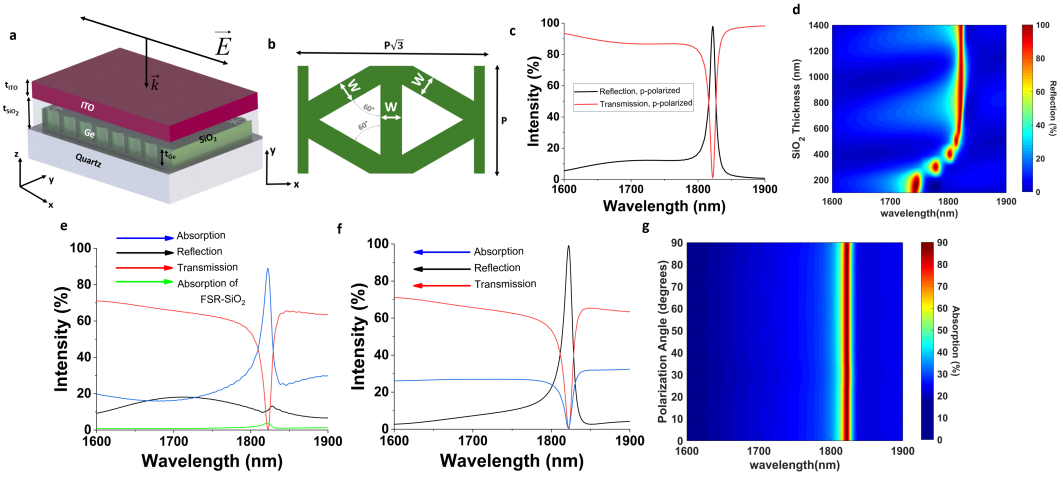

Figure 5.1: Achieving one-way absorption/reflection with adjacent transparency windows in a narrowband design. **(a)** The proposed device to achieve one-way absorption/reflection with transparency in sidebands functionality. SiO_2 layer is drawn transparently to make the FSR visible as well. **(b)** Unit-cell of FSR, elaborating the 2D grating, as seen from the top-view. **(c)** Transmission and Reflection spectra of the FSR-SiO_2 structure under p-polarized incident plane wave. **(d)**: Spectral response of the FSR-SiO_2 structure when thickness of the SiO_2 spacer, t_{SiO_2} is changed. Spectral response of the narrowband device under **(e)**: forward, **(f)**: backward illumination. **(g)** Reflection map of FSR-SiO_2 structure for the polarization angles spanning from 0° (p, TM-polarization) to 90° (s, TE-polarization)

We initiate our analysis by first scrutinizing the excitation of GMRs in the FSR, which defines the frequency band where there is the forward absorption/backward reflection functionality. To investigate the spectral response of Device I, we utilize FDTD simulations. In the simulations, we illuminated the unit-cell with a broadband plane-wave at normal incidence whose electric-field is polarized in the x-direction ($\phi = 0$, p-polarization), as in Fig. 5.1(a). In the x and y directions of the simulation region, we employed periodic boundary conditions, while in the z-direction perfectly matched layers (PML) are adopted. We use two monitors to find the reflected (R) and transmitted (T) power, normalized to the incident

power. The dispersion effect of Ge, SiO_2, and ITO are retrieved with ellipsometry measurements. While the former two are in good agreement with the models based on the Sellmeier equation [160], permittivity of ITO is modeled by using the Drude-Lorentz model [28].

We first fixed t_{Ge} at 220 nm, P at 1100 nm, w at 240 nm, t_{SiO_2} at 1200 nm, but not yet incorporated ITO. We then looked at R and T of the FSR-SiO_2 structure in the forward excitation case, to gain insight about the resonance excitation. The simulation result in Fig. 5.1(c) shows a sharp guided-mode resonance, manifesting itself as a peak in reflection (98%) and a dip in transmission at 1.82 μm. The physics governing the excitation the GMRs, as well as the effect of FSR parameter on the GMR excitation wavelength and its bandwidth are particularized in our recent works [26, 28]. Briefly, GMRs are excited when a diffracted order of the grating can excite a guided-mode of the waveguide core, which is the FSR itself, as a result of phase-matching[86], governed by Eq. 5.1.

$$\begin{aligned} k_{x,g} &= mK_x = n\frac{2\pi}{\Lambda_x} = n\frac{2\pi}{P\sqrt{3}} \\ k_{y,g} &= mK_y = l\frac{2\pi}{\Lambda_y} = l\frac{2\pi}{P} \\ \beta &= |k_{x,g}\hat{\mathbf{x}} + k_{y,g}\hat{\mathbf{y}}| \end{aligned} \tag{5.1}$$

where β is the propagation wavenumber along the guiding direction, Λ_x (K_x) and Λ_y (K_y) are the grating periods (reciprocal lattice vectors) along x and y-directions, respectively. m (l) is the diffraction orders along the x (y)-direction, and $k_{x,g}$ ($k_{y,g}$) is the wavevector component of the guided-mode along the x (y)-direction. As the guided-mode propagates, it also continually leaks energy to the far-field because of the periodicity of the waveguide core. The sharp increase in the reflection is because the re-radiated waves interfere destructively with the directly transmitted waves, but constructively with the reflected waves.

It is critical to mention that as long as t_{SiO_2} goes beyond the evanescent decay length of the guided-mode in the SiO_2, it has little effect on the resonance wavelength, which is the case in our design. We verified this by keeping t_{Ge}, P, and w at their aforementioned values, and sweeping t_{SiO_2} from 100 nm to 1400

nm, in which the lower bound only partially covers the grooves of the grating. The reflection spectrum shown in Fig. 5.1(d) demonstrates that t_{SiO_2} has a profound effect on the resonance when it is smaller than t_{Ge}, because it controls the effective refractive index of FSR. For t_{SiO_2} values between t_{Ge} =220 nm and 400 nm, the effective waveguide core refractive index is set but the non-negligible optical fields in the SiO_2-Air boundary that necessitate new boundary conditions and hence modify β. For t_{SiO_2} larger than 400 nm, the resonance wavelength is indeed independent of t_{SiO_2}.

Next, to obtain the desired functionality, we add the planar ITO layer of t_{ITO} =90 nm on top SiO_2 spacer to attain near-perfect EMW absorption for forward-propagating radiation. From this point on, $\rightarrow$ and $\leftarrow$ symbols will be used for absorption (A), R, and T in forward and backward illumination cases, respectively. From R and T, we calculated the spectral absorption by using $A = 1 - R - T$. The spectral response of our proposed narrowband device, under forward and backward illumination cases, is shown in Figs. 5.1(e,f), respectively. These two figures confirm the multifunctionality of our device, as in the resonant range there is absorption (reflection) under forward (backward) illumination, while neighboring transparency windows with almost 65% transmittance are also obtained. With the values of $\overrightarrow{A}$ =0.9, and $\overleftarrow{A}$ =0.015 ($\overleftarrow{R}$ =0.985); the forward-to-backward absorption contrast, $\psi = \overrightarrow{A}/\overleftarrow{A}$ reached as high as 60, while the linewidth (FWHM) is measured as 19 nm. The independence of the transmission from the illumination direction, in other words, having $\overrightarrow{T} = \overleftarrow{T}$ mainly stems from the Lorentz reciprocity [175] and energy conservation, while the mismatch in $\overrightarrow{A}$ and $\overleftarrow{A}$ originates from the fact that in the forward excitation case, the reflected EMWs are directed back to the ITO layer and harnessed mostly there, whereas in the backward case, they do not reach to ITO and leave the device from the substrate. We also explored the contribution of FSR-SiO_2 to the near-perfect absorption in the forward excitation case, by placing three three-dimensional (3D) monitors on the FSR-SiO_2 layer. We used the formula in Eq. 5.2,

$$\frac{dP_{loss}}{dV} = \frac{1}{2} w \epsilon''(w) |E|^2 \tag{5.2}$$

where P_{loss} is the absorbed power due to conduction losses and dielectric hysteresis, V is the volume, w is the angular frequency, $\epsilon''(w)$ is the imaginary part of the complex permittivity and $|E|^2$ is the modulus of the complex electric-field inside each layer [93]. dP_{loss}/dV is integrated over FSR-SiO_2 and normalized to the incident power to obtain absorption of it, which is plotted in Fig. 5.1(e). It is seen that during the resonance, the FSR-SiO_2 has an absorption of 0.04, due to the small but non-negligible losses in Ge. ITO is then the main absorbing layer in our design.

We investigated the insensitivity to polarization in more detail by sweeping the polarization angle of the source from 0° to 90°. The result that is shown in Fig. 5.1(g) clearly indicates that our proposed device maintains almost constant absorption at a nearly fixed spectral position. This mainly originates from the fact that the hexagonal grating structure that we adopted has almost identical interaction with the incoming E-field for all polarization angles [26, 28].

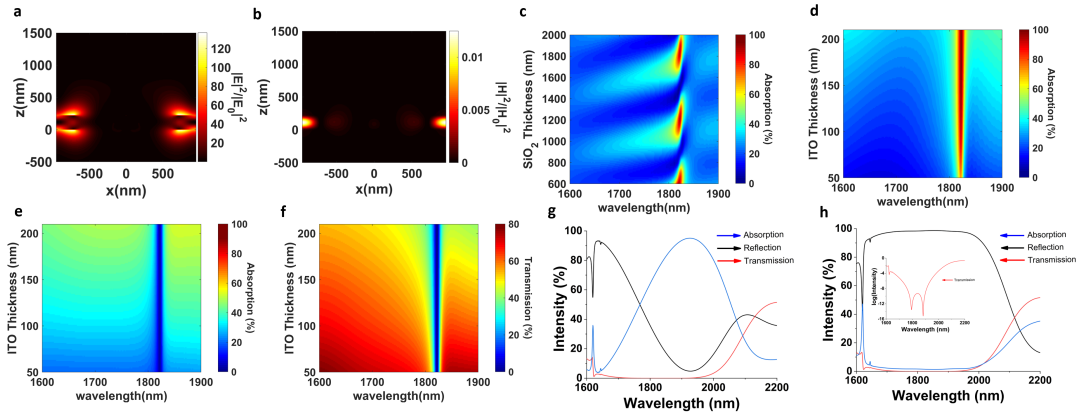

Figure 5.2: **(a)**: $|E|^2/|E_0|^2$ at XZ plane during resonance at 1.82μm. **(b)**: $|H|^2$ at XZ plane during resonance. $|E|^2$ and $|H|^2$ are the modulus of electric and magnetic field inside Device I, $|E_0|^2$ and $|H_0|^2$ denote that of incident light. GWS extends from z=0 to z=220 nm. Forward illumination absorption spectrum of the narrowband design under varying **(c)**: SiO_2 spacer thickness, t_{SiON_2} ,**(d)**: ITO thickness, t_{ITO}. Effect of t_{ITO} on the **(e)**: Absorption and **(f)**: Transmission spectra of the narrowband design under backwards illumination. Spectral response of the broadband device under **(g)**: forward, **(h)**: backward illumination.

To further discern the resonance phenomenon, we also plotted the electric and magnetic-field (E-field and H-field) profiles at the peak resonance wavelength, in Figs. 2(a,b), respectively. These figures clearly indicate a strong enhancement and the localization of both fields inside the FSR region. These figures also imply that the fundamental mode of the slab waveguide is excited. This is an anticipated result because of the relatively small thickness of the waveguide core region with respect to the wavelength, t_{Ge}/λ, as the excitation of higher order modes of a waveguide requires larger core thickness.

In Fig. 5.2(c), we demonstrate how t_{SiO_2} affects $\overrightarrow{A}$, while all other geometrical parameters are fixed. $t_{SiO_2} = 1200$ nm is picked because it is the smallest thickness that, firstly, yields the highest absorption, due to creating the necessary phase accumulation to redirect the EMWs mostly to the top absorbing layer. Secondly, it is much larger than the evanescent decay length of the guided-mode, as shown in Fig. 5.1(g), so it has no influence on the GMRs. Following this, we swept t_{ITO} and the result is shown in Fig. 5.2(d). Fig. 5.2(d). indicates that the thicker layers of ITO boosts $\overrightarrow{A}$. This is because EMWs travel more in ITO and are harvested before leaving the device. The choice of 90 nm is made by considering the backward illumination, the absorption and transmission spectra in this case are plotted with respect to t_{ITO} in Fig. 5.2(e,f), respectively. While t_{ITO} has little effect on $\overleftarrow{A}$ in the resonant band, as can be observed from Fig. 5.2(e), it decreases $\overleftarrow{T}$ considerably, as in Fig. 5.2(f). Therefore, t_{ITO} is picked as 90 nm to have near-perfect $\overrightarrow{A}$ of 0.9 in the resonant band, while not accentuating the losses in the adjacent bands.

We also designed a device that operates in a wide spectral band [176], by altering the geometrical parameters to $t_{Ge} = 420$ nm, $P = 1100$ nm, $w = 180$ nm, $t_{SiO_2} = 800$ nm, and $t_{ITO} = 110$ nm. The simulation results for this device, under forward and backward illumination are presented in Figs. 5.2(g,h), respectively. While $\overleftarrow{R}$ remained above 0.9 for a broad spectral range of 400 nm, $\overrightarrow{R}$ did not show a flat perfect absorption, although the peak absorption reached 0.95 and the linewidth is measured to be 300 nm. To have a broad GMR bandwidth, the main design parameter that we changed was the thickness of the grating (FSR), t_{Ge}. By doing so, the waveguide is able to support higher order modes [93] in addition

to the fundamental mode, and the overlap of these resulted in a broad spectrum. The coexistence of two modes is observed upon plotting the natural logarithm of transmission, as in the inset of Fig. 5.2(h). In this device, since there are two modes which are spectrally close and overlap with each other, the field profiles that correspond to distinct modes are superposed and, therefore, could not be plotted.

Chapter 6

Conclusion

This thesis demonstrated and discussed four important functionalities of dielectric metasurfaces, namely, passive radiative coolers, colorimetric refractive index sensors, monolayer graphene based color filters, and resonant one-way perfect absorber/reflectors with supported transparency in the neighboring spectral bands.

In Chapter 2, which is devoted to our first work, metasurfaces utilizing disordered, densely packed, and titled ITO nanorod forests as the top absorbing layer are experimentally analyzed and the attainment of a record-high thermal-emissivity of 0.968, and Figure of Merit of 5.73 are verified. The top ITO scaffold of our metasurfaces enabled the very efficient harvesting of thermal-radiation to have an ultra-broadband absorption in the thermal-infrared range, while their small thickness did not accentuate the dielectric losses in the solar spectrum. The utilization of oblique-angle deposition with the line-of-sight coating of PVD systems allowed not only the realization of such ITO nanoforests but also large-scale and high-throughput fabrication. The experimental results of the proposed devices are compared to designs to the numerical simulations of periodic ITO discs and the experimental result of planar ITO thin-film, as the top absorbing layer. These comparisons further proved the absorption enhancement by the ITO nanoforests, which is mainly due to relieving the strong phonon reflection bands of SiO_2 in thermal-infrared. Overall, our ultra-high performance, yet large-scale

compatible devices hold great promise for the radiative cooling of spacecraft during their space missions, and it is also highly applicable to many areas such as terrestrial radiative coolers and thermal imaging for labeled security purposes.

In our second work, which constitutes Chapter 3 of this thesis, we analyzed and experimentally confirmed the highly sensitive measurement of adsorbed layers and change of the surrounding medium's refractive index numerically. Colorimetric detection and near-absolute insensitivity of proposed design to the polarization incident light are verified. Our novel 2D sub-wavelength periodically modulated grating structure also acts as a waveguide to support the guided-modes. The interaction of absorbed layers with the guided-mode within the evanescent decay length of the mode results in the shift of the resonance wavelength. Numerically calculated linewidth of the resonance, 0.58 nm and the maximum sensitivity of 110 nm/RIU resulted in a very-high Figure-of-Merit of 190. A design that is more tolerant to fabrication inaccuracies is fabricated and the maximum sensitivity reached as high as 235.2 nm/RIU, while the linewidth is measured as 19 nm. Perfect agreement of resonance positions and their shift is obtained between experimental results and numerical simulations. The performance of our nanosensor can be improved even further and/or adapted to different scenarios by the physical laws and explanations outlined in this work, at the cost of a more cumbersome fabrication route. Overall, our simple yet robust, and easy-to-fabricate device holds great promise in many areas such as biomedicine with less invasive and point-of-care therapies, drug detection, and contamination control.

In Chapter 4, which is allocated to our third project, the enhancement of light-graphene interaction is numerically analyzed and the near-perfect polarization insensitivity of proposed design to incident light is verified. Our novel sub-wavelength dielectric grating excites the guided modes of an asymmetric dielectric slab waveguide. The critical coupling of the guided mode resonances to graphene resulted in perfect light absorption that is tunable by structural parameters in the visible and NIR ranges. The bandwidth of the resonance, 0.8 nm resulted in a very high Q-factor of 850. To the best of our knowledge, this bandwidth is smaller than all of the relevant device proposals with sub-micron thickness. Overall, our simple yet robust, and easy-to-fabricate device holds great

promise in ultra-sensitive color detection and design of advanced photodetectors.

In our fourth and final work, which is presented in Chapter 5, we analyzed and numerically confirmed one-way absorption/reflection with transmission in the sidebands functionality of an all-dielectric metasurface. Near-absolute insensitivity of the proposed design to the polarization incident light is verified. Our 2D sub-wavelength periodically modulated grating-waveguide structure supports guided-mode resonances. Within the bandwidth of the resonance, it effectively acts as a mirror to create a Fabry-Pérot type cavity, due to the SiO_2 spacer dielectric and the top layer ITO. In the narrowband design, the linewidth is calculated to be 19 nm, while the forward-to-backward absorption ratio is found to be 60. These results are complemented with 65% transparency in the sideband frequencies. A broadband design is also analyzed, and in the forward direction, resonant absorption with a peak strength of 95% and 300 nm linewidth is realized, while in the backward direction, reflection stayed above 0.9 for 400 nm. Overall, our simple yet robust, and easy-to-fabricate device is promising not only for the applications in the near-infrared range but also for THz applications, such as obtaining single-frequency signals from THz sources, in which the multifunctionality shown in this work is required.

Bibliography

[1] A. J. Hoffman, L. Alekseyev, S. S. Howard, K. J. Franz, D. Wasserman, V. A. Podolskiy, E. E. Narimanov, D. L. Sivco, and C. Gmachl, "Negative refraction in semiconductor metamaterials," 2007.

[2] D. R. Smith, J. B. Pendry, and M. C. Wiltshire, "Metamaterials and negative refractive index," 2004.

[3] G. T. Papadakis, D. Fleischman, A. Davoyan, P. Yeh, and H. A. Atwater, "Optical magnetism in planar metamaterial heterostructures," Nature Communications, 2018.

[4] C. Menzel, C. Helgert, C. Rockstuhl, E. B. Kley, A. Tünnermann, T. Pertsch, and F. Lederer, "Asymmetric transmission of linearly polarized light at optical metamaterials," Physical Review Letters, 2010.

[5] J. Valentine, J. Li, T. Zentgraf, G. Bartal, and X. Zhang, "An optical cloak made of dielectrics," Nature Materials, 2009.

[6] D. Schurig, J. J. Mock, B. J. Justice, S. A. Cummer, J. B. Pendry, A. F. Starr, and D. R. Smith, "Metamaterial electromagnetic cloak at microwave frequencies," Science, 2006.

[7] A. Fang, T. Koschny, and C. M. Soukoulis, "Lasing in metamaterial nanostructures," Journal of Optics A: Pure and Applied Optics, 2010.

[8] E. Plum, V. A. Fedotov, P. Kuo, D. P. Tsai, and N. I. Zheludev, "Towards the lasing spaser: controlling metamaterial optical response with semiconductor quantum dots," Optics Express, 2009.

[9] N. I. Zheludev and Y. S. Kivshar, "From metamaterials to metadevices," 2012.

[10] N. Yu and F. Capasso, "Flat optics with designer metasurfaces," 2014.

[11] D. Neshev and I. Aharonovich, "Optical metasurfaces: new generation building blocks for multi-functional optics," Light: Science and Applications, 2018.

[12] N. Yu, P. Genevet, M. A. Kats, F. Aieta, J. P. Tetienne, F. Capasso, and Z. Gaburro, "Light propagation with phase discontinuities: Generalized laws of reflection and refraction," Science, 2011.

[13] A. I. Kuznetsov, A. E. Miroshnichenko, M. L. Brongersma, Y. S. Kivshar, and B. Luk'yanchuk, "Optically resonant dielectric nanostructures," 2016.

[14] M. Khorasaninejad, W. T. Chen, R. C. Devlin, J. Oh, A. Y. Zhu, and F. Capasso, "Metalenses at visible wavelengths: Diffraction-limited focusing and subwavelength resolution imaging," Science, 2016.

[15] S. Wang, P. C. Wu, V. C. Su, Y. C. Lai, M. K. Chen, H. Y. Kuo, B. H. Chen, Y. H. Chen, T. T. Huang, J. H. Wang, R. M. Lin, C. H. Kuan, T. Li, Z. Wang, S. Zhu, and D. P. Tsai, "A broadband achromatic metalens in the visible," Nature Nanotechnology, 2018.

[16] H.-H. Hsiao, C. H. Chu, and D. P. Tsai, "Fundamentals and Applications of Metasurfaces," Small Methods, 2017.

[17] M. C. Soydan, A. Ghobadi, D. U. Yildirim, V. B. Erturk, and E. Ozbay, "All Ceramic-Based Metal-Free Ultra-broadband Perfect Absorber," Plasmonics, 2019.

[18] M. C. Soydan, A. Ghobadi, D. U. Yildirim, E. Duman, A. Bek, V. B. Erturk, and E. Ozbay, "Lithography-Free Random Bismuth Nanostructures for Full Solar Spectrum Harvesting and Mid-Infrared Sensing," Advanced Optical Materials, vol. 8, no. 4, p. 1901203, 2020.

[19] T. Ellenbogen, K. Seo, and K. B. Crozier, "Chromatic plasmonic polarizers for active visible color filtering and polarimetry," Nano Letters, 2012.

[20] C. Ji, K. T. Lee, T. Xu, J. Zhou, H. J. Park, and L. J. Guo, "Engineering Light at the Nanoscale: Structural Color Filters and Broadband Perfect Absorbers," 2017.

[21] N. I. Landy, C. M. Bingham, T. Tyler, N. Jokerst, D. R. Smith, and W. J. Padilla, "Design, theory, and measurement of a polarization-insensitive absorber for terahertz imaging," Physical Review B - Condensed Matter and Materials Physics, 2009.

[22] P. Offermans, M. C. Schaafsma, S. R. Rodriguez, Y. Zhang, M. Crego-Calama, S. H. Brongersma, and J. Gómez Rivas, "Universal scaling of the figure of merit of plasmonic sensors," ACS Nano, 2011.

[23] M. E. Stewart, C. R. Anderton, L. B. Thompson, J. Maria, S. K. Gray, J. A. Rogers, and R. G. Nuzzo, "Nanostructured plasmonic sensors," 2008.

[24] A. Tittl, A. K. U. Michel, M. Schäferling, X. Yin, B. Gholipour, L. Cui, M. Wuttig, T. Taubner, F. Neubrech, and H. Giessen, "A Switchable Mid-Infrared Plasmonic Perfect Absorber with Multispectral Thermal Imaging Capability," Advanced Materials, 2015.

[25] T. Xu, Y.-K. Wu, X. Luo, and L. J. Guo, "Plasmonic nanoresonators for high-resolution colour filtering and spectral imaging," Nature Communications, 2010.

[26] D. U. Yildirim, A. Ghobadi, and E. Ozbay, "Near-absolute polarization insensitivity in grapheme based ultra-narrowband perfect visible light absorber," Scientific Reports, vol. 8, no. 1, pp. 1–14, 2018.

[27] S. Yokogawa, S. P. Burgos, and H. A. Atwater, "Plasmonic color filters for CMOS image sensor applications," Nano Letters, 2012.

[28] D. U. Yildirim, A. Ghobadi, M. C. Soydan, M. Gokbayrak, A. Toprak, B. Butun, and E. Ozbay, "Colorimetric and Near-Absolute Polarization Insensitive Refractive-Index Sensing in All-Dielectric Guided-Mode Resonance based Metasurface," The Journal of Physical Chemistry C, p. acs.jpcc.9b04748, 2019.

[29] J. K. Tong, W. C. Hsu, Y. Huang, S. V. Boriskina, and G. Chen, "Thin-film 'thermal well' emitters and absorbers for high-efficiency thermophotovoltaics," Scientific Reports, 2015.

[30] W. Li and J. Valentine, "Metamaterial perfect absorber based hot electron photodetection," Nano Letters, 2014.

[31] Y. Zhai, Y. Ma, S. N. David, D. Zhao, R. Lou, G. Tan, R. Yang, and X. Yin, "Scalable-manufactured randomized glass-polymer hybrid metamaterial for daytime radiative cooling," Science, 2017.

[32] D. Wu, C. Liu, Z. Xu, Y. Liu, Z. Yu, L. Yu, L. Chen, R. Li, R. Ma, and H. Ye, "The design of ultra-broadband selective near-perfect absorber based on photonic structures to achieve near-ideal daytime radiative cooling," Materials and Design, 2018.

[33] D. U. Yildirim, A. Ghobadi, M. C. Soydan, O. Atesal, A. Toprak, M. D. Caliskan, and E. Ozbay, "Disordered and Densely Packed ITO Nanorods as an Excellent Lithography-Free Optical Solar Reflector Metasurface," ACS Photonics, 2019.

[34] M. C. Soydan, A. Ghobadi, D. U. Yildirim, V. B. Erturk, and E. Ozbay, "Deep subwavelength light confinement in disordered bismuth nanorods as a linearly thermal-tunable metamaterial," physica status solidi (RRL) – Rapid Research Letters, vol. 14, no. 7, p. 2000066, 2020.

[35] V. L. Pisacane and . Moore Robert C. (Robert Clark), Fundamentals of space systems. New York : Oxford University Press, 1994.

[36] M. Ovchinnikov, S. Mckenna-lawlor, S. Psychology, N. Kanas, D. Manuy, W. J. Larson, and J. R. Wertz, Space Mission Analysis and Design. Microcosm, 1991.

[37] K. Sun, C. A. Riedel, Y. Wang, A. Urbani, M. Simeoni, S. Mengali, M. Zalkovskij, B. Bilenberg, C. H. De Groot, and O. L. Muskens, "Metasurface

Optical Solar Reflectors Using AZO Transparent Conducting Oxides for Radiative Cooling of Spacecraft," ACS Photonics, vol. 5, no. 2, pp. 495–501, 2018.

[38] K. Sun, C. A. Riedel, A. Urbani, M. Simeoni, S. Mengali, M. Zalkovskij, B. Bilenberg, C. H. De Groot, and O. L. Muskens, "VO2 Thermochromic Metamaterial-Based Smart Optical Solar Reflector," ACS Photonics, vol. 5, no. 6, pp. 2280–2286, 2018.

[39] K. Aydin, V. E. Ferry, R. M. Briggs, and H. A. Atwater, "Broadband polarization-independent resonant light absorption using ultrathin plasmonic super absorbers," Nature Communications, 2011.

[40] Q. Liang, W. Yu, W. Zhao, T. Wang, J. Zhao, H. Zhang, and S. Tao, "Numerical study of the meta-nanopyramid array as efficient solar energy absorber," Optical Materials Express, 2013.

[41] F. Ding, J. Dai, Y. Chen, J. Zhu, Y. Jin, and S. I. Bozhevolnyi, "Broadband near-infrared metamaterial absorbers utilizing highly lossy metals," Scientific Reports, 2016.

[42] M. G. Nielsen, A. Pors, O. Albrektsen, and S. I. Bozhevolnyi, "Efficient absorption of visible radiation by gap plasmon resonators," Optics Express, 2012.

[43] Q. Liang, T. Wang, Z. Lu, Q. Sun, Y. Fu, and W. Yu, "Metamaterial-Based Two Dimensional Plasmonic Subwavelength Structures Offer the Broadest Waveband Light Harvesting," Advanced Optical Materials, 2013.

[44] Y. Cui, J. Xu, K. Hung Fung, Y. Jin, A. Kumar, S. He, and N. X. Fang, "A thin film broadband absorber based on multi-sized nanoantennas," Applied Physics Letters, 2011.

[45] Q. Feng, M. Pu, C. Hu, and X. Luo, "Engineering the dispersion of metamaterial surface for broadband infrared absorption," Optics Letters, 2012.

[46] W. Guo, Y. Liu, and T. Han, "Ultra-broadband infrared metasurface absorber," Optics Express, 2016.

[47] H. Wang and L. Wang, "Perfect selective metamaterial solar absorbers," Optics Express, 2013.

[48] J. A. Bossard, L. Lin, S. Yun, L. Liu, D. H. Werner, and T. S. Mayer, "Near-ideal optical metamaterial absorbers with super-octave bandwidth," ACS Nano, 2014.

[49] A. Ghobadi, H. Hajian, M. Gokbayrak, S. Abedini Dereshgi, A. Toprak, B. Butun, and E. Ozbay, "Visible light nearly perfect absorber : an optimum unit cell arrangement for near absolute polarization insensitivity," Optics Express, 2017.

[50] F. Ding, Y. Jin, B. Li, H. Cheng, L. Mo, and S. He, "Ultrabroadband strong light absorption based on thin multilayered metamaterials," Laser and Photonics Reviews, 2014.

[51] Y. Cui, K. H. Fung, J. Xu, H. Ma, Y. Jin, S. He, and N. X. Fang, "Ultrabroadband light absorption by a sawtooth anisotropic metamaterial slab," Nano Letters, 2012.

[52] J. Zhu, Z. Ma, W. Sun, F. Ding, Q. He, L. Zhou, and Y. Ma, "Ultrabroadband terahertz metamaterial absorber," Applied Physics Letters, 2014.

[53] A. Ghobadi, H. Hajian, B. Butun, and E. Ozbay, "Strong Light-Matter Interaction in Lithography-Free Planar Metamaterial Perfect Absorbers," ACS Photonics, vol. 5, pp. 4203–4221, 2018.

[54] S. Abedini Dereshgi, A. Ghobadi, H. Hajian, B. Butun, and E. Ozbay, "Ultra-Broadband, Lithography-Free, and Large-Scale Compatible Perfect Absorbers: The Optimum Choice of Metal layers in Metal-Insulator Multilayer Stacks," Scientific Reports, 2017.

[55] A. Ghobadi, S. A. Dereshgi, H. Hajian, G. Birant, B. Butun, A. Bek, and E. Ozbay, "97 percent light absorption in an ultrabroadband frequency range utilizing an ultrathin metal layer: Randomly oriented, densely packed dielectric nanowires as an excellent light trapping scaffold," Nanoscale, vol. 9, no. 43, pp. 16652–16660, 2017.

[56] A. Ghobadi, H. Hajian, A. R. Rashed, B. Butun, and E. Ozbay, "Tuning the metal filling fraction in absorbers to maximize the absorption bandwidth," Photonics Reseach, 2018.

[57] S. Q. Li, P. Guo, L. Zhang, W. Zhou, T. W. Odom, T. Seideman, J. B. Ketterson, and R. P. H. Chang, "Infrared plasmonics with indium-tin-oxide nanorod arrays," ACS Nano, 2011.

[58] J. Kim, A. Dutta, G. V. Naik, A. J. Giles, F. J. Bezares, C. T. Ellis, J. G. Tischler, A. M. Mahmoud, H. Caglayan, O. J. Glembocki, A. V. Kildishev, J. D. Caldwell, A. Boltasseva, and N. Engheta, "Role of epsilon-near-zero substrates in the optical response of plasmonic antennas," Optica, 2016.

[59] M. Abb, Y. Wang, N. Papasimakis, C. H. De Groot, and O. L. Muskens, "Surface-enhanced infrared spectroscopy using metal oxide plasmonic antenna arrays," Nano Letters, vol. 14, no. 1, pp. 346–352, 2014.

[60] S. Sang, Y. Wang, Q. Feng, Y. Wei, J. Ji, and W. Zhang, "Progress of new label-free techniques for biosensors: A review," Critical Reviews in Biotechnology, vol. 36, no. 3, pp. 465–481, 2016.

[61] J. Elf, G. W. Li, and X. S. Xie, "Probing transcription factor dynamics at the single-molecule level in a living cell," Science, vol. 316, no. 5828, pp. 1191–1194, 2007.

[62] B. Schuler, E. A. Lipman, and W. A. Eaton, "Probing the free-energy surface for protein folding with single-molecule fluorescence spectroscopy.," Nature, vol. 419, no. 6908, pp. 743–7, 2002.

[63] M. J. Lang, P. M. Fordyce, A. M. Fordyce, K. C. Neuman, and S. M. Block, "Simultaneous, coincident optical trapping and single-molecule fluorescence," Nature Methods, vol. 1, no. 2, pp. 133–139, 2004.

[64] B. Huang, H. Wu, D. Bhaya, A. Grossman, S. Granier, B. K. Kobilka, and R. N. Zare, "Counting low-copy number proteins in a single cell," Science, vol. 315, no. 5808, pp. 81–84, 2007.

[65] A. M. Armani, R. P. Kulkarni, S. E. Fraser, R. C. Flagan, and K. J. Vahala, "Label-free, single-molecule detection with optical microcavities," Science, vol. 317, no. 5839, pp. 783–787, 2007.

[66] N. L. Rosi and C. A. Mirkin, "Nanostructures in Biodiagnostics," Chemical Reviews, vol. 105, no. 4, pp. 1547–1562, 2005.

[67] N. Bontempi, K. E. Chong, H. W. Orton, I. Staude, D. Y. Choi, I. Alessandri, Y. S. Kivshar, and D. N. Neshev, "Highly sensitive biosensors based on all-dielectric nanoresonators," Nanoscale, vol. 9, no. 15, pp. 4972–4980, 2017.

[68] P. D. Howes, S. Rana, and M. M. Stevens, "Plasmonic nanomaterials for biodiagnostics," Chemical Society Reviews, vol. 43, no. 11, pp. 3835–3853, 2014.

[69] K. Saha, S. S. Agasti, C. Kim, X. Li, and V. M. Rotello, "Gold Nanoparticles in Chemical and Biological Sensing," Chemical Reviews, vol. 112, no. 5, pp. 2739–2779, 2012.

[70] O. Yavas, M. Svedendahl, P. Dobosz, V. Sanz, and R. Quidant, "On-a-chip Biosensing Based on All-Dielectric Nanoresonators," Nano Letters, vol. 17, no. 7, pp. 4421–4426, 2017.

[71] J. Zhang, L. Wang, D. Pan, S. Song, F. Y. Boey, H. Zhang, and C. Fan, "Visual cocaine detection with gold nanoparticles and rationally engineered aptamer structures," Small, vol. 4, no. 8, pp. 1196–1200, 2008.

[72] L. Shi, C. Jing, W. Ma, D. W. Li, J. E. Halls, F. Marken, and Y. T. Long, "Plasmon resonance scattering spectroscopy at the single-nanoparticle level: Real-time monitoring of a click reaction," Angewandte Chemie - International Edition, vol. 52, no. 23, pp. 6011–6014, 2013.

[73] F. Long, A. Zhu, and H. Shi, "Recent advances in optical biosensors for environmental monitoring and early warning," Sensors (Switzerland), vol. 13, no. 10, pp. 13928–13948, 2013.

[74] H. Aldewachi, T. Chalati, M. N. Woodroofe, N. Bricklebank, B. Sharrack, and P. Gardiner, "Gold nanoparticle-based colorimetric biosensors," Nanoscale, vol. 10, no. 1, pp. 18–33, 2018.

[75] W. Q. Lim and Z. Gao, "Plasmonic nanoparticles in biomedicine," Nano Today, vol. 11, no. 2, pp. 168–188, 2016.

[76] G. K. Joshi, S. Deitz-Mcelyea, M. Johnson, S. Mali, M. Korc, and R. Sardar, "Highly specific plasmonic biosensors for ultrasensitive MicroRNA detection in plasma from pancreatic cancer patients," Nano Letters, vol. 14, no. 12, pp. 6955–6963, 2014.

[77] M. Mahmoudi, S. E. Lohse, C. J. Murphy, A. Fathizadeh, A. Montazeri, and K. S. Suslick, "Variation of protein corona composition of gold nanoparticles following plasmonic heating," Nano Letters, vol. 14, no. 1, pp. 6–12, 2014.

[78] S. A. Maier, Plasmonics: Fundamentals and applications. Springer Science, Business Media, 2007.

[79] A. I. Kuznetsov, A. E. Miroshnichenko, M. L. Brongersma, Y. S. Kivshar, and B. Luk'yanchuk, "Optically resonant dielectric nanostructures," Science, vol. 354, no. 6314, 2016.

[80] I. Staude, A. E. Miroshnichenko, M. Decker, N. T. Fofang, S. Liu, E. Gonzales, J. Dominguez, T. S. Luk, D. N. Neshev, I. Brener, and Y. Kivshar, "Tailoring directional scattering through magnetic and electric resonances in subwavelength silicon nanodisks," ACS Nano, vol. 7, no. 9, pp. 7824–7832, 2013.

[81] M. Parry, A. Komar, B. Hopkins, S. Campione, S. Liu, A. E. Miroshnichenko, J. Nogan, M. B. Sinclair, I. Brener, and D. N. Neshev, "Active tuning of high-Q dielectric metasurfaces," Applied Physics Letters, vol. 111, no. 5, 2017.

[82] J. Sautter, I. Staude, M. Decker, E. Rusak, D. N. Neshev, I. Brener, and Y. S. Kivshar, "Active tuning of all-dielectric metasurfaces.," ACS nano, vol. 9, no. 4, pp. 4308–15, 2015.

[83] M. Decker and I. Staude, "Resonant dielectric nanostructures: A low-loss platform for functional nanophotonics," Journal of Optics (United Kingdom), vol. 18, no. 10, 2016.

[84] Y. Yang, I. I. Kravchenko, D. P. Briggs, and J. Valentine, "All-dielectric metasurface analogue of electromagnetically induced transparency," Nature Communications, vol. 5, 2014.

[85] D. G. Baranov, D. A. Zuev, S. I. Lepeshov, O. V. Kotov, A. E. Krasnok, A. B. Evlyukhin, and B. N. Chichkov, "All-dielectric nanophotonics: the quest for better materials and fabrication techniques," Optica, vol. 4, no. 7, pp. 814–825, 2017.

[86] D. Rosenblatt, A. Sharon, and A. A. Friesem, "Resonant grating waveguide structures," IEEE Journal of Quantum Electronics, vol. 33, no. 11, pp. 2038–2059, 1997.

[87] R. Magnusson and S. S. Wang, "New principle for optical filters," Applied Physics Letters, vol. 61, no. 9, pp. 1022–1024, 1992.

[88] R. Halir, P. J. Bock, P. Cheben, A. Ortega-Moñux, C. Alonso-Ramos, J. H. Schmid, J. Lapointe, D. X. Xu, J. G. Wangüemert-Pérez, Í. Molina-Fernández, and S. Janz, "Waveguide sub-wavelength structures: A review of principles and applications," Laser and Photonics Reviews, vol. 9, no. 1, pp. 25–49, 2015.

[89] R. Magnusson, B. R. Wenner, J. W. Allen, M. S. Allen, S. Gimlin, K. J. Lee, D. W. Weidanz, H. Hemmati, and Y. H. Ko, "The guided-mode resonance biosensor: principles, technology, and implementation," Frontiers in Biological Detection: From Nanosensors to Systems X, no. February 2018, p. 15, 2018.

[90] X. Wei and S. M. Weiss, "Guided mode biosensor based on grating coupled porous silicon waveguide," Optics Express, vol. 19, no. 12, p. 11330, 2011.

[91] A. J. Haes, S. Zou, G. C. Schatz, and R. P. Van Duyne, "Nanoscale optical biosensor: Short range distance dependence of the localized surface plasmon

resonance of noble metal nanoparticles," Journal of Physical Chemistry B, vol. 108, no. 22, pp. 6961–6968, 2004.

[92] C. E. Rubio-Mercedes, V. F. Rodriguez-Esquerre, I. T. Lima, and H. E. Hernandez-Figueroa, "Analysis of straight periodic segmented waveguide using the 2-D finite element method," Journal of Lightwave Technology, vol. 32, no. 11, pp. 2163–2169, 2014.

[93] A. Yariv and P. Yeh, Photonics: Optical Electronics in Modern Communications (The Oxfo New York, NY, USA: Oxford University Press, Inc., 2006.

[94] K. S. Novoselov, A. K. Geim, S. V. Morozov, D. Jiang, Y. Zhang, S. V. Dubonos, I. V. Grigorieva, and A. A. Firsov, "Electric field effect in atomically thin carbon films.," Science (New York, N.Y.), 2004.

[95] F. Bonaccorso, Z. Sun, T. Hasan, and A. C. Ferrari, "Graphene photonics and optoelectronics," Nature Photonics, 2010.

[96] K. S. Novoselov, A. K. Geim, S. V. Morozov, D. Jiang, M. I. Katsnelson, I. V. Grigorieva, S. V. Dubonos, and A. A. Firsov, "Two-dimensional gas of massless Dirac fermions in graphene," Nature, 2005.

[97] A. K. Geim and K. S. Novoselov, "The rise of graphene," Nature Materials, 2007.

[98] J. He, Y. Chai, and L. Liao, "Focus on 2D materials beyond graphene," 2018.

[99] S. Manzeli, D. Ovchinnikov, D. Pasquier, O. V. Yazyev, and A. Kis, "2D transition metal dichalcogenides," 2017.

[100] M. Bernardi, M. Palummo, and J. C. Grossman, "Extraordinary sunlight absorption and one nanometer thick photovoltaics using two-dimensional monolayer materials," Nano Letters, 2013.

[101] W. D. Tan, C. Y. Su, R. J. Knize, G. Q. Xie, L. J. Li, and D. Y. Tang, "Mode locking of ceramic Nd:yttrium aluminum garnet with graphene as a saturable absorber," Applied Physics Letters, 2010.

[102] Q. Bao, H. Zhang, Y. Wang, Z. Ni, Y. Yan, Z. X. Shen, K. P. Loh, and D. Y. Tang, "Atomic layer graphene as saturable absorber for ultrafast pulsed lasers," Advanced Functional Materials, 2009.

[103] T. Mueller, F. Xia, and P. Avouris, "Graphene photodetectors for high-speed optical communications," Nature Photonics, 2010.

[104] C. H. Liu, Y. C. Chang, T. B. Norris, and Z. Zhong, "Graphene photodetectors with ultra-broadband and high responsivity at room temperature," Nature Nanotechnology, 2014.

[105] X. Wang, L. Zhi, and K. Müllen, "Transparent, conductive graphene electrodes for dye-sensitized solar cells," Nano Letters, 2008.

[106] S. Bae, H. Kim, Y. Lee, X. Xu, J. S. Park, Y. Zheng, J. Balakrishnan, T. Lei, H. Ri Kim, Y. I. Song, Y. J. Kim, K. S. Kim, B. Özyilmaz, J. H. Ahn, B. H. Hong, and S. Iijima, "Roll-to-roll production of 30-inch graphene films for transparent electrodes," Nature Nanotechnology, 2010.

[107] M. Liu, X. Yin, E. Ulin-Avila, B. Geng, T. Zentgraf, L. Ju, F. Wang, and X. Zhang, "A graphene-based broadband optical modulator," Nature, 2011.

[108] Z. Li and N. Yu, "Modulation of mid-infrared light using graphene-metal plasmonic antennas," Applied Physics Letters, 2013.

[109] S. Y. Hong, J. I. Dadap, N. Petrone, P. C. Yeh, J. Hone, and R. M. Osgood, "Optical third-harmonic generation in graphene," Physical Review X, 2013.

[110] M. A. Vincenti, D. De Ceglia, M. Grande, A. D'Orazio, and M. Scalora, "Third-harmonic generation in one-dimensional photonic crystal with graphene-based defect," Physical Review B - Condensed Matter and Materials Physics, vol. 89, no. 16, pp. 1–6, 2014.

[111] W. Gao, J. Shu, C. Qiu, and Q. Xu, "Excitation of plasmonic waves in graphene by guided-mode resonances," ACS Nano, vol. 6, no. 9, pp. 7806–7813, 2012.

[112] T. R. Zhan, F. Y. Zhao, X. H. Hu, X. H. Liu, and J. Zi, "Band structure of plasmons and optical absorption enhancement in graphene on subwavelength dielectric gratings at infrared frequencies," Physical Review B - Condensed Matter and Materials Physics, 2012.

[113] J. Christensen, A. Manjavacas, S. Thongrattanasiri, F. H. L. Koppens, and F. J. García De Abajo, "Graphene plasmon waveguiding and hybridization in individual and paired nanoribbons," ACS Nano, 2012.

[114] B. Zhao and Z. M. Zhang, "Strong Plasmonic Coupling between Graphene Ribbon Array and Metal Gratings," ACS Photonics, 2015.

[115] K. S. Novoselov, V. I. Fal'Ko, L. Colombo, P. R. Gellert, M. G. Schwab, and K. Kim, "A roadmap for graphene," 2012.

[116] K. Kim, J. Y. Choi, T. Kim, S. H. Cho, and H. J. Chung, "A role for graphene in silicon-based semiconductor devices," 2011.

[117] M. Furchi, A. Urich, A. Pospischil, G. Lilley, K. Unterrainer, H. Detz, P. Klang, A. M. Andrews, W. Schrenk, G. Strasser, and T. Mueller, "Microcavity-integrated graphene photodetector," Nano Letters, 2012.

[118] A. Ferreira, N. M. Peres, R. M. Ribeiro, and T. Stauber, "Graphene-based photodetector with two cavities," Physical Review B - Condensed Matter and Materials Physics, 2012.

[119] Z. Fang, Z. Liu, Y. Wang, P. M. Ajayan, P. Nordlander, and N. J. Halas, "Graphene-antenna sandwich photodetector," Nano Letters, 2012.

[120] X. Zhu, L. Shi, M. S. Schmidt, A. Boisen, O. Hansen, J. Zi, S. Xiao, and N. A. Mortensen, "Enhanced light-matter interactions in graphene-covered gold nanovoid arrays," Nano Letters, 2013.

[121] S. Jahani and Z. Jacob, "All-dielectric metamaterials," 2016.

[122] J. R. Piper and S. Fan, "Total Absorption in a Graphene Monolayer in the Optical Regime by Critical Coupling with a Photonic Crystal Guided Resonance," ACS Photonics, vol. 1, no. 4, pp. 347–353, 2014.

[123] Y. Long, Y. Li, L. Shen, W. Liang, H. Deng, and H. Xu, "Dually guided-mode-resonant graphene perfect absorbers with narrow bandwidth for sensors," Journal of Physics D: Applied Physics, vol. 49, no. 32, pp. 4–9, 2016.

[124] Y. Long, L. Shen, H. Xu, H. Deng, and Y. Li, "Achieving ultranarrow graphene perfect absorbers by exciting guided-mode resonance of one-dimensional photonic crystals," Scientific Reports, vol. 6, no. August, pp. 2–9, 2016.

[125] M. Grande, M. A. Vincenti, T. Stomeo, G. V. Bianco, D. de Ceglia, N. Aközbek, V. Petruzzelli, G. Bruno, M. De Vittorio, M. Scalora, and A. D'Orazio, "Graphene-based perfect optical absorbers harnessing guided mode resonances," Optics Express, vol. 23, no. 16, p. 21032, 2015.

[126] M. Grande, M. A. Vincenti, T. Stomeo, G. V. Bianco, D. de Ceglia, N. Aközbek, V. Petruzzelli, G. Bruno, M. De Vittorio, M. Scalora, and A. D'Orazio, "Graphene-based absorber exploiting guided mode resonances in one-dimensional gratings," Optics Express, vol. 22, no. 25, p. 31511, 2014.

[127] C. C. Guo, Z. H. Zhu, X. D. Yuan, W. M. Ye, K. Liu, J. F. Zhang, W. Xu, and S. Q. Qin, "Experimental Demonstration of Total Absorption over 99% in the Near Infrared for Monolayer-Graphene-Based Subwavelength Structures," Advanced Optical Materials, 2016.

[128] M. Kumar, J. Tervo, T. Kaplas, and Y. Svirko, "Graphene-enhanced waveguide-resonance gratings," Journal of Nanophotonics, 2016.

[129] T. Jang, H. Youn, Y. J. Shin, and L. J. Guo, "Transparent and Flexible Polarization-Independent Microwave Broadband Absorber," ACS Photonics, vol. 1, pp. 279–284, mar 2014.

[130] M. Mutlu, S. Cakmakyapan, A. E. Serebryannikov, and E. Ozbay, "One-way reciprocal spoof surface plasmons and relevant reversible diodelike beaming," Phys. Rev. B, vol. 87, p. 205123, may 2013.

[131] P. Rodríguez-Ulibarri, M. Beruete, and A. E. Serebryannikov, "One-way quasiplanar terahertz absorbers using nonstructured polar dielectric layers," Physical Review B, vol. 96, no. 15, pp. 1–9, 2017.

[132] J. D. Plummer, M. D. Deal, and P. B. Griffin, "Silicon VLSI technology: fundamentals, practice and modeling," 2000.

[133] A. Barranco, A. Borras, A. R. Gonzalez-Elipe, and A. Palmero, "Perspectives on oblique angle deposition of thin films: From fundamentals to devices," 2016.

[134] Z. Wang, P. R. West, X. Meng, N. Kinsey, V. M. Shalaev, and A. Boltasseva, "Angled physical vapor deposition techniques for non-conformal thin films and three-dimensional structures," MRS Communications, vol. 6, no. 1, pp. 17–22, 2016.

[135] C. Grüner, S. Liedtke, J. Bauer, S. G. Mayr, and B. Rauschenbach, "Morphology of Thin Films Formed by Oblique Physical Vapor Deposition," ACS Applied Nano Materials, vol. 1, no. 3, pp. 1370–1376, 2018.

[136] A. G. Mark, J. G. Gibbs, T. C. Lee, and P. Fischer, "Hybrid nanocolloids with programmed three-dimensional shape and material composition," Nature Materials, 2013.

[137] M. Jensen and M. J. Brett, "Square spiral 3D photonic bandgap crystals at telecommunications frequencies.," Optics express, 2005.

[138] J. Q. Xi, M. F. Schubert, J. K. Kim, E. F. Schubert, M. Chen, S. Y. Lin, W. Liu, and J. A. Smart, "Optical thin-film materials with low refractive index for broadband elimination of Fresnel reflection," Nature Photonics, 2007.

[139] X. Xiao, G. Dong, J. Shao, H. He, and Z. Fan, "Optical and electrical properties of SnO2:Sb thin films deposited by oblique angle deposition," Applied Surface Science, 2010.

[140] B. A. Munk, Frequency Selective Surfaces: Theory and Design. New York: John Wiley, 2000.

[141] D. M. Pozar, Microwave Engineering, 4th Edition. Wiley, 2011.

[142] S. Fan and J. D. Joannopoulos, "Analysis of guided resonances in photonic crystal slabs," Physical Review B, 2002.

[143] G. V. Naik, V. M. Shalaev, and A. Boltasseva, "Alternative plasmonic materials: Beyond gold and silver," 2013.

[144] D. Ji, A. Cheney, N. Zhang, H. Song, J. Gao, X. Zeng, H. Hu, S. Jiang, Z. Yu, and Q. Gan, "Efficient Mid-Infrared Light Confinement within Sub-5-nm Gaps for Extreme Field Enhancement," Advanced Optical Materials, vol. 5, no. 17, 2017.

[145] R. Li, D. Wu, Y. Liu, L. Yu, Z. Yu, and H. Ye, "Infrared Plasmonic Refractive Index Sensor with Ultra-High Figure of Merit Based on the Optimized All-Metal Grating," Nanoscale Research Letters, vol. 12, no. 1, 2017.

[146] S. Luo, J. Zhao, D. Zuo, and X. Wang, "Perfect narrow band absorber for sensing applications," Optics Express, vol. 24, no. 9, p. 9288, 2016.

[147] Z. Yong, S. Zhang, C. Gong, and S. He, "Narrow band perfect absorber for maximum localized magnetic and electric field enhancement and sensing applications," Scientific Reports, vol. 6, 2016.

[148] D. Wu, R. Li, Y. Liu, Z. Yu, L. Yu, L. Chen, C. Liu, R. Ma, and H. Ye, "Ultra-narrow Band Perfect Absorber and Its Application as Plasmonic Sensor in the Visible Region," Nanoscale Research Letters, vol. 12, 2017.

[149] A. Ghobadi, H. Hajian, M. Gokbayrak, S. A. Dereshgi, A. Toprak, B. Butun, and E. Ozbay, "Visible light nearly perfect absorber: an optimum unit cell arrangement for near absolute polarization insensitivity," Optics Express, vol. 25, no. 22, p. 27624, 2017.

[150] Marcuse Dietrich, A. Telephone, and T. Company., Theory of dielectric optical waveguides. Academic Press Boston, 2nd ed. ed., 1991.

[151] S. Fan and J. D. Joannopoulos, "Analysis of guided resonances in photonic crystal slabs," Physical Review B, vol. 65, no. 23, 2002.

[152] N. Liu, M. Mesch, T. Weiss, M. Hentschel, and H. Giessen, "Infrared perfect absorber and its application as plasmonic sensor," Nano Letters, vol. 10, no. 7, pp. 2342–2348, 2010.

[153] Y. Tang, Z. Zhang, R. Wang, Z. Hai, C. Xue, W. Zhang, and S. Yan, "Refractive index sensor based on fano resonances in metal-insulator-metal waveguides coupled with resonators," Sensors (Switzerland), vol. 17, no. 4, 2017.

[154] D. Wu, Y. Liu, R. Li, L. Chen, R. Ma, C. Liu, and H. Ye, "Infrared Perfect Ultra-narrow Band Absorber as Plasmonic Sensor," Nanoscale Research Letters, vol. 11, no. 1, 2016.

[155] H. Lu, X. Liu, D. Mao, and G. Wang, "Plasmonic nanosensor based on Fano resonance in waveguide-coupled resonators," Optics Letters, vol. 37, no. 18, p. 3780, 2012.

[156] N. Bontempi, M. Salmistraro, M. Ferroni, L. E. Depero, and I. Alessandri, "Probing the spatial extension of light trapping-induced enhanced Raman scattering in high-density Si nanowire arrays," Nanotechnology, vol. 25, no. 46, 2014.

[157] S. Peng and G. M. Morris, "Experimental demonstration of resonant anomalies in diffraction from two-dimensional gratings," Optics Letters, vol. 21, no. 8, p. 549, 1996.

[158] J. D. Plummer, Silicon VLSI technology: fundamentals, practice and modeling. Pearson Education India, 2009.

[159] S. S. Wang and R. Magnusson, "Theory and applications of guided-mode resonance filters.," Applied optics, vol. 32, no. 14, pp. 2606–13, 1993.

[160] E. D. Palik, Handbook of optical constants of solids. Academic Press, 2012.

[161] F. Lumerical, "Solutions," 2016.

[162] Y. Ding and R. Magnusson, "Resonant leaky-mode spectral-band engineering and device applications," Optics Express, vol. 12, no. 23, p. 5661, 2004.

[163] J. D. Jackson, Classical electrodynamics. New York, {NY}: Wiley, 3rd ed. ed., 1999.

[164] G. W. Hanson, "Dyadic Green's functions and guided surface waves for a surface conductivity model of graphene," Journal of Applied Physics, 2008.

[165] M. Lončar, A. Scherer, and Y. Qiu, "Photonic crystal laser sources for chemical detection," Applied Physics Letters, vol. 82, no. 26, pp. 4648–4650, 2003.

[166] S. M. Rytov, "Electromagnetic properties of a finely stratified medium," Soviet Physics JETP, 1956.

[167] S. Thongrattanasiri, F. H. L. Koppens, and F. J. García De Abajo, "Complete optical absorption in periodically patterned graphene," Physical Review Letters, vol. 108, no. 4, pp. 1–5, 2012.

[168] H. A. Haus, Waves and fields in optoelectronics. Englewood Cliffs, NJ: Prentice-Hall, 1984.

[169] A. Yariv, "Critical coupling and its control in optical waveguide-ring resonator systems," IEEE Photonics Technology Letters, 2002.

[170] S. C. Dhanabalan, J. S. Ponraj, Z. Guo, S. Li, Q. Bao, and H. Zhang, "Emerging Trends in Phosphorene Fabrication towards Next Generation Devices," 2017.

[171] G. V. Naik, V. M. Shalaev, and A. Boltasseva, "Alternative plasmonic materials: Beyond gold and silver," 2013.

[172] Y. Li, A. Chernikov, X. Zhang, A. Rigosi, H. M. Hill, A. M. Van Der Zande, D. A. Chenet, E. M. Shih, J. Hone, and T. F. Heinz, "Measurement of the optical dielectric function of monolayer transition-metal dichalcogenides: MoS2, Mo S e2, WS2, and WS e2," Physical Review B - Condensed Matter and Materials Physics, vol. 90, no. 20, pp. 1–6, 2014.

[173] J. S. Ponraj, Z. Q. Xu, S. C. Dhanabalan, H. Mu, Y. Wang, J. Yuan, P. Li, S. Thakur, M. Ashrafi, K. McCoubrey, Y. Zhang, S. Li, H. Zhang, and Q. Bao, "Photonics and optoelectronics of two-dimensional materials beyond graphene," Nanotechnology, 2016.

[174] S. C. Dhanabalan, J. S. Ponraj, H. Zhang, and Q. Bao, "Present perspectives of broadband photodetectors based on nanobelts, nanoribbons, nanosheets and the emerging 2D materials," 2016.

[175] R. J. Potton, "Reciprocity in optics," Reports on Progress in Physics, vol. 67, no. 5, pp. 717–754, 2004.

[176] W. Wu and R. Magnusson, "Total absorption of TM polarized light in a 100 nm spectral band in a nanopatterned thin a-Si film," Optics Letters, 2012.

Appendix A

Scientific Contributions

A.1 Journal Articles

1. **D. U. Yildirim**, A. Ghobadi, and E. Ozbay, "Near-absolute polarization insensitivity in grapheme based ultra-narrowband perfect visible light absorber," Scientific Reports, vol. 8, no. 1, pp. 1–14, 2018.

2. **D. U. Yildirim**, A. Ghobadi, M. C. Soydan, M. Gokbayrak, A. Toprak, B. Butun, and E. Ozbay, "Colorimetric and Near-Absolute Polarization Insensitive Refractive-Index Sensing in All-Dielectric Guided-Mode Resonance based Metasurface," The Journal of Physical Chemistry C, p. acs.jpcc.9b04748, 2019.

3. **D. U. Yildirim**, A. Ghobadi, M. C. Soydan, O. Atesal, A. Toprak, M. D. Caliskan, and E. Ozbay, "Disordered and Densely Packed ITO Nanorods as an Excellent Lithography-Free Optical Solar Reflector Metasurface," ACS Photonics, 2019.

4. **D. U. Yildiri**m, A. Ghobadi, M. C. Soydan, A. E. Serebryannikov, and E. Ozbay, "One-way and near-absolute polarization insensitive near-perfect absorption by using an all-dielectric metasurface," Optics Letters, vol. 45, no. 7, pp. 2010–2013, 2020

5. M. C. Soydan, A. Ghobadi, **D. U. Yildirim**, V. B. Erturk, and E. Ozbay, "All Ceramic-Based Metal-Free Ultra-broadband Perfect Absorber," Plasmonics, 2019.

6. M. C. Soydan, A. Ghobadi, **D. U. Yildirim**, E. Duman, A. Bek, V. B. Erturk, and E. Ozbay, "Lithography-Free Random Bismuth Nanostructures for Full Solar Spectrum Harvesting and Mid-Infrared Sensing," Advanced Optical Materials, vol. 8, no. 4, p. 1901203, 2020.

7. M. C. Soydan, A. Ghobadi, **D. U. Yildirim**, V. B. Erturk, and E. Ozbay, "Deep subwavelength light confinement in disordered bismuth nanorods as a linearly thermal-tunable metamaterial," physica status solidi (RRL) - Rapid Research Letters, vol. 14, no. 7, p. 2000066, 2020

8. C. Cakir, H. Kocer, Y. Durna, **D.U. Yildirim**, A. Ghobadi, H. Hajian, K. Aydin, H. Kurt, N. Saglam, E. Ozbay, "Unveiling the Optical Parameters of Vanadium Dioxide in the Phase Transition Region: A Hybrid Modeling Approach," *received a minor revision from RSC Advances*, 2020

9. V. Ercaglar, V. Erturk, A. Ghabadi, **D.U. Yildirim**, E. Ozbay, "Thermally-tunable Spectrally-Selective Absorber Enabled by an All-dielectric Metamirror," *in submission to Optics Letters*, 2020

10. Z. Eftekhari, A. Ghobadi, M.C. Soydan, **D.U. Yildirim**, N. Cinel E. Ozbay, "Strong quantum emission from defective hexagonal boron nitride monolayer coupled to near-touching random plasmonic nanounits," *in submission to Optics Letters*, 2020

A.2 Refereed Conference Papers

1. **D. U. Yildirim**, A. Ghobadi, M. C. Soydan, O. Atesal, A. Toprak, M. D. Caliskan, and E. Ozbay, "Disordered and densely packed ITO nanorods as an excellent lithography-free optical solar re ector metasurface for the radiative cooling of spacecraft," in Metamaterials, Metadevices, and Metasystems 2019 (N. Engheta, M. A. Noginov, and N. I. Zheludev, eds.), vol.

11080, pp. 63-72, International Society for Optics and Photonics, SPIE, 2019.